Project/Contract no.: 018698

Project acronym: OVCAD

Project title: Ovarian Cancer – Diagnosis of a Silent Killer

Instrument: Specific Targeted Research or Innovation Project

Thematic Priority: Life sciences, genomics and biotechnology for health

Title of report: Publishable Report

Period covered: from 01.01.2006 to 30.06.2010 Date of preparation: 01.08.2010

Start date of project: 01.01.2006 Duration: 54 months

Project coordinator name: Robert Zeillinger

Project coordinator organisation name: Medical University of Vienna, Vienna, Austria

Revision: 1

Contents

Publishable Report

1. Publishable final activity report

2. Project execution and results

2.1. Project objectives

In Europe 63000 ovarian cancer cases are diagnosed and 41000 ovarian cancer patients die annually. 75% of patients are diagnosed at advanced stages due to an asymptomatic course. 75% of these patients die within 5 years. Treatment involves surgery followed by chemotherapy. However, 25% of patients relapse within 6 months after initial treatment. There is doubt whether these patients benefit from this therapy at all. Recurrent disease is diagnosed by clinical evidences or by CA125 dynamics. But detection is limited due to lack of sensitivity and specificity, as is the case with primary diagnosis. Currently, there is no method to detect minimal disease, the first indicator of therapy failure and precursor of recurrence, which inevitably leaves specific traces through out the body. There is strong need for molecular-oriented research to detect minimal disease in order to disburden patients from an inefficient and toxic therapy.

The aim of this project is to define clinically useful molecular-orientated early detection of minimal disease in ovarian cancer that can identify patients not responding to the standard therapy at the time of surgery. This will eventually lead to alternative therapy modalities, which can really bring benefits to this group of patients. "Signatures" that signal the presence of minimal disease will be systematically investigated at various molecular levels (DNA, RNA and protein) and in a broad spectrum of biological materials (tumour tissue, disseminated tumour cells, sera, white blood cells, ascites) from ovarian cancer patients. Profiling of chromosomal loss or gain, gene methylation and mutations, mRNA expression and protein will be analyzed. Specific signatures that predict patients' outcome or indicate minimal disease, eventually suitable for early primary diagnosis, will be extracted.

2.2. Contractors involved

Part. no.	Participant name	Participant short name	Country	Leader
1	Medizinische Universität Wien	MUW	Austria	Robert Zeillinger
2	Charité - Universitätsmedizin Berlin	Charité, Berlin	Germany	Jalid Sehouli
3	Katholieke Universiteit Leuven	K.U.Leuven	Belgium	Ignace Vergote
4	Institut Paoli-Calmettes	IPC	France	Jean-Paul Borg
5	German Cancer Research Center	DKFZ	Germany	Peter Altvogt
6	Kaplan Medical Center	Kaplan	Israel	Mina Fogel
7	Biofocus GmbH	Biofocus	Germany	Lothar Prix
8	Centre Régional de Lutte contre le Cancer de	CRLC de Montpellier	France	Charles Theillet

	Montpellier			
10	Centre for Biomedical Technology, Danube University Krems	ZBMT	Austria	Viktoria Weber
12	Emergentec biodevelopment GmbH	Emtec	Austria	Bernd Mayer
13	Labordiagnostika GmbH	ViennaLab	Austria	Fritz Kury
14	Erasmus Medisch Centrum Rotterdam	EMC	Netherlands	Els Berns
15	Vitateq Biotechnology GmbH	Vitateq	Austria	Hans Dieplinger
16*	Universitätsklinikum Hamburg-Eppendorf	UKE	Germany	Burkhard Brandt

* Sven Mahner is co-responsible for this contractor, taking the responsibility in WP2

2.3. Work performed and end results

General and specific objectives of the OVCAD project were defined in the "Description of Work":

General objectives:

- To establish and to validate molecular diagnostic methods to identify MRD in ovarian cancer patients.
- To define a new "diagnostic state-of-the-art" by correlating the diagnostic results with the clinically-defined response of the patients to standard therapy
- To discover and to characterize MRD by molecular diagnostics leading to additional therapeutic interventions, ultimately improving patients' prognosis and quality of life
- To better understand the mechanisms that cause MRD and therapy failure
- To identify and evaluate new potential therapy targets

Specific scientific objectives

- To define protein profiles in serum and tumours tissues which signal the presence of MRD, or predict recurrent MRD at the time of primary surgery
- To define specific mRNA expression signature of primary ovarian carcinomas and validate the known markers that indicate the likelihood of recurrence
- To define specific mRNA expression signatures of peripheral blood mononuclear cells that signal the presence of MDR and predict recurrent disease at the time of primary surgery
- To validate the selected signatures on a real-time PCR platform.
- To detect and characterize disseminated tumour cells in peripheral blood in respect of the DNA and RNA aberrations
- To define specific sites of DNA abnormalities in genomic profiling of ovarian tumour tissues by comparative genomic hybridization (CGH) that signal the presence of MDR and predict the response of patients to standard chemotherapy.
- To discover the ovarian cancer specific genes which are epigenetically inactivated by promoter hypermethylation, to validate these markers in primary ovarian carcinomas and free DNA in serum, and to define methylation signatures indicating MRD

- To investigate prognostic value of proteins like L1 or vitamin E-binding protein as alternatives to the standard serum tumour marker CA125 and their potential as targets for antibody-based therapy
- To identify accessible and antigenic sites on ovarian cancer specific proteins and B-cell candidates in silico, to validate the results experimentally and to quantify auto-antibodies that indicate the MDR
- To analyze K-*ras* mutations in primary ovarian carcinomas and in free DNA in serum as a model system for gene mutation-based detection of MRD
- To develop specific biocompatible adsorbents and devices for extra-corporeal antibody-based isolation of disseminated tumour cells from peripheral blood
- To investigate therapy modalities using novel targets and established NOD/Scid animal models.
- To characterize multi-drug resistance mechanisms with respect to the response of ovarian cancer patients to standard chemotherapy

Works were performed during the project period according to these defined objectives and the end results were obtained and presented below.

(1) Establishment of the OVCAD tumourbank

Establishment of the OVCAD tumourbank

To ensure all the planed works, biological materials from the ovarian cancer patients must be collected and processed with standard procedures. Workpackage 2 in OVCAD consortium includes 4 university clinics (P1, P2, P3 and P16) and is responsible for the task. One associated partner, Department of Obstetrics and Gynaecology, Medical University of Innsbruck, Austria was also involved into the project without receiving additional funding.

At the beginning of the project, WP2 has defined the inclusion criteria (Appendix 1), the sample coding system (Appendix 2) and established the standard protocols for processing all clinical materials including tumor tissues, blood and ascites (Appendix 3). An online database was established with the help of a subcontracted partner, Alcedis (www.ovcad.com).

From 1.1.2006 till 31.12.2008 clinical materials from 602 patients were handled. Because we had to precede the blood samples immediately after the blood was drawn and this happened quite often before the pathological and clinical confirmations could be obtained, about half of the patients were excluded mainly because of having benign diseases, borderline ovarian cancer, second malignant tumours, or ovarian cancer with FIGO I stage. After the final updating and data revising including more steps of plausibility test at the end of the project, 275 patients, who had FIGO stage II-IV epithelial ovarian cancer and received the standard treatment including debulking surgery and platinum-based chemotherapy were included in the OVCAD project (Table 1). Ages of the patients are between 18 and 85 years old with an average age of 58 year old. The average follow-up time is 26 months ranging from 1-49 months and with a median time of 25 months. 25% of patients had no response to the standard treatment, i.e. they had recurrent or progressive disease within 6 months after the last chemotherapy. 164 patients had developed recurrent disease during the whole follow-up time and 80 died of ovarian cancer. The clinical and pathological characteristics of the patients and tumours are shown in table 2.

Table 1. Recruitment rates of the patients

	Berlin	Hamburg	Innsbruck	Leuven	Vienna	Total
Number of patients	97	46	11	79	42	275
%	35	17	4	29	15	100

Table 2. Characteristics of the patients and tumours

	Number of patients	%
Histological type		
clear cell tumour	2	1
endometrioid tumour	13	5
Mmixed epithelial tumour	11	4
Mucinous tumour	3	1
Serous tumour	237	86
Undifferentiated tumour	9	3
Histological grade		
G1	10	4
G2	64	23
G3	200	73
unknown	1	0
FIGO stage		
II	15	6
III	212	77
IV	48	17
Lymphnode involvement		
pN0	65	24
pN1	143	52
unknown	67	24
pM		
pM0	142	52
pM1	49	18
pMX	84	31
Rest tumour		
no residual tumour	188	68
≤ 0.5cm	25	9
0.5 - 1cm	23	8
1 - 2cm	8	3
≥ 2cm	30	11
unknown	1	0
Peritoneal carcinomatosis		
yes	186	68
no	88	32
unknown	1	0
Ascites		

0	66	25
0 - 500ml	110	40
≥ 500ml	99	36
Total	275	100

The frequently applied surgical interventions were omentectomy, bilateral salpingo-oophorectomy, hysterectomy, pelvic and para-aortic lymphadenectomy, large bowel and small bowel resection. All patients received platinum-based chemotherapy. Some patients were treated with neo-adjuvant chemotherapy and some received adjuvant chemotherapy in form of intraperitoneal treatment.

From these 275 patients, tumor tissues, blood and ascites were collected. Tumor tissues were processed to isolate DNA, RNA, and lysate for protein measurement. In addition, paraffin blocks and sections were prepared for the partners, who needed to perform immunohistochemistry. Blood samples were processed by each WP2 partners to separate plasma, epithelial cell containing fraction and peripheral blood cell fraction. From ascites, cell pellet and supernatant were collected. Altogether, tumor tissues were available from 249 patients, ascites samples from 202 patients, and blood samples from 248 patients. In addition we also collected blood samples from 133 patients 6 months after the completion of chemotherapy. All these biological materials were delivered to OVCAD partners according to the DOW.

Thus we have established one of the well documented and biggest tumorbank of ovarian cancer in Europe and in the world, which is very valuable to investigate ovarian cancer.

Establishment of OVCAD data repository

In the DOW, we defined a task to perform integrated analyses of OVCAD data. In the first step, a database for the deposit of all OVCAD data must be established. The final aim of such a repository will be “Systems Biology” and “Systems Medicine” initiatives of ovarian cancer. Consequently, this add-on opportunity was conceptually and technologically included in OVCAD efforts. P12 led by Bernd Meyer together with P1 led by Robert Zeillinger took the lead in these efforts.

The fundament for the joint analysis procedures is a consolidated data handling environment covering i) structured data storage, ii) consolidated name spaces for molecular features, providing iii) flexible mapping of experimental procedures. P12 has developed such an environment and provided the platform for evaluating and testing OVCAD integration efforts.

Establishing the framework for use in OVCAD involved a management step for evaluating general requirements for bringing the platform into the consortium including the development of showcases, and a RTD step for delineating integrated data analysis options of value for the OVCAD data.

As the experimental procedures have been (naturally) heterogeneous the following core mapping of procedures was derived:

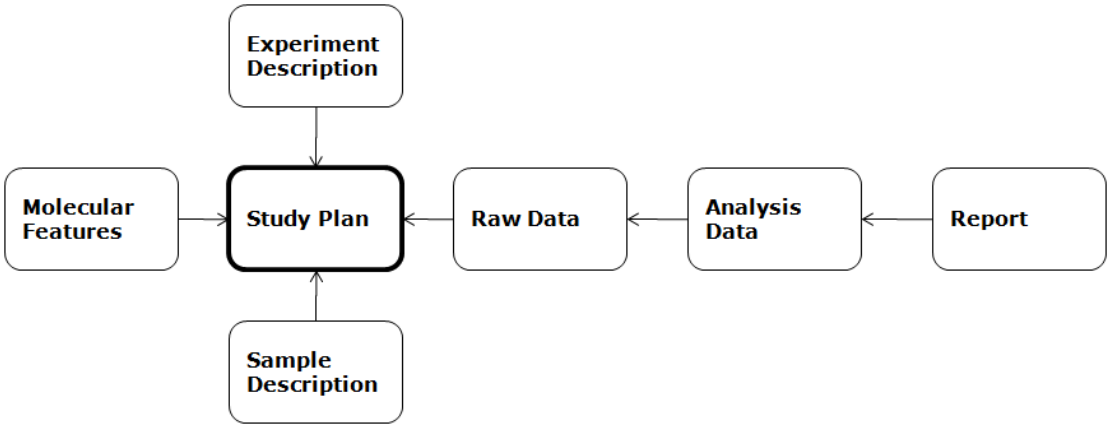

Figure 1. Structure of the repository.

Central element is a 'Study Plan', outlining responsibility, experimental setup, hypothesis, goals, etc. With this document the general structure of the study becomes clear. Subsequently, information is added to the Study Plan, covering i) what molecular features are studied utilizing b) what samples were used. Experiment description provides details on the protocol, followed by sets of raw data, analysis data and reports. By evaluating the OVCAD studies done so far (and potential future studies to be performed) we concluded to use this scheme as general structure.

In the data repository established each element is denoted as 'record' resembling any level of granularity. In translating selected OVCAD studies into the relations scheme we used detailed resolution for molecular features (Ensemble) and samples (sample codes used in the relational sample database) and course grained resolution for study-associated description files.

The repository was customized according to the OVCAD project structure, and structured data collection has started.

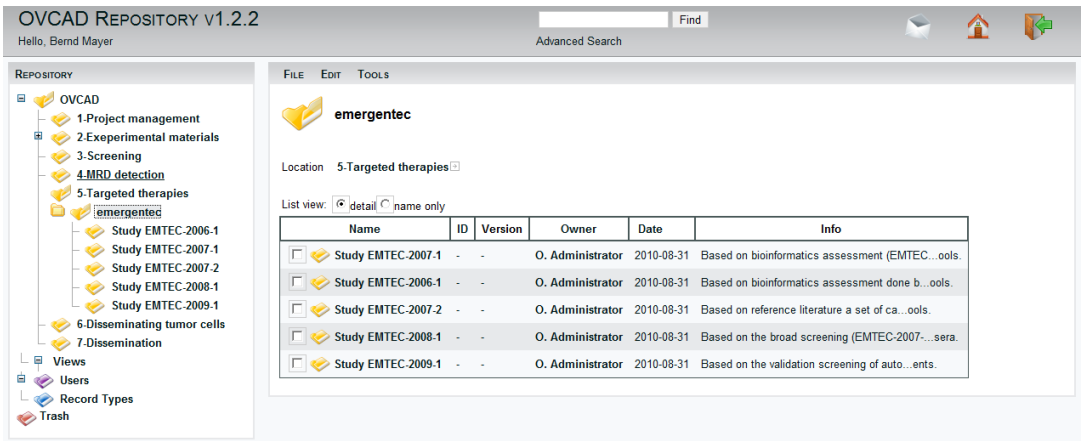

Figure 2: OVCAD data platform: Left: Project structure and assigned OVCAD partners; right: implementation of OVCAD project work (broken down into individual studies) exemplarily shown for EMTEC.

(2) Epigenomic approaches

The number of hypermethylated genes in context of tumour development and progression is growing daily. At the beginning of the OVCAD project, very few epigenetically silenced genes are associated with ovarian cancer, most of which are not very specific and the frequency of hypermethylation is low. Therefore, the objective was defined to discover and validate hypermethylated genes relevant for ovarian cancer progression, with high frequency in ovarian cancer and ideally with a low frequency of methlytion in other caner entities. A group in P1 led by Mechael Krainer was responsible for the discovery and P7 led by Lothar Prix was responsible for the validation of the genes.

Discovering new candidate genes

37 cell lines derived from different type of cancer (12 ovarian cancer, 6 cervical cancer, 4 colorectal cancer, 6 endometrial cancer, 2 lung cancer and 7 breast cancer) were treated either a) mock, b) with 2.5 µM 5-aza-CdR for 72 hours, or c) with 2.5 µM 5-aza-CdR for 48 hours and additionally 24 hours with 2.5 µM 5-aza-CdR plus 0.5 µM TSA. Total RNA was isolated and the transcriptome was assessed on Human Genome Survey Microarrays (Applied Biosystems), which comprise 32.878 probes for the interrogation of 29.098 genes. Microarray data from 111 samples obtained.

After filtration and normalization, two strategies were used to select candidate genes.

- A: To select genes not expressed before treatment (Figure 3):
  - Mock: S/N<2 (signal-to-noise)
  - Calculate change of expression (treated / mock)
  - Inter-gene normalization of change levels
  - Find outliers of all normalized change values (one-sided: increase)
  - Calculate significance for occurrence of outliers in the ovarian group compared to the other tumor group (comprised of all other tumor entities)
- B: To select genes expressed before treatment (Figure 3):
  - Mock: S/N>2
  - Same procedure as above

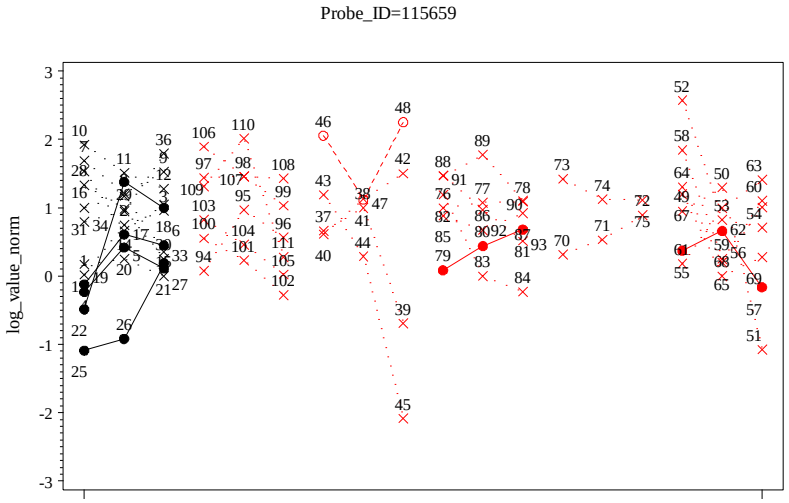

Figure 3. An example showing how a candidate gene was selected with strategy A (bold line: all conditions fulfilled; dotted line: excluded because mock S/N>2; dashed line: no outlier in change of expression; black: ovarian cell line specific; red: for other type of cancer).

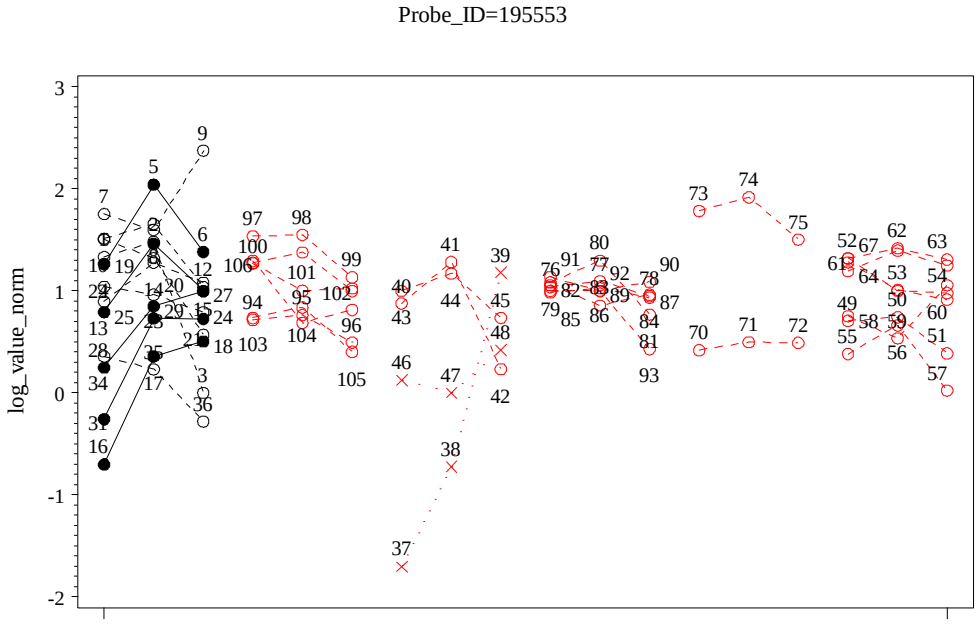

Figure 4. Example showing how a candidate gene was selected with strategy B (bold line: all conditions fulfilled; dotted line: excluded because mock S/N<2; dashed line: no outlier in change of expression; black: specific for ovarian cancer cell lines; red: specific for other type of cancer cell lines).

A list of 131 genes was selected following strategy A, which showed no significant enrichment for genes with CpG-islands but an enrichment for genes with function in cancerogenesis (7 instead of 2 expected).

Table 3. Examples of candidate genes found with strategy A (+: all conditions fulfilled; -: either no outlier or mock S/N>2).

Probe_ID	Number	Outlier Sum	P	Ovary	Other Tumors
178622	7	6.3170295	0.0233452	+--+-++-+++-	----------
186935	4	4.9895149	0.095768	-+-+--+----+	----------
216513	4	1.7174024	0.095768	-++------+-+	----------

A list of 52 genes was selected following strategy B, which showed a significant enrichment for genes with CpG-islands (89% instead of 69% for all genes of the microarray, p = 0.003)

Table 4. Examples of candidate genes found with strategy B (plus: all conditions fulfilled. minus: either no outlier or mock S/N<2).

Probe_ID	Number	Outlier Sum	P	Ovary	Other Tumors
223696	9	131.18272	0.0082111	-+++-++++++-	----------
228532	8	98.236563	0.0140071	+-++-+++-++-	----------
219614	7	75.213383	0.0233452	--+-+++--+++	----------
136738	7	17.90871	0.0233452	+---++-++-++	----------

The hypermethylation status of genes with CpG-islands from both lists, starting with the most significant genes, was further validated.

Validation of candidate genes

1ml of plasma from a total of 270 ovarian cancer patients was used for DNA extraction. The samples were analyzed for promoter-hypermethylation of the five tumor suppressor genes DAPK1, RASSF1, APC, N33 and RUNX3. These five markers were shown to have the highest diagnostic specificity in a study prior to the OVCAD project (Figure 5).

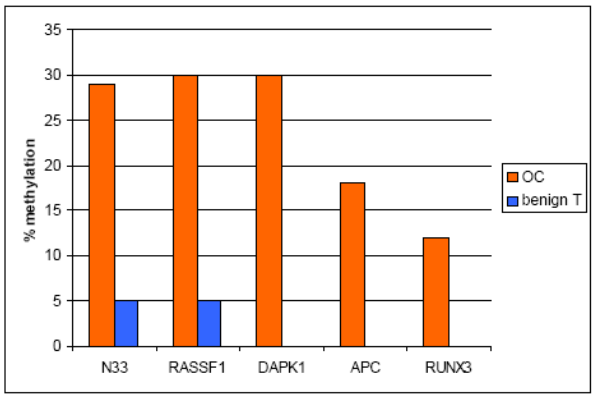

Figure 5: Diagnostic specificity of the methylation markers determined by comparing promotor methylation between primary ovarian tumours and benign/normal ovarian tissues.

Working protocol is shown in Figure 6. In brief:

- DNA was extracted from 800 µl plasma of each of the 270 samples automatically by using Promega DNA-extraction kits in conjunction with a Abbott m24sp robot (152 samples) or manually by using Qiagen DNA-Mini-kits (118 samples).
- PCR of HLA DRA*0102 locus was performed on DNA-preparations to check if sufficient amounts of DNA could have been extracted.
- HLA-PCR positive samples were treated with sodium bisulfite in order to test promoter methylation status by methylation-specific PCR (MSP).
- For quality control, the amplification of marker ACTB (b-actin) was examined on the bisulfite treated samples. ACTB serves as an internal control marker as it is amplified irrespective of promotor methylation (ACTB primers do not cover any CpG dinucleotides), but require successful bisulfite-conversion of the DNA. Native and non-treated-treated DNA is not amplified by ACTB primers. Thus, ACTB allows controlling successful bisulfite conversion and loss of amplifiable DNA during sodium bisulfite treatment.
- Samples which were positive for ACTB-primers were analyzed for promoter-methylation of the 5 tumor suppressor genes.
- The MSP was performed in three duplex-PCR reactions:
  Duplex 1: ACTB (178 bp) + RUNX3 (107 bp)
  Duplex 2: DAPK1 (116 bp) + N33 (156 bp)
  Duplex 3: RASSF1 (191 bp) + APC (118 bp)
  As positive control, a mixture of bisulfite treated DNA of the three tumor cell lines LNCAP, MiaPaCa2 and SW480 was used. Each of the analyzed promoters is hypermethylated in this mixture. DNA from normal lymphocytes was used as negative control.

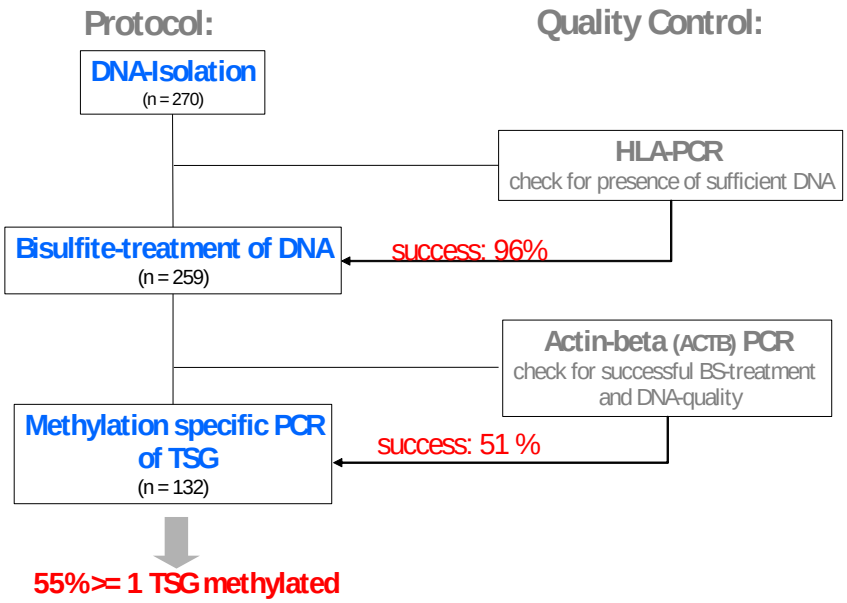

Figure 6: workflow.

From DNA-extracts of the 270 plasma samples, HLA-PCR was positive in 259 samples (96 %). 11 plasma samples did not contain enough DNA or contained inhibitors. The 259 HLA-positive DNA-samples were treated with bisulfite. Only 51% (132/259) samples were positive for ACTB. Presumably, DNA might be damaged by bisulfite treatment, although calf thymus DNA was added to the bisulfite reaction to protect the plasma-DNA.

The analysis of methylation of the tumor suppressor genes DAPK1, RASSF1, APC, N33 or RUNX3 in the 132 ACTB-positive samples showed the following results:

at least one TSG methylated: 55 % of samples
at least two TSG methylated: 16 % of samples
at least three TSG methylated: 4 % of samples
at least four TSG methylated: 2 % of samples
all five TSG methylated: 0 % of samples.

Regarding methylation of the five TSG in the responder and non-responder groups, no differences were found. 50 % and 51% of plasma samples showed at least one methylated TSGs in the non-responder and responder group, respectively. Likewise, no difference between both groups was observed regarding samples with two or more methylated genes. There were also no significant differences regarding particular markers in both groups.

We further validated the candidate markers discovered by partner 1. Bioinformatics was performed to correlate each probe ID to a Genbank RefSeq entry (Panther database, Genbank) in order to obtain the sequence information of the promotor region of the RefSeqs (UCSC Genome Browser) and to examine whether these genes actually contain CpG islands in the vicinity of the promoter region (UCSC Genome Browser, CpG Island Searcher). Of the 92 gene-chip gene identifiers, 63 genes could be unequivocally assigned to RefSeq sequences in Genbank. Of those 63 genes, CpG islands were observed in the promotors of 37 genes.

MSP-assays as duplex reactions for 15 of these 37 genes were designed. Genes, which has functional relevance (e.g. tumor suppressor gene) and which allows appropriate primer design were selected. After proof of principle that the MSPs are functional, the methylation frequency of these markers in ovarian tumour tissues was determined in five most promising markers.

DNA extracted from 54 ovarian tumours (29 non-responders and 25 responders) was used in a training set. Table 5 shows the results of promotor-methylation status .

Table 5. Methylation status of the 15 genes in 54 ovarian tumours.

ACTB(178)	Scotin(133)	EIF3S9(222)	SPATA(157)	WDH1 (203)	CCDC98 (167)	C9ORF (219)	ATP55 (165)
100%	2%	11%	4%	0%	0%	22%	0%

LRP (210)	NELF (166)	DDAH1 (190)	PH-4 (164)	MYLIP (184)	OCEL (118)	ZNF416 (184)	SAMD8 (164)
0%	0%	26%	1%	0%	16%	1%	0%

* The lengths of the amplicons were shown in the blanket.

In contrast to plasma samples, MSP from tissue samples was not restricted by DNA-loss during bisulfite treatment since ACTB control gene could be amplified from all tissue samples. The majority of the 15 tested genes showed methylation frequencies below 10 %. Only two genes (C9ORF and DDAH1) were methylated in >20% of the samples. The gene OCEL was observed to be methylated in 16% of the tested tissue samples.

There was no statistically significant correlation of the methylation frequency with chemoresponse of the patients.

Taking together, in 50% of the plasma samples at least one of the TSG genes is hypermethylated. However, none of these TSG was suitable to allow prediction of clinical responder status. Loss of DNA during bisulfite treatment in almost half of the plasma samples turned out to be a serious problem. The bisulfite treatment step of DNA is a critical bottleneck, because harsh conditions (5M sodium-bisulfite for 4h incubation) must be used to ensure complete conversion. It has been described that under these conditions almost 90% of DNA is degraded. Plasma samples inherently contain low amounts of DNA and when working with bisulfite treatment of DNA obtained from plasma samples, high starting volumes might be needed to obtain sufficient DNA. E.g. the first commercially available diagnostic methylation assay (Septin9 by Abbott Molecular) demands DNA extracted from 10 ml plasma, which is inconvenient to handle for high sample numbers. In contrast to plasma samples, methylation analysis by bisulfite treatment of DNA extracted from tissue samples was successful. Further technical improvement will be needed for improving the detection of methylation in low amount of plasma samples.

(3) Genomic approaches

Comparative genomic hybridization of tumour tissues

Originally, the major objective of the genomic approach was defined to produce high resolution genomic profiles of clinically defined sample sets (25 responsive and 25 non-responsive) of ovarian tumour tissues. Genomic profiles was planed to be

analyzed by means of appropriate mathematical tools (clustering, PCA or ICA) in order to determine the existence of anomalies related to early relapse in ovarian cancer.

P8 was led by Charles Theillet. His group analyzed a total of 128 ovarian tumours by array-CGH. Profiles of genomic gains and losses revealed 18 regions showing numerical aberrations with high significance. These anomalies corresponded to 7 regions of gain (Figure 7A, green) and 11 of loss (red).

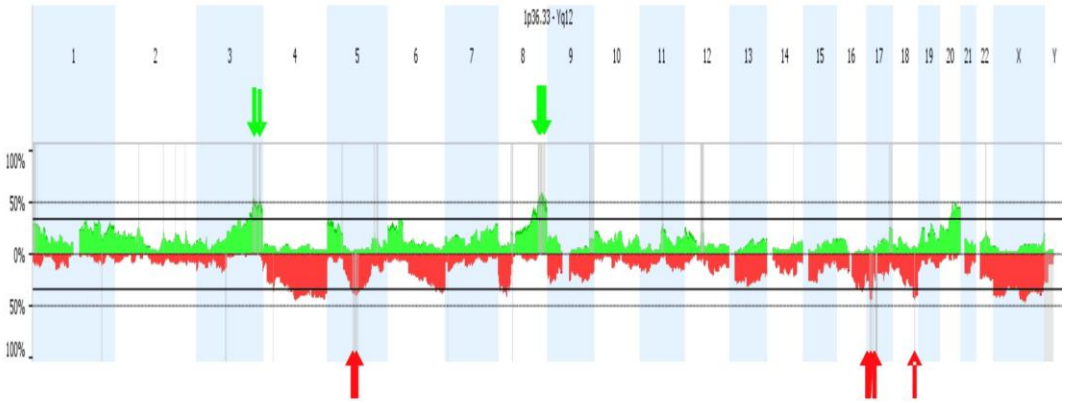

Figure 7: cumulated profiles of copy number alterations in the series of 128 ovarian carcinomas analyzed. Grey bars highlight regions of greatest significance in this dataset.

Data showed that serous adenocarcinomas, which represent about 80% of all ovarian carcinomas, presented different genomic profiles from non-serous carcinomas. This suggested the existence of distinct biological subgroups in ovarian cancer (Figure 8).

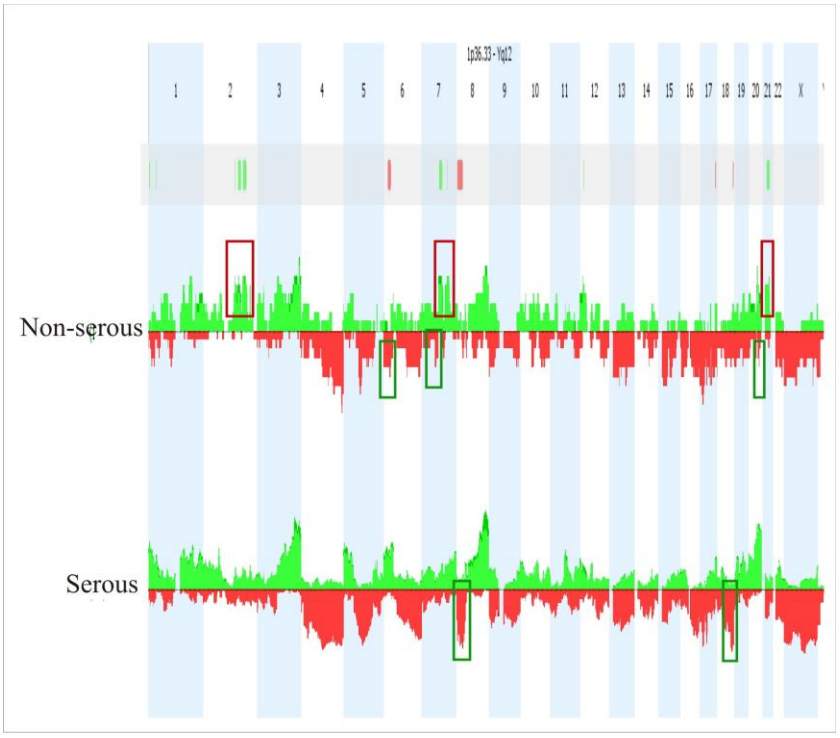

Figure 8: copy number alteration profiles from non-serous ovarian carcinomas differ from serous ones.

Furthermore, the preliminary analyses suggested the existence of specific genomic patterns in tumours associated to long term progression free survival compared to short term survival. Specific sets of high level gains have been identified (Figure 9).

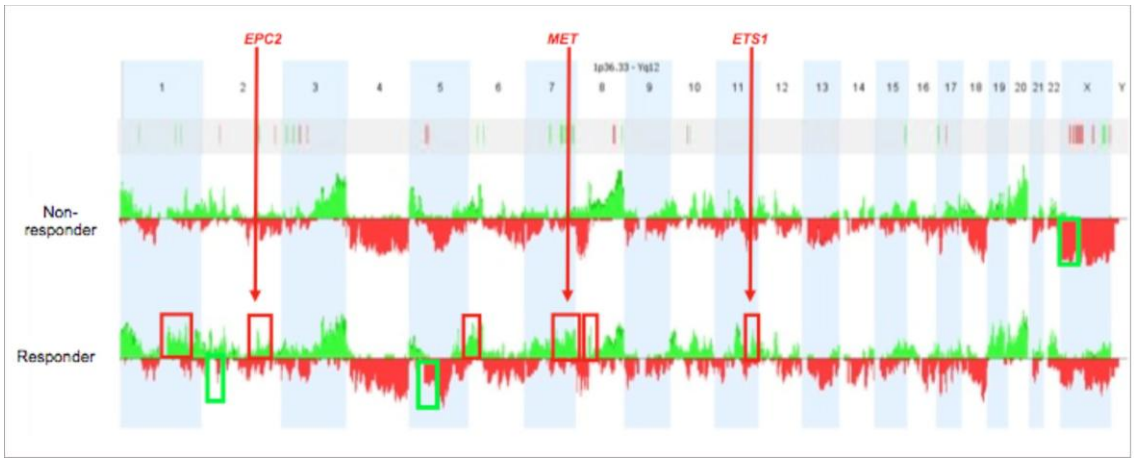

Figure 9: copy number alteration profiles from non-responder ovarian carcinomas show distinct differences with those of responders.

Ovarian tumours were stratified according to their overall level of instability. Four classes were defined, low, median, high, and very high. Kaplan-Meier survival analyses were performed. Surprisingly best outcome was associated to the very high instability group, while the high group presented the worst outcome. These data were unexpected and it may be that very high instability tumours present a better response to therapy than others (Figure 10).

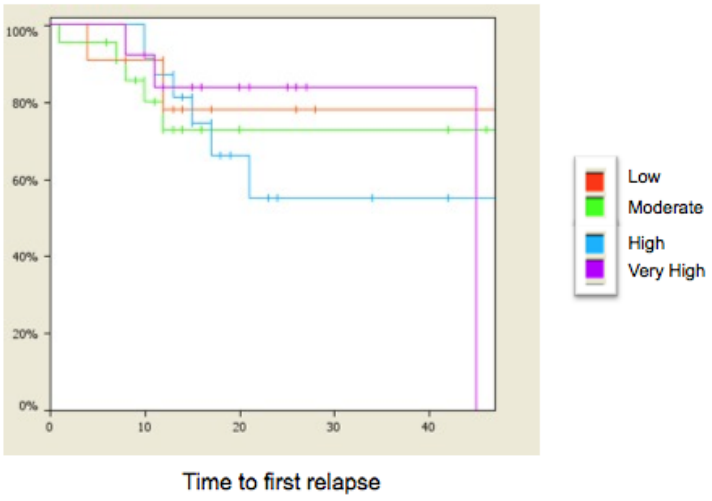

Figure 10: Kaplan-Meier survival curves from ovarian survival curves stratified according to their level of genetic instability. Endpoint was recurrence of the disease.

Of the 128 ovarian carcinomas analyzed by array-CGH, 63 were also analyzed at the transcriptome level by partner 1. Data have been matched and list of genes whose expression levels were significantly modified in correlation to copy number changes were determined. These genes could represent interesting targets for future therapeutical approaches.

One of the interesting regions defined by the CGH array data is on chromosomal 3q26, which showed gain in 63% non-responder patients. This was delivered to partner 16,

led by Burkhard Brandt, who used the marker to characterize the circulating tumour cells.

Analyses are currently being performed in coordination with partner 1 in order to determine possible differences at the genomic level according to the TP53 mutation status and/or the expression of TP53 short isoforms, and K-RAS or RAF mutations. Moreover, data by partner P14 showing altered expression of oncogenic miRNA bore possible leads as well.

Evaluation of mutations in *KRAS* oncogene as predictive marker

K-*ras* is frequently activated by point mutations in various neoplasms. P13 was led by Christian Oberkanins and aimed at detecting the K-*ras* mutations (codon 12 and codon 13) and evaluating their association with ovarian cancer response using the GeneStiX system.

The GeneStix detection system was established and validated for the highly sensitive detection of *KRAS* mutations Ala12 (GGT>GCT), Arg12 (GGT>CGT), Asp12 (GGT>GAT), Cys12 (GGT>TGT), Ile12 (GGT>ATT), Leu12 (GGT>CTT), Ser12 (GGT>AGT), Val12 (GGT>GTT), Asp13 (GGC>GAC) and Cys13 (GGC>TGC). This assay was extended by including the most common *BRAF* mutation V600E. The test combines mutant-enriched PCR based on peptide nucleic acid (PNA) clamping and reverse-hybridization (RH) to nitrocellulose test strips and allows the detection of 1% mutated *KRAS* and *BRAF* with genomic wild-type background.

The mutations of *KRAS* and *BRAF* were analyzed on DNA from fresh frozen tumour tissues, formalin-fixed paraffin-embedded (FFPE) tumor tissue, from blood plasmas and from ascites cells of OVCAD patients. A total of 6.8% of the available OVCAD tumor samples (18/263) were mutated either in *KRAS* (16/263) or in *BRAF* (2/263). A patient was defined as being positive when either DNA from fresh-frozen or from FFPE tumor tissue samples showed a *KRAS/BRAF* mutation. Plasma and ascites samples were tested only if a patient showed positive *KRAS* or *BRAF* mutation in tumour tissues. For the majority of these patients, two plasma samples, i.e. plasmas isolated from the pre-surgery blood and from the blood taken 6 months after the last chemotherapy, were analyzed. None of the *KRAS* or *BRAF* mutations could be detected in the plasma samples. In contrast, 7/10 ascites DNA samples demonstrated the respective *KRAS/BRAF* mutations.

The mean age of KRAS/BRAF positive patients was 51.33 years, the mean age of non-mutated patients 58.74 years (18 [6.8%] / 245 [93.2%]; n = 263; t-test sig. [2-tailed] = 0.013).

Out of 230 serous ovarian tumors, 18 were mutated and 212 were not mutated, whereas *KRAS* or *BRAF* mutations were not found in any of the 33 non-serous ovarian cancer samples. The difference of the *KRAS/BRAF* mutations in serous and non-serous ovarian cancer was not statistically significant (Fisher's exact test = 0.141), probably due to the small sample size.

A statistically significant correlation of *KRAS/BRAF* mutations with tumour grade was found. Despite of being a small cohort, 40% of grade 1 tumours were mutated. The

frequency of *KRAS/BRAF* mutations dropped significantly to 8.8% and 4.9% in grade 2 and grade 3 tumours, respectively (Table 6).

Table 6. Correlation of *KRAS/BRAF* mutation and tumor grading

	Grade 1	**Grade 2**	**Grade 3**	**n**
Non-mutated	6 (60.0%)	52 (91.2%)	173 (95.1%)	231
***KRAS-BRAF* mutated**	4 (40.0%)	5 (8.8%)	9 (4.9%)	18
n	10	57	182	249
Fisher's exact test = 0.02				

A correlation of *KRAS/BRAF* mutations to FIGO stage was not statistically significant. Non-mutated versus mutated cases were FIGO II (12 [92.3%] / 1 [7.7%]), FIGO III (192 [92.8%] / 15 [7.2%]), FIGO IV (40 [95.2%] / 2 [4.8%]) (n = 262; Fisher's exact test = 0.802).There was also no correlation of *KRAS/BRAF* mutations and responder status.

Overall survival (p = 0.412) and disease-free survival (p = 0.189) of *KRAS/BRAF* mutation carriers versus non-mutated patients showed no statistically significant correlation in Mantel-Cox test.
TP53 mutation analysis of 202 OVCAD tissue samples was performed by OVCAD partner 1. The genotype distributions of the mutations in the three genes were as follows: non-mutated, only *TP53* mutated, only *KRAS/BRAF* mutated, *TP53/KRAS/BRAF* mutated are 34 (16.8%), 153 (75.7%), 13 (6.4%), 2 (1%), respectively (n = 202; Fisher's exact test < 0.0001).

Table 7 showed a cohort of 194 samples, which were assigned being grade 1, 2, or 3 tumours. *TP53* mutation frequency accumulated with tumor grading, whereas the *KRAS/BRAF* mutation frequency dropped.

Table 7. Correlation of *TP53/KRAS/BRAF* mutation and tumor grading

	Grade 1	Grade 2	Grade 3	n
Non-mutated	2 (28.5%)	11 (25.0%)	18 (12.6%)	31
Only *TP53* mutated	2 (28.5%)	28 (63.6%)	118 (82.5%)	148
TP53/KRAS/BRAF mutated	0 (0%)	0 (0%)	2 (1.4%)	2
Only *KRAS/BRAF* mutated	3 (43.0%)	5 (11.4%)	5 (3.5%)	13
n	7	44	143	194

In summary, a PCR/reverse-hybridization-based assay has been developed and validated to detect 12 *KRAS* and 1 *BRAF* mutations with 1% sensitivity. 263 OVCAD tumor DNA samples have been examined for *KRAS/BRAF* mutations. Out of these, 18 (6.8%) were positive. *KRAS/BRAF* mutations statistically correlated with age and tumor grade, and were almost absent in *TP53*-mutated tumours. The respective *KRAS/BRAF* mutation was also found in 7/10 ascites DNA samples. No *KRAS/BRAF* mutation was detectable in blood plasma samples.

(3) Approaches on gene expression profiles

Several tasks were defined in the DOW regarding gene expression in ovarian cancer in relation to chemoresponse.

Transcriptomics of ovarian tunours

This task was allocated to P1 lead by the OVCAD coordinator Robert Zeillinger. The objective is to identify tumour gene expression profiles that are significantly associated with the chemo-response of ovarian cancer patients by comparing expression profiles of 50 non-responders tumours with 150 responsive ones.
The transcriptomes from a total of 213 ovarian cancer tissues were performed using Applied Biosystems Human Genome Survey Microarrays V2.0. 9 samples were excluded after the final clinical data were delivered. Data were filtered, quantile normalized, and log-2 transformed according the R-script ABarray. After quality control by means of average signal, number of genes above signal-to-noise (S/N) ratios of 3 (|>5,400) and a principal component analysis (PCA), nine samples were excluded for further analysis because of their very low average signal and unusual expression profile (Figure 11).

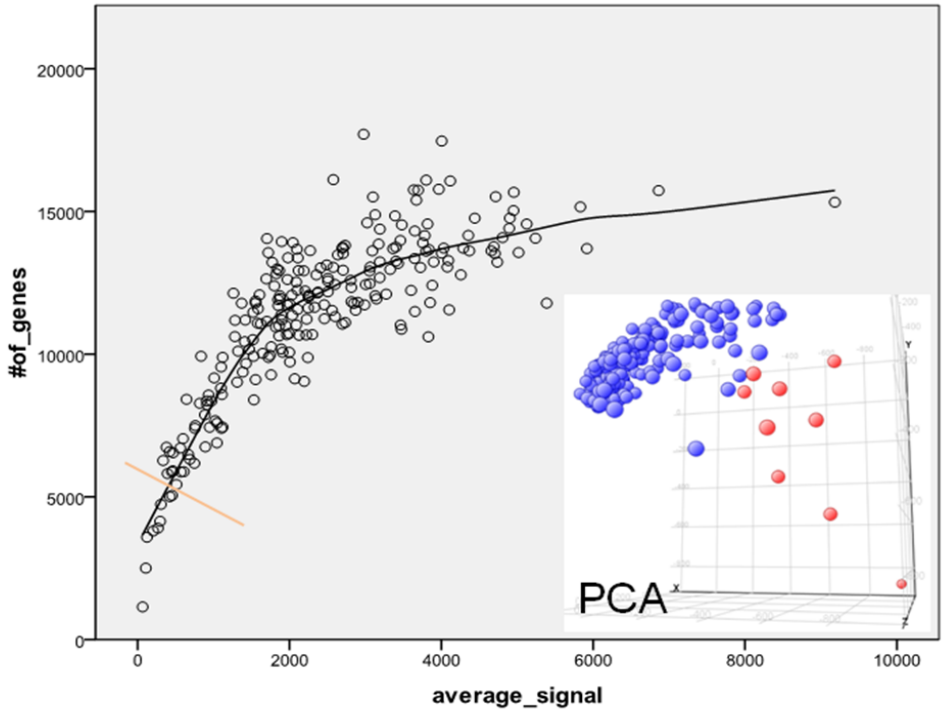

Figure 11. Quality evaluation of the microarray data. Samples with lower than 5400 detetable genes (S/N>3) were excluded. Theses samples also showed usual expression by PCA analysis – red labelled.

Table 8. Clinical and pathologic characteristics of this subset of the 195 tumours

	Number of patients	%
Histological type		
endometrioid tumour	5	3
Mmixed epithelial tumour	7	4
Mucinous tumour	3	2

Serous tumour	172	88
Undifferentiated tumour	8	4
Histological grade		
G1	7	4
G2	42	22
G3	146	75
FIGO stage		
II	9	5
III	153	78
IV	31	16
unknown	2	1
Rest tumour		
no residual tumour	137	70
0 - 1cm	36	18
> 1cm	21	11
unknown	1	1
Responder		
yes	146	75
no	46	24
unknown	3	2
Total	195	100

A binary logistic regression with the categorical responder status (Table 9), two cox regression analyses for disease free survival (DFS, Table 10) and for overall survival (OS, Table 11) using all clinicopathologic parameters are shown.

Table 9. Binary logistic regression with responder status as dependent variable

	Binary Logistic Regression				Multiple Logistic Regression			
	Exp(B)	CI 95%		P	Exp(B)	CI 95%		P
Age	**1.04**	1.01	1.07	**0.02**	**1.03**	1.00	1.07	**0.05**
FIGO stage	**2.24**	1.07	4.70	**0.03**	2.01	0.90	4.48	0.09
Grade	2.11	0.93	4.76	0.07				
Histology (non-ser vs ser)	0.92	0.32	2.64	0.87				
Residual Tumor	**1.72**	1.09	2.71	**0.02**	1.56	0.96	2.53	0.07
Type of Chemotherapy								
Neoadjuvant	**1.00**				**1.00**			
Adjuvant	**0.34**	0.15	0.76	**<0.01**	**0.42**	0.18	0.99	**0.05**
Intraperitoneal adjuvant	**0.07**	0.01	0.61	**0.02**	**0.10**	0.01	0.82	**0.03**

Tabel 10. Cox regression analysis with censored DFS data as dependent variable

	Univariate Cox Regression				Multiple Cox Regression			
	Exp(B)	CI 95%		P	Exp(B)	CI 95%		P
Age	1.01	1.00	1.03	0.09				
FIGO stage	**2.06**	1.40	3.04	**<0.01**	**1.75**	1.16	2.64	**0.01**
Grade	**1.66**	1.11	2.48	**0.01**	1.39	0.94	2.06	0.10
Histology (non-ser vs ser)	1.10	0.65	1.87	0.72				
Residual Tumor	**1.80**	1.41	2.31	**<0.01**	**1.65**	1.29	2.13	**<0.01**
Type of Chemotherapy								
Neoadjuvant	**1.00**				**1.00**			
Adjuvant	**0.51**	0.33	0.78	**<0.01**	**0.61**	0.39	0.95	**0.03**
Intraperitoneal adjuvant	**0.36**	0.17	0.75	**0.01**	**0.41**	0.19	0.85	**0.02**
Responder (no vs. yes)	**20.53**	12.67	33.26	**<0.01**	excluded			

Table 11. Cox regression analysis with censored OS data as dependent variable

	Univariate Cox Regression				Multiple Cox Regression			
	Exp(B)	CI 95%		P	Exp(B)	CI 95%		P
Age	**1.03**	1.01	1.06	**0.01**	**1.03**	1.00	1.06	**0.03**
FIGO stage	**1.81**	1.03	3.19	**0.04**	1.83	0.96	3.48	0.07
Grade	**2.33**	1.16	4.69	**0.02**	**2.18**	1.08	4.40	**0.03**
Histol. (non-ser/ser)	1.33	0.65	2.72	0.43	**2.27**	1.05	4.93	**0.04**
Residual Tumor	**1.78**	1.28	2.49	**<0.01**	**1.62**	1.15	2.28	**0.01**
Type of Chemotherapy								
Neoadjuvant	1.00				excluded			
Adjuvant	0.64	0.36	1.16	0.14				
Intraperitoneal adjuvant	no events							
Responder (no vs. yes)	**9.40**	5.44	16.25	**<0.01**	excluded			

The results demonstrated that only age of patients, residual tumor and type of chemotherapy were independent predictors for responder status or DFS. But all clinicopathologic parameters except FIGO stage were independent predictors. FIGO stage did not show any predictive power is probably due to the exclusion of FIGO I patients in OVCAD project.

For all clinicopathologic parameters, a significance analysis of microarrays (SAM) after filtering out of genes with expressions below S/N=2 in either 50% of all samples (age, OS, DFS) or in 75% of samples in more than 50% of the used categories (grade, histology types, FIGO stage, and responder status) was performed. A summary is shown in Table 12.

Table 12. SAM analyses of the transcriptomes of 204 ovarian cancer tissues

Factor	Included serous samples	Dependent	**Sign. Genes**	FDR	Up	Down
Age	172	Numeric [26 - 85 yrs]	**1,000**	10%	981	19
Grade	165	1/2 vs 3 [42 vs 123]	**738**	10%	357	381
Histology[1]	204	5 Categories	**17**	12%	n.a.	n.a.
FIGO stage	172	III vs IV [140 vs 32]	-	>40%	-	-
Overall Survival	195	Censored OS, 57 events	**73**	20%	73	-
Disease Free Survival	195	Cens. DFS, 124 events	8	38% !	8	-
Response to Chemoth.	192	Yes vs No [146 vs 46]	-	>40	-	-

[1]only very few samples in the four non-serous categories and no clear cell tumors.

As seen in Table 12, for FIGO stage, DFS, and responder status, no significant genes were found, indicating no substantial biological differences between primary tumors with different FIGO stages, and no predict power of gene expression levels in tumor tissues on DFS and responder status. However, age, grade, and histology yielded significant different expressed genes. The outcome OS yielded 73 significantly different expressed genes, even with a rather low number of events (57).
Nevertheless, a 73 gene list is too small for a significant meaningful functional analysis. Thus we expanded these genes by their first protein-protein-interaction partners and subsequent built protein interaction networks of these expanded protein list. 64/73 genes were annotated in the Interologous Interaction Database (I2D). Using these 64 proteins as seeding proteins for network building, we got four networks, one with 652 proteins and three with each 2 proteins (Figure 10). This is significant less ($p=0.001$) than expected by chance (as control 1000 networks with 64 randomly chosen seeding proteins were built, leading to a Gaussian distribution of built networks with a mean of 28 networks and a standard deviation of 5.5; the smallest number of built networks was 12).

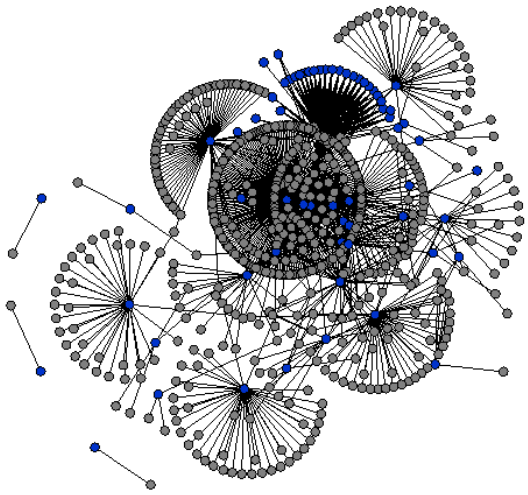

Figure 12. Four protein-protein interaction networks.

Using these 658 network-proteins as gene list for a Database for Annotation, Visualization and Integrated Discovery (DAVID) analysis, clusters for actin binding, cell adhesion, and the extracellular matrix were significantly overrepresented.

Annotation Cluster 1	**Enrichment Score: 38.59**			**Count**	**P_Value**	**Benjamini**
SP_PIR_KEYWORDS	actin-binding	RT		85	1.4E-63	7.5E-61
GOTERM_MF_FAT	actin binding	RT		104	1.2E-61	8.2E-59
GOTERM_MF_FAT	cytoskeletal protein binding	RT		124	8.9E-60	3.1E-57
GOTERM_CC_FAT	actin cytoskeleton	RT		82	3.8E-48	1.8E-45
SP_PIR_KEYWORDS	cytoskeleton	RT		93	2.3E-35	6.1E-33
GOTERM_CC_FAT	cytoskeleton	RT		158	2.2E-34	5.1E-32
GOTERM_CC_FAT	intracellular non-membrane-bounded organelle	RT		193	1.7E-18	8.0E-17
GOTERM_CC_FAT	non-membrane-bounded organelle	RT		193	1.7E-18	8.0E-17
GOTERM_CC_FAT	cytoskeletal part	RT		91	5.9E-14	1.0E-12
Annotation Cluster 2	**Enrichment Score: 38.19**			**Count**	**P_Value**	**Benjamini**
GOTERM_BP_FAT	actin filament-based process	RT		71	8.6E-41	2.7E-37
GOTERM_BP_FAT	cytoskeleton organization	RT		90	2.3E-38	3.6E-35
GOTERM_BP_FAT	actin cytoskeleton organization	RT		66	1.3E-37	1.4E-34
Annotation Cluster 3	**Enrichment Score: 21.35**			**Count**	**P_Value**	**Benjamini**
GOTERM_BP_FAT	cell adhesion	RT		91	3.6E-23	2.8E-20
GOTERM_BP_FAT	biological adhesion	RT		91	4.0E-23	2.5E-20
SP_PIR_KEYWORDS	cell adhesion	RT		57	6.4E-20	3.1E-18
Annotation Cluster 4	**Enrichment Score: 17.21**			**Count**	**P_Value**	**Benjamini**
SP_PIR_KEYWORDS	extracellular matrix	RT		52	1.1E-27	9.9E-26
GOTERM_CC_FAT	extracellular matrix	RT		67	2.1E-26	3.2E-24
GOTERM_CC_FAT	extracellular region part	RT		115	5.9E-26	6.8E-24
GOTERM_CC_FAT	proteinaceous extracellular matrix	RT		61	1.4E-23	1.3E-21
SP_PIR_KEYWORDS	triple helix	RT		20	2.5E-21	1.5E-19
SP_PIR_KEYWORDS	Secreted	RT		128	9.0E-21	4.7E-19
SP_PIR_KEYWORDS	hydroxylysine	RT		19	1.2E-19	5.1E-18
SP_PIR_KEYWORDS	hydroxyproline	RT		20	2.6E-19	1.1E-17
SP_PIR_KEYWORDS	hydroxylation	RT		25	8.8E-19	3.3E-17
SP_PIR_KEYWORDS	trimer	RT		17	3.4E-18	1.2E-16
GOTERM_CC_FAT	extracellular matrix part	RT		32	3.8E-17	1.3E-15
UP_SEQ_FEATURE	region of interest:Triple-helical region	RT		15	6.2E-16	6.7E-13
GOTERM_MF_FAT	extracellular matrix structural constituent	RT		27	1.4E-15	3.3E-13
GOTERM_CC_FAT	collagen	RT		18	5.6E-15	1.2E-13
SP_PIR_KEYWORDS	collagen	RT		23	1.8E-13	4.4E-12
INTERPRO	Collagen triple helix repeat	RT		22	1.1E-12	5.5E-10
GOTERM_CC_FAT	basement membrane	RT		22	3.8E-12	5.2E-11
GOTERM_BP_FAT	collagen fibril organization	RT		12	8.4E-9	3.4E-7
SP_PIR_KEYWORDS	basement membrane	RT		12	2.3E-8	3.5E-7

Figure 13. Overrepresented functional clusters derived from a DAVID analysis using the 658 network-proteins as query gene list.

Focal adhesion was the most significant overrepresented pathway (Figure 14).

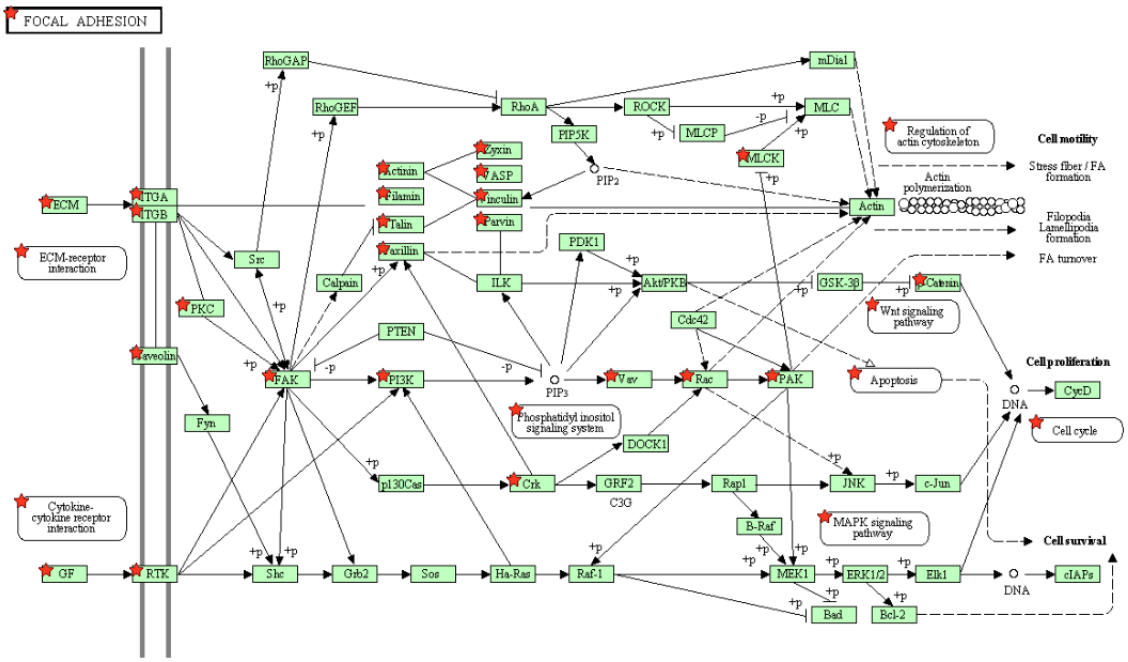

Figure 14. Proteins from the focal adhesion pathway overrepresented in the 658 network built from the 73 significantly de-regulated genes involved in overall survival.

Taking together, disease free survival and responder status revealed no significant deregulated genes in tumor tissues, indicating no extensive expressional differences between tumor tissues from patients with early and late recurrences. This is in accordance with the analysis of clinicopathologic parameters, where only age (a systemic factor of the patient) and type of chemotherapy were independent predictors for DFS and responder status, but not the biological meaningful factors like grade, FIGO, or histology. Nevertheless, proteins from the cytoskeleton and the extracellular matrix including the focal adhesion pathway were overrepresented from the deregulated genes involved in overall survival.

Gene expression signatures in ovarian tumours

P14 was led by Els Bern. This group had discovered a set of 9 genes, which were differently expressed between the responsive and resistant ovarian tumours treated with cisplatin. The objectives in OVCAD were to measure the expression of these 9 genes in all tumours and to analyze its predictive impact on the response of ovarian cancer patients to the standard treatment.

The nine genes (Fibronectin 1, FN1, topoisomerase II alpha, TOP2A, Lamin B Receptor, LBR, Serine/threonine kinase 6/aurorakinase 6, STK6, collagen type 3 alpha 1, COL3A1, argininosuccinate synthetase, ASS, Sphingosine-1-phosphate phosphatase, SGPP1, integrin alpha E, ITGAE, proliferating cell nuclear antigen, PCNA) and the an extracellular metrix (ECM)-gene-signature (FN1, COL3A1, collagen type IV alpha 2, COL5A2, succinate dehydrogenase B, SDHB, arachidonate 5-lipoxygenase, ALOX5, annexin A4, ANX4, CD59 antigen, CD59, calreticulin, CALR) involved in cisplatin resistance, were quantified using RT-PCR as described before (Helleman et al, Int J Cancer 118:1963-71, 2006).

The cDNA of RNA from the OVCAD specimens was prepared and tested for qRT-PCR. The expression level of these genes has been measured by quantitative RT-PCR in 229 OVCAD ovarian cancer specimens. Of these 219 were informative (Ct ranges from 15-26) according to the expression of the housekeeper genes HPRT, PBGD and B2M. An exploratory unsupervised clustering of the gene expression values showed a random distribution of the tumours collected in the different institutes, which indicated that there is no institute bias.

Computerized clinical data were available on 200 patients: response data on 142 and PFS on all 200 patients. COL3A1, ITGEA, PCNA, CD59 and COL5A2 were significantly associated with response (t-test, $p<0.05$). However, none of the genes were associated with progression free survival (PFS), categorized as PFS 6, 6-12, and >12 months after last treatment of chemotherapy.

The differences observed can be explained by different distribution in the original and the OVCAD study, i.e. histology (more non-serous vs. pure serous), FIGO stage (more early stage vs. pure advanced), residual tumours, grade as well as different platinum based chemotherapy (cisplatin and endoxan vs. carboplatin and taxanes) and response criteria between the original and the OVCAD study design.

During the OVCAD time, the group also performed a pathway analysis on nine published gene sets associated with platinum resistance in ovarian cancer, including the 9 gene set. Gene Ontology (GO) analysis and Ingenuity Pathway Analysis (IPA)

were performed to determine which functional processes were differentially represented in the combined gene lists of the nine studies (457 genes) compared to all Unigene identifiers or the Ingenuity knowledge base. 23 gene networks were generated. 13 GO processes, 71 canonical pathways, eight toxicity pathways and 74 biological functions are significantly associated with the 9-study gene set (Gynecologic Oncology 117:170-176, 2010).

Analysis of microRNAs (miRs) in tumour tissues

Since 2006, an increasing number of studies have indicated an essential role for miRs in ovarian cancer regarding both tumorigenesis and resistance. Although the targets of most miRs are still under investigation, P14 described putative interesting miRs, which may associate with ovarian cancer prognosis and/or therapy response (Helleman et al. Gynecol Oncol 117:170-6, 2010; Helleman et al. Int J Biochem and Cell Biol 42:25-30, 2010).

Six miRs have thus been selected for analyses in 229 OVCAD samples: miR34a/b/c, related to TP53 activity, miR200c, related to epithelial mesenchymal transition, miR214, targets PTEN activity, miR335, targets TNC activity, and control RNUs. An additional project was performed using biological materials from OVCAD.

MiR-34b and -c were significantly associated with response and PFS (t-test, $p<0.05$). Moreover, miR34-c retained significance for PFS ($p=0.042$), but did not show any association with response in Wilcoxon test.

In conclusion, for serous ovarian cancer the miR family, especially miR34-c, is a likely candidate for response and PFS prediction to carboplatin-taxanes based chemotherapy. As discussed during the final OVCAD meeting 2010, it is advised to integrate the available data of *TP53* mutation/functional activity and its downstream genes (cyclin D-E, CDK4/6, cMYC, E2F3, MET, BCL2) from the OVCAD project. The resulting algorithm may substantiate the role of the miR34 family in therapy resistance.

Gene expression profiles of peripheral blood mononuclear cells (PBMC)

Tumourigenesis and cancer progression does not only leave traces in tumour tissues, they are also reflected by the host immune active cells and possible disseminated tumour cells. It has been shown that PBMCs from renal cell carcinoma patients has specific mRNA expression signature different from that from healthy subject. It was also indicated that different types of tumour might have different gene expression profiling of PBMC. Thus, one objective was defined to investigate biological signatures of PBMC, presumably reflecting the patients' immune response against ovarian cancer. P1 led by Robert Zeillinger aimed at comparing gene expression profiles of 25 samples from patients responsive to chemotherapy with that of 25 samples of resistant patients using high density microarray technology. After statistical analysis, the results should be validated using RT-PCR.

ABI microarrays of 48 PBMC samples (22 responders, 23 non-responders, 3 not defined; 27 with recurrence; 12.5 months median follow up ranging from 1 - 41 months) were obtained.

After the filtration of raw data in regard to the average expression level and quality of the arrays and correction of batch-effect, gene expression values from 15,143 ProbeIDs were Log2-transformed and quantile normalized. Two methods were employed for the selection of markers, which could be used in the prediction of responder and non-responder patients.

Lasso (L1 norm restricted Cox regression analysis) uses censored disease free survival (DFS) data with significance analysis of microarrays (SAM) pre-selection (FDRs: 5%, 10%, 20%, no threshold) and leave-one-out cross-validation during multivariable model building and .632 bootstrap estimation to assess the predictive information (Table 13). The difference of the responder and non-responder is shown in Figure 15.

Table 13. Gene-models selected by the Lasso method

Pre-selection	Selected genes	.632	P-value	Used
30; FDR 5%	9	27.4%		no
137; FDR 10%	**9**	**31.2%**	**0.118**	**yes**
281; FDR 20%	16	25.1%		no
15,085	**20**	**23.5%**	**0.248**	**yes**

➢ U

SC (Uncorrelated Shrunken Centroids) uses the categorical responder status with M-fold cross-validation during shrinkage (delta) and correlation threshold (rho) determination (Table 14).

Table 14. Gene-model selected by the USC method

Selected Genes	CV Mistake	Avg. Genes	Delta	Rho
25	5	17	1	0.5

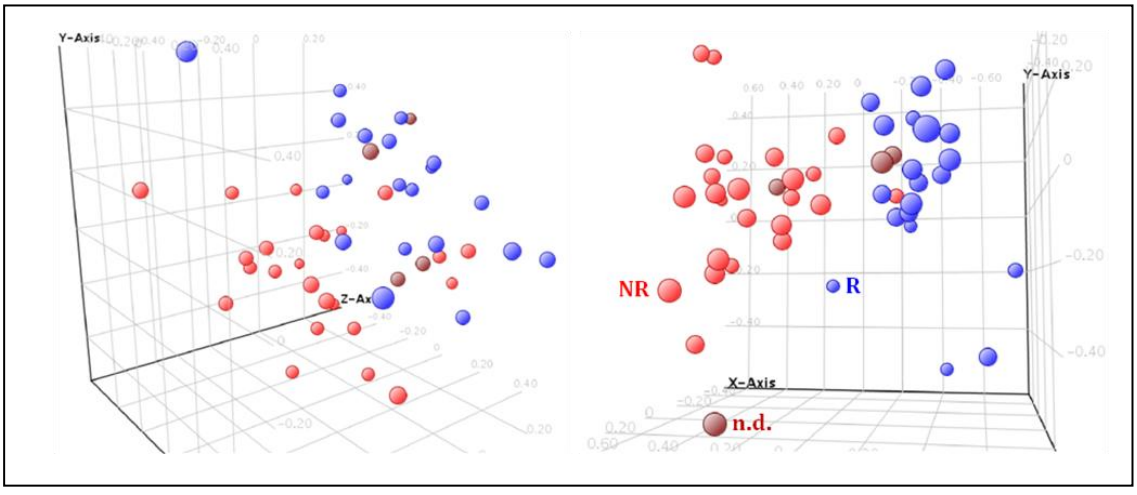

Figure 15. Principal component analysis of the 20 gene lasso-model (left) and the 25 gene USC-model (right). Red: non-responder; blue: responder; brown: not identified.

Expression of 49 selected genes and further 38 genes from other projects were determined by RT-qPCR and normalized to the geometric mean of three stable expressed genes. Since the results generated from RT-qPCR did not always correlated

with microarray data, a second step of marker selection using SAM with either the censored DFS or the categorical responder status as dependent variable and a FDR cut-off of 15% was performed, which yielded 47 significant genes.

The expression of these 47 genes was determined in 212 samples from OVCAD patients, comprising 158 responders (75%) and 54 non-responders (25%). No predictive model could be built with lasso and the categorical responder status as dependent variable. But models were built with either (a) five clinical parameters (age, histology type, FIGO stage, grade, residual tumor size) and the expression of 47 genes (Table 15) or (b) the five clinical parameters alone using censored DFS as dependent variable. Cross-validated proportions of explained variation (PEV) of these two models were 0.159 for model (a) and 0.108 for model (b), respectively estimated by the .632 bootstrap method. An increase of 47.2% predictive power can be shown by adding the expressions of three genes in PBMCs of patients to the known clinical parameters.

Table 15. Final Cox regression model built from five clinical parameters and the expressions of 47 genes using lasso

Factor	Type	B	HR	P
FIGO	Clinical	0.367	1.444	0.063
Grade	Clinical	0.502	1.652	0.008
Residual Tumor	Clinical	0.379	1.461	<0.001
CETP	Gene	0.243	1.275	0.007
ZNF419	Gene	-0.095	0.909	0.003
GP1BA	Gene	-0.186	0.830	0.019

In conclusion, PBMCs is a useful source for the prognosis of ovarian cancer.

(4) Proteomics approaches and analyses of candidate proteins and autoantigens

The SELDI-TOF MS technology applies to serum or plasma samples as well as to tissue samples allows protein profiling to be correlated to clinical parameters. The main objectives at the protein level in the OVCAD project are to identify a robust protein profile, which is able to differentiate responsive patients from non-responsive ones.

Proteomic analysis of tumour tissues

This task was performed by Partner 3, led by Ignace Vergote. Tumour tissues were obtained from the clinical partners and prepared for laser microdissection and SELDI-TOF MS analysis according to our previously defined protocol (Cadron et al. Anticancer Res 29:1039-45, 2009). Of the first 100 samples analysed, 78 samples contained enough tumours, which enabled the isolation of 30.000 tumour cells for analysis on CM10 and IMAC30 chips.

The clinical data of these patient samples are given in Table 16. In regard to platinum sensitivity, three groups were defined: the extreme sensitive group with relapse > 12 months after the end of therapy, the intermediate sensitive group with relapse within 6 to 12 months, and the resistant group who relapsed within 6 months after the end of therapy.

Table 16: Clinical characteristics of OVCAD samples

	n	%
Platinum free interval		
< 6 months	19	24
6-12 months	23	29
>12 months	36	46
CR	55	71
Primary debulking	62	80
Stage		
II	4	5
III	63	81
IV	11	14
R0	52	67
Serous Histology	65	83
Grade		
I	3	4
II	20	26
III	52	67
Median Age	60	
Range	36-83	
Total	78	

After laser microdissection, cells were lysed for 60 min at 4°C with 50 µl U9 buffer followed by filtration and dilution in 200 µl binding buffer and nanosep MF device. Subsequently lysates were analysed on CM10 and IMAC30 ProteinChip arrays. Samples were randomly spotted in triplicate. On every array a quality control sample was randomized between samples to assess reproducibility. The coefficient of variation (CV) was calculated for 4 peaks and a pooled CV for CM10 and IMAC30 arrays were 20% and 21% respectively.

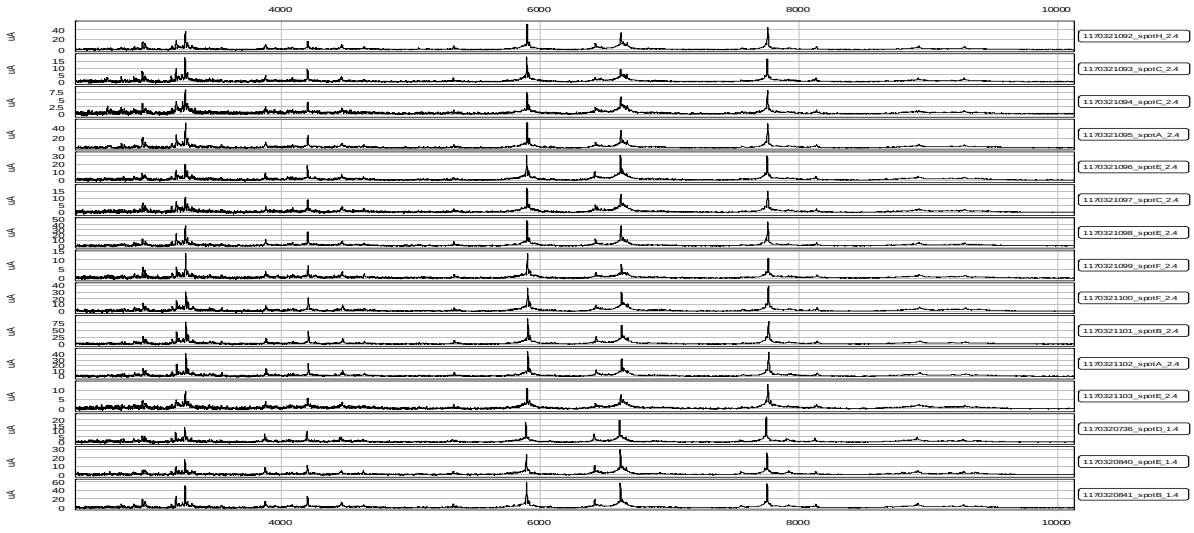

Figure 16. Intra-assay reproducibility of reference samples.

Mass analysis was performed using SELDI-TOF MS (PCS 4000 Enterprise, Ciphergen ProteinChip Reader Inc. Fremont, CA, USA) according to an automated data collection protocol for a molecular weight range of 0 - 30.000 Da. The following settings were used: (a) laser intensity of 3.500 nJ; (b) focus mass 10.000 Da; (c) matrix attenuation 500 Da; (d) sampling rate 400 MHz; (e) 2 warming shots (not included in analysis). 10 data shots per point and (f) Total number of points evaluated equal to 25% of the spot surface. Mass accuracy was calibrated externally using the

all-in-one peptide standard according to the manufacturer's protocol (Bio-Rad. Nazareth. Belgium). Using the Ciphergen Express Software, calibration, baseline subtraction and noise reduction were completed before peak intensities were normalized to the total ion current followed by alignment of the detected peaks. Outlier spectra were identified and removed from analysis when the normalisation factor deviated more than 2 standard deviations. Numeric data were exported to Excel files for further biostatistical processing.

Subsequently unsupervised peak detection and peak clustering with MASDA software were performed:
- peak detection per sample
- peak filtering per sample
*MAD = all peaks below a local noise threshold estimated by a robust local estimator (median) plus five times its median absolute deviation are filtered out
*Std = all peaks below a local noise threshold estimated by a robust local estimator (mean) plus five times its standard deviations are filtered out
- Complete linkage hierarchical one-dimensional clustering for the detection of peak clusters

On CM10 chip arrays, 492 peak clusters were detected. Seventy-four peaks were differentially expressed between the sensitive (PFI > 6 months) and the resistant group (PFI < 6 months) with a p-value < 0.05. Eighty-one peaks were differentially expressed between the intermediate and the resistant group and 42 peaks between the extreme sensitive and resistant group ($p < 0.05$). On IMAC30 chips, 387 peaks were detected. Twenty peaks were differentially expressed between the sensitive (PFI > 6 months) and the resistant group (PFI < 6 months) with a p-value < 0.05. Thirty-seven peaks were differentially expressed between the intermediate and the resistant group and 1 peak between the extreme sensitive and resistant group ($p< 0.05$). Of these, some of the peaks found in our pilot study remained statistically significantly differentially expressed (Figure 17 and Figure 18). Other peaks of interest found were in the m/z region 4900-5100 and 10000 Dalton.

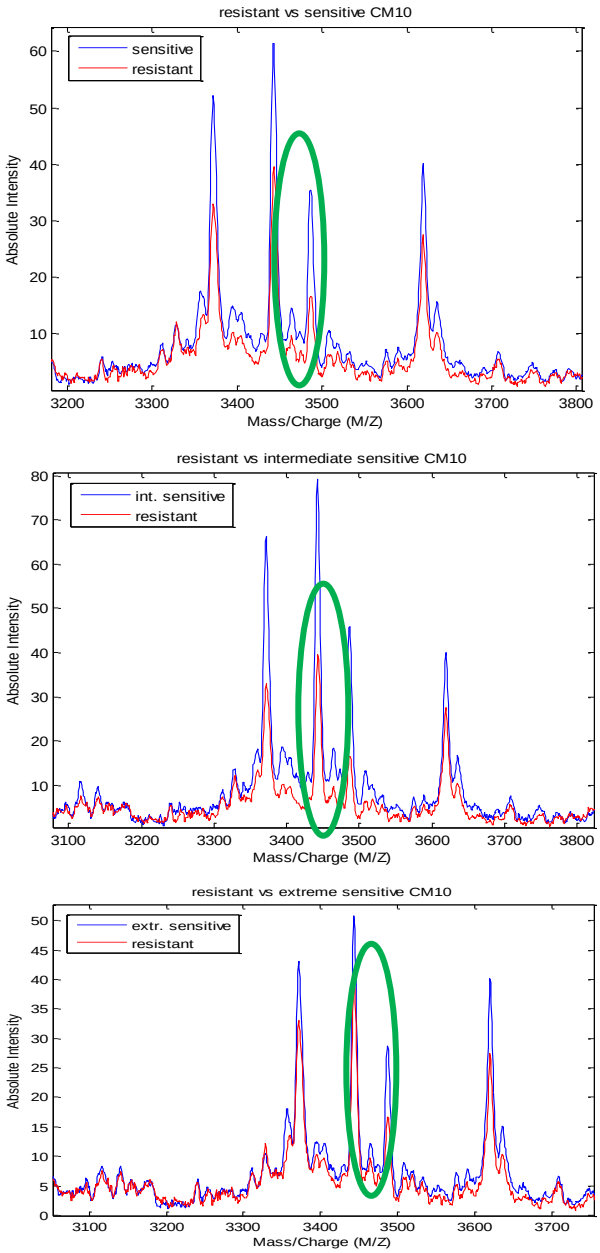

Figure 17: Average spectrum of the platinum sensitive (blue) and resistant (red) samples on CM10 arrays, zooming on the m/z value 3650. The x-axis shows the mass/charge (m/z) ratio and Y-axis the relative intensity.

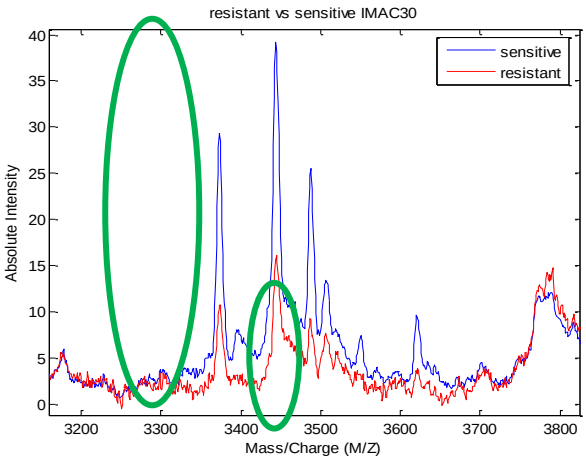

P-value = 0.03, 0.05, 0.04

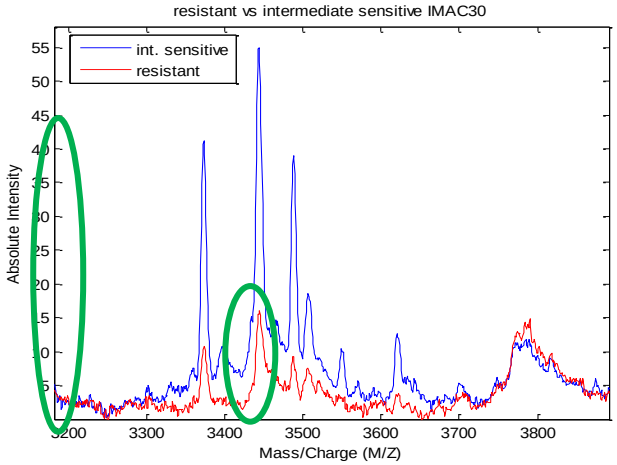

P-value = 0.034, 0.03

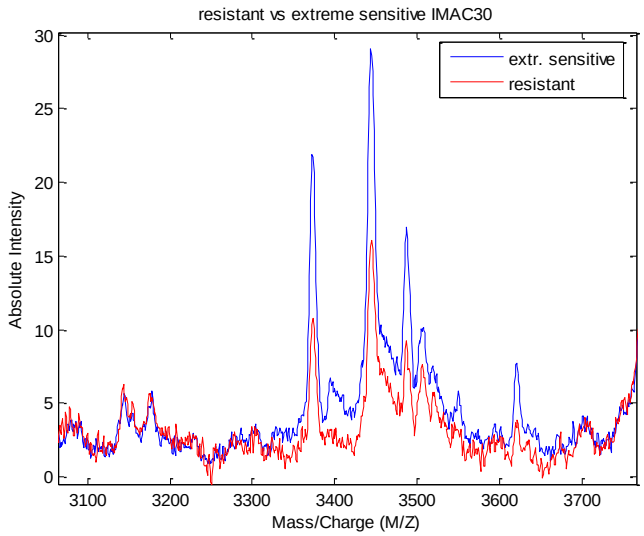

Figure 18: Average spectrum of the platinum sensitive (blue) and resistant (red) samples on IMAC30 arrays, zooming on the m/z region 3100-3700. The x-axis shows the mass/charge (m/z) ratio and Y-axis the relative intensity.

When platinum sensitivity was considered as a continuous interval, 24 peaks on CM10 arrays were related with platinum sensitivity with a p-value of 0.01 to 0.04 (Figure 19).

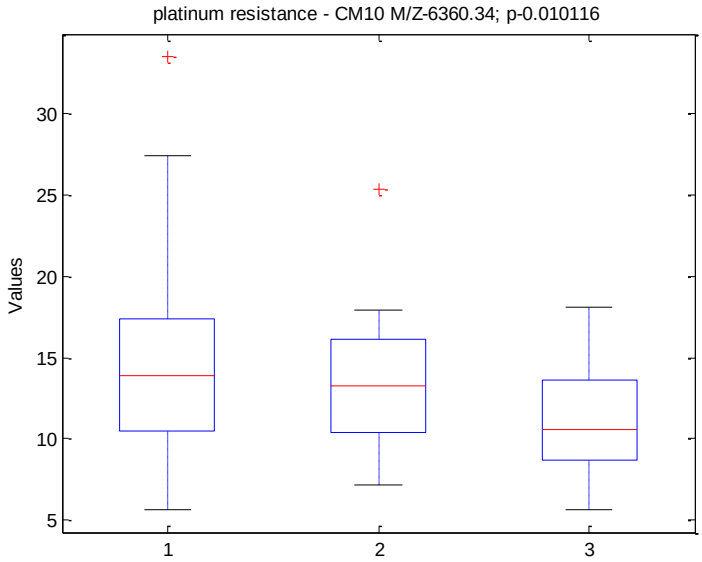

Figure 19: Box blot of the intensity of m/z value 6360 on CM10 arrays for 1: resistant group. 2: intermediate sensitive and 3: extreme sensitive samples.

Consequently, a model was created based on these results to classify samples according to platinum sensitivity based on a leave-one-out cross validation with weighted Least Squares Support Vector Machine (LOO-wLSSVM).

Table 17. Model building with LOO-wLSSVM

Outcome	LOO AUC	N peaks	Chip	Threshold
Resistant *vs.* sensitive	0.7591	35	CM10	std
Resistant *vs.* intermediate sensitive	0.8421	7	IMAC30	std
Resistant *vs.* sensitive (> 12 months)	0.9108	2	IMAC30	MAD
Intermediate *vs.* sensitive (> 12 months)	0.9710	12	CM10	std

In the validation study, 80 patients' samples were processed with laser microdissection, of which 62 were evaluable for platinum response, histopathology and clinical parameters. They were subsequently analysed on CM10 and IMAC30 chips.

The clinical data of these patient samples are given in Table 18. In relation to platinum sensitivity, three groups were defined. The extreme sensitive group with relapse > 12 months after the end of therapy, the intermediate sensitive group with relapse within 6 to 12 months and the resistant group who relapsed < 6 months after the end of therapy.

Table 18: Clinical data of OVCAD samples used to validate protein profiles

	n	%
Platinum free interval		
< 6 months	11	18
6-12 Months	12	19
>12 months	39	63
CR	54	81
Primary debulking	62	95
Stage		
II	3	4
II	51	76
IV	13	19
R0	51	76
Serous Histology	61	91
Grade		
I	1	1
II	10	15
III	50	75
Median Age	54	
Range	27-84	

The same procedures used for discovering protein peaks were processed for the samples in the validation set. Some of the differentially expressed peaks found in the test set remained significantly expressed in the validation set.

Table 19. Differentially expressed protein peaks in validation set

m/z value	Pilot study (n = 9)	OVCAD test samples (n = 78)	OVCAD validation samples (n = 62)
2888	significant	0.14	0.2
3360	significant	0.034	0.039
3445	significant	0.06	0.04
3487	significant	0.06	0.035
3645	significant	0.04	0.04

Further confirmation will be needed on the CM10 surfaces and is currently being analysed. The protein profiles of ovarian cancer tissue that can discriminate between platinum resistant and sensitive disease are expected.

Proteomic analysis of plasma samples

This task was allocated to partner 4, led by Jean-Paul Borg with the aim to identify circulating protein patterns that could predict therapeutic response to paltinum-based

chemotherapy. Pre-treatment plasma samples delivered from clinical partners, frozen and stored at -80°C. The proteomics analysis of 155 plasma samples was carried out and the results were evaluated based on part of the patients, for whom both clinical and proteomic data were available. Two technical approaches were performed using unfractionated whole plasma samples or samples equalized using proteominer technology.

Analysis of unfractionated plasma samples:

The plasma samples along with 8 replicates of plasma references have been analyzed using the following experimental design:

- 10 µl plasma were denatured by 20 min. incubation in 90 µl of urea-based buffer
- 10 µl of the mix urea buffer/plasma were then incubated in duplicate during 45 minutes with 4 types of ProteinChips arrays:
  - H50 (reverse phase . hydrophobic interaction)
  - Cooper-coated IMAC 30
  - CM10 (Cationic exchange surface).
  - NP20 (neutral surfaces)

This step was entirely automated using Tecan Evo system.
After washing and energy absorbing molecule (matrix. sinapinic acid) addition, chips were analyzed by SELDI-TOF MS using ProteinChip System Series 4000. After smoothing, noise filtering, and baseline subtracting, spectra were mass aligned and normalized using total ion current procedure. Then peak detection was performed using integrated ProteinChip Software. Raw peak data (including masses and intensities) were exported using excel file and then subjected to further biostatistic processing.

Overall, 725 protein peaks were detected within 2 optimized mass ranges:

- low molecular weight 1.500-30.000 Da = 551 protein peaks.
- high molecular weight 30.000-200.000 Da = 174 protein peaks.

The coefficient of variation (CV) of control plasma spotted as replicates was considered as acceptable (Average pooled CV = 36 % (23-49%)). Reproducibility of patient sample replicates was addressed by calculating correlation between each measurement: coefficient of correlation was 0.9423 and was also considered as acceptable. Experimental and clinical data were correlated. Supervised analyses were developed in order to identify protein peaks differentially expressed according to platinum sensitivity. In addition, a beads based sample equalization approach was applied and the same analytical processes were performed.

- Analysis 1 - to distinguish platinum resistant vs. non- platinum resistant patients: 135 patients were evaluable for analysis 1 (patients were evaluable if clinical and proteomic data were available and if they had at least 6 months of follow-up). 31 patients were resistant (23%) while 104 patients were not (77%). Learning (including 2/3 of patients, n=89) and testing (including 1/3 of patients, n=46) sets were built in a chronological and balanced (20% of resistant) way. In the learning phase, for each protein peak, comparisons of mean intensity in resistant (R) and nonresistant (NR) patients (Student T test) were performed, with a method of minimization of False Discovery Rate (FDR) (Dudoit Method). The following 17 peaks (with the corresponding chromatographic surfaces and m/z ratio) were retained:

Table 20. 17 protein peaks

1	NP20 91853
2	NP20 89240
3	H50 14108
4	H50 28249
5	H50 84767
6	H50 29233
7	H50 56331
8	IMAC 5241
9	CM10 175917
10	H50 94758
11	IMAC 10463
12	NP20 5002
13	CM10 47189
14	H50 130449
15	NP20 9348
16	H50 23789
17	NP20 51430

These 17 protein peaks discovered in learning test were used to build a multiparametric predictor allowing distinguishing between responders (R) and non-responders (NR) by a diagonal linear discriminant analysis (DLDA). Patients were classified as R and NR using DLDA-17 protein predictor. Proteomic based prediction was compared to the clinical defined phenotype (Table 21).

Table 21. Comparison of the classification of R and NR using multiprotein predictor and by clinical definition

Protein predictor/clinical definition	**Resistant**	**Non Resistant**
Resistant	**2**	**11**
Non resistant	**8**	**25**
P value	0.7	
Good prediction rate [IC95]	58.7 % [43.2-73]	
sensitivity [IC95]	69.4 % [51.9-83.7]	
specificity [IC95]	20 % [2.5-55.6]	
Youden index	-0.11	
Positive predictive value[IC95]	75.8 % [57.7-88.9]	
Negative predictive value [IC95]	15.4 % [1.9-45.4]	

As shown, the multiprotein predictor did not significantly predict platinum sensitivity, with a very low good prediction rate and a very low specificity. Positive predictive value (PPV) of the predictor was nearly similar to the clinical prevalence of the resistant/non resistant phenotype, indicating no supplementary clinical interest.

- Analysis 2: to predict time to event (progression or death): 136 patients were evaluable for analysis 2. Learning (including 2/3 of patients, n=90) and testing (including 1/3 of patients, n=46) sets were built in a balanced (same rate of events in each population) way. In the learning phase, CoxBoost method was used to build a multiprotein predictor composed of the following plasma protein peaks:

Table 22. Protein peaks for the multiprotein predictor

1	IMAC 4810
2	IMAC 6381
3	IMAC 8881
4	IMAC 8983
5	IMAC 23532

This predictor was able to identify two subsets of patients with significantly different progression-free survivals according to plasma expression of the above mentioned protein peaks (Figure 20).

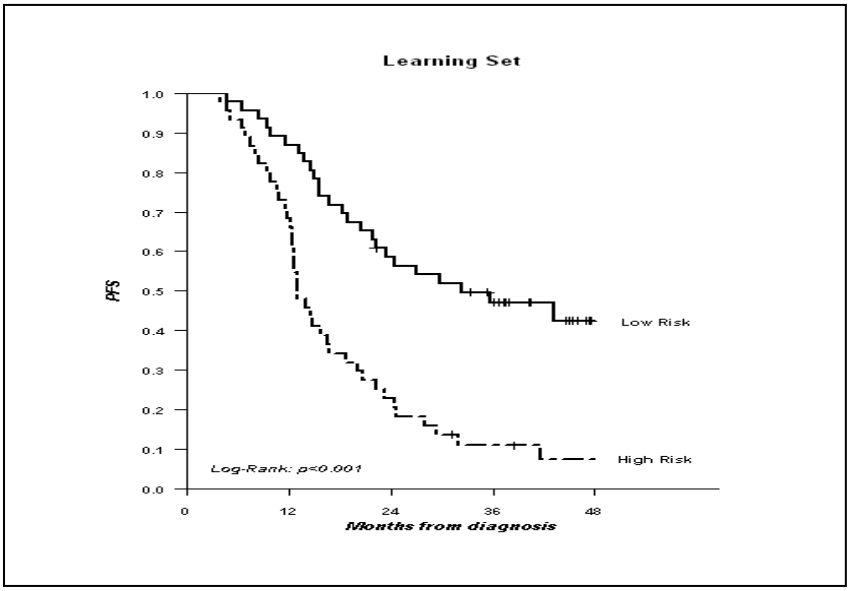

Figure 20. Progression-free survivals according to plasma expression of the protein peaks.

In the validation set, no significant difference in median PFS was observed between proteomic predicted "low-risk" patients compared to "high-risk" ones (p=0.106).

Analysis with bead-based sample equalization:

The 20 most abundant proteins in plasma represent 90-99% of total amount of protein. In addition, there is a very high dynamic range in serum/plasma, and amount of expressed proteins are in a wide range of concentrations, from fentogram- to gram per litre. This explains the high difficulties to detect at the same time proteins with so different concentrations, notably the low ability to detect very low-abundant proteins (the so-called deep proteome).

ProteoMiner technology (BioRad) provides a method for overcoming this challenge. It is based on a large, highly diverse library of hexapeptides bound to chromatographic supports. In theory, each unique hexapeptide binds to a unique protein sequence. Because the bead capacity limits binding capacity, high-abundance proteins quickly saturate their ligands and excess protein is washed out during the procedure. In contrast, low-abundance proteins are concentrated on their specific ligands, thereby decreasing the dynamic range of proteins in the sample.

200µl of the same 155 plasma samples as above were subjected to ProteoMiner technology, being incubated onto a specific 96-well plate. After washing, equalized proteins were eluted in 4 fractions. Eluted fractions (F1, F2, F3 and F4) from the 155 samples were then incubated with 3 types of ProteinChips: H50, Cooper-coated IMAC 30, CM10 according to the same settings as described in last periodic report.

Biological replicates were independently subjected to the whole procedure and showed good reproducibility (Figure 21).

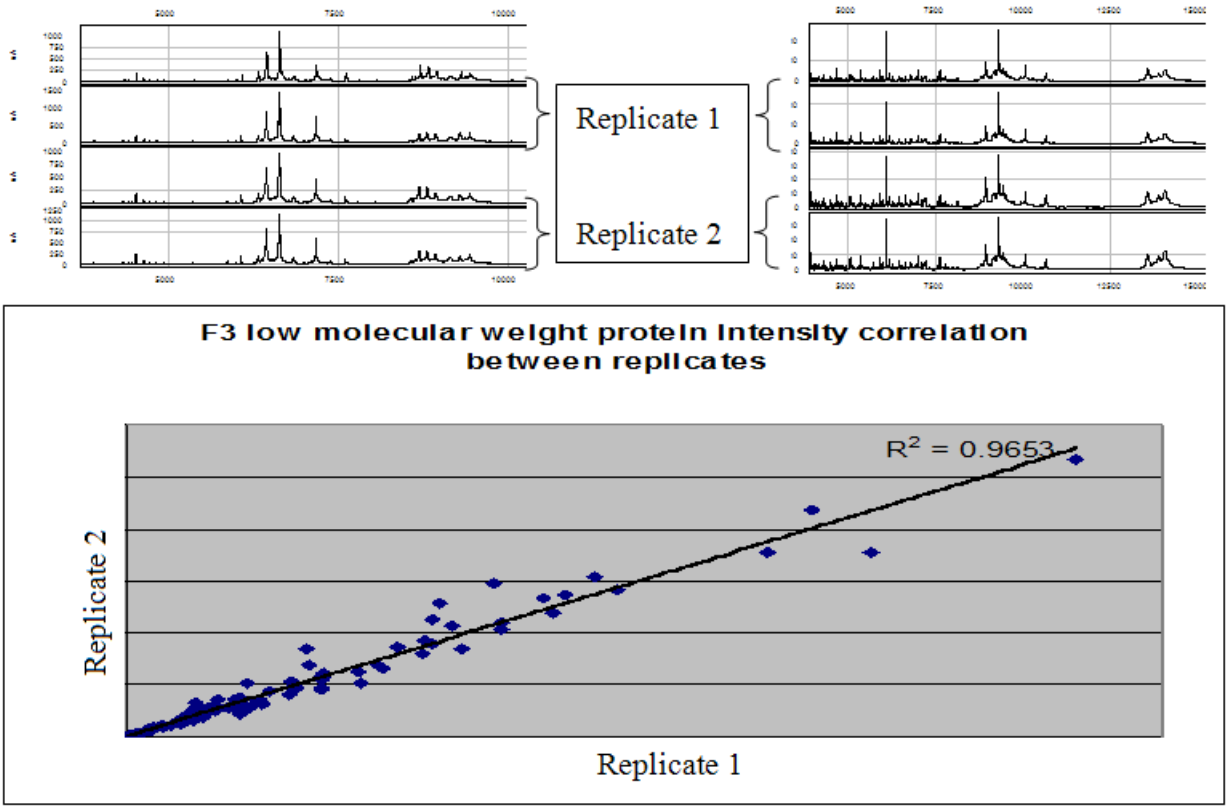

Figure 21. Reproducibility of biological replicates.

Overall, 2616 protein peaks were obtained within 2 optimized mass ranges:

- low molecular weight 1,500-30,000 Da = 1937 protein peaks,
- high molecular weight 30,000-200,000 Da = 679 protein peaks

Experimental data were correlated to clinical data and supervised analyses were developed in order to identify protein peaks differentially expressed according to platinum sensitivity.

Condition	peaks number	M/Z range
CM10-F1-LMW	150	1501 - 28207
CM10-F1-HMW	51	33793 - 279075
CM10-F2-LMW	138	1507 - 28873
CM10-F2-HMW	51	30160 - 283879
CM10-F3-LMW	147	1513 - 28956
CM10-F3-HMW	49	31405 - 277609
CM10-F4-LMW	156	1509 - 29048
CM10-F4-HMW	60	33422 - 277403
IMAC-F1-LMW	172	1500 - 28739
IMAC-F1-HMW	54	33392 - 281863
IMAC-F2-LMW	235	1506 - 29602
IMAC-F2-HMW	55	30044 - 277722
IMAC-F3-LMW	169	1510 - 29076
IMAC-F3-HMW	58	31413 - 276194
IMAC-F4-LMW	149	1506 - 29094
IMAC-F4-HMW	67	30173 - 276689
H50-F1-LMW	122	1510 - 28124
H50-F1-HMW	56	33462 - 267272
H50-F2-LMW	212	1506 - 29019
H50-F2-HMW	58	28154 - 273814
H50-F3-LMW	163	1507 - 29035
H50-F3-HMW	59	34623 - 279964
H50-F4-LMW	124	1500 - 29027
H50-F4-HMW	61	33227 - 268579

Figure 20. Protein peaks differentially expressed in platinum sensitive and resistant groups.

- Analysis 1 - to distinguish platinum resistant (relapse within 6 months) vs. non-platinum resistant patients: 136 patients were evaluable for analysis 1 (patients were evaluable if clinical and proteomic data were available and if they had at least 6 months of follow-up). 30 patients were resistant (22%) while 106 patients were not (78%). Learning (including 2/3 of patients, n=91) and testing (including 1/3 of patients, n=45) sets were built in a chronological and balanced (20% of Resistant) way. In the learning phase, for each protein peak, comparisons of mean intensity in resistant (R) and nonresistant (NR) patients (Student T test) were performed, with a method of minimization of False Discovery Rate (FDR) (Dudoit Method). The following 53 peaks (with the corresponding chromatographic surfaces and m/z ratio) were retained:

Table 23. 53 protein peaks.

1	8148-CM10-F2	19	3956-IMAC-F2	37	104737-H50-F3
2	2152-CM10-F2	20	7767-H50-F2	38	8809-H50-F4
3	3132-CM10-F2	21	2038-CM10-F1	39	8914-H50-F4
4	4111-CM10-F1	22	108109-IMAC-F4	40	8206-H50-F4
5	2141-CM10-F2	23	49724-CM10-F3	41	141011-H50-F3
6	76002-IMAC-F2	24	19947-IMAC-F1	42	8686-H50-F4
7	5290-IMAC-F1	25	6434-H50-F4	43	248165-H50-F3
8	3274-IMAC-F1	26	1512-H50-F4	44	90341-H50-F4
9	7618-IMAC-F3	27	9366-CM10-F1	45	6483-H50-F1
10	4411-IMAC-F1	28	43343-IMAC-F1	46	198205-H50-F3
11	5304-IMAC-F1	29	7619-H50-F3	47	9013-H50-F4
12	2514-CM10-F1	30	5526-CM10-F1	48	183153-H50-F3
13	17313-CM10-F2	31	2996-CM10-F1	49	4463-H50-F4
14	7987-IMAC-F2	32	97156-H50-F3	50	161503-H50-F2
15	7769-CM10-F2	33	155492-H50-F3	51	279964-H50-F3
16	8292-IMAC-F1	34	82144-H50-F4	52	95022-H50-F4
17	7638-CM10-F2	35	3292-IMAC-F1	53	171282-IMAC-F1
18	3141-IMAC-F1	36	172184-H50-F4		

In an independent validation set, this multiprotein model did not show any significant predictive value for the identification of platinum-sensitive patients.

Table 24. Prediction of outcome by multiprotein predictor

	Clinical outcome	
	Resistance	**Non-resistance**
Predicted Resistance	**2**	**12**
Predicted Non-resistance	**8**	**23**
p-value (Fisher's test)	NS	
Good prediction [IC95]	55.6 % [40-70.4]	
sensitivity[IC95]	65.7 % [47.8-80.9]	
specificity [IC95]	20 % [2.5-55.6]	
Youden index	-0.14	
PPV [IC95]	74.2 % [55.4-88.1]	
NPV [IC95]	14.3 % [1.8-42.8]	

- Analysis 2: to predict time to event (progression or death): 136 patients were evaluable for analysis 2. Learning (including 2/3 of patients, n=91) and testing (including 1/3 of patients, n=45) sets were built in a balanced (same rate of events in each population) way. In the learning phase, CoxBoost method was used to build a multiprotein predictor composed of the following plasma protein peaks:
  1 9366.CM10.F1.
  2 3347.IMAC.F2.
  3 110771.IMAC.F4.
  4 1716.H50.F2.
  5 8587.CM10.F4.

  This predictor was able to identify to subsets of patients with significantly different progression-free survivals according to plasma expression of the above mentioned protein peaks (Figure 23).

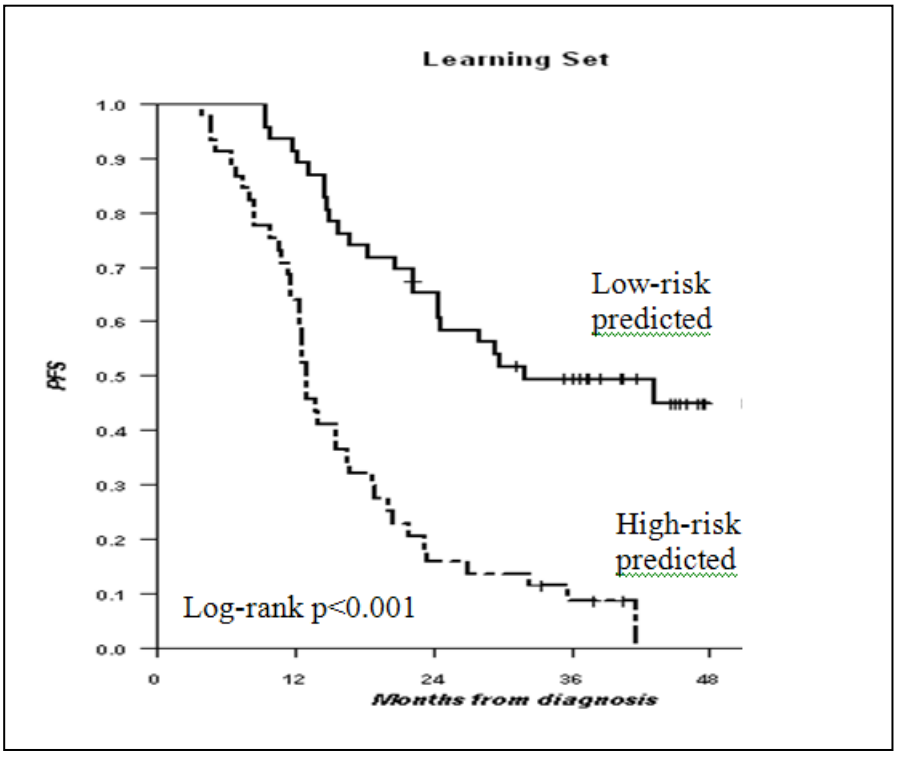

Figure 23. Survivals according to plasma expression of the protein peaks.

The 5-protein-predictor was validated the testing set using 45 independent plasma samples. Progression-free survivals were generated using Kaplan-Meier method and compared between proteomic-predicted subgroups using log-rank test (Figure24).

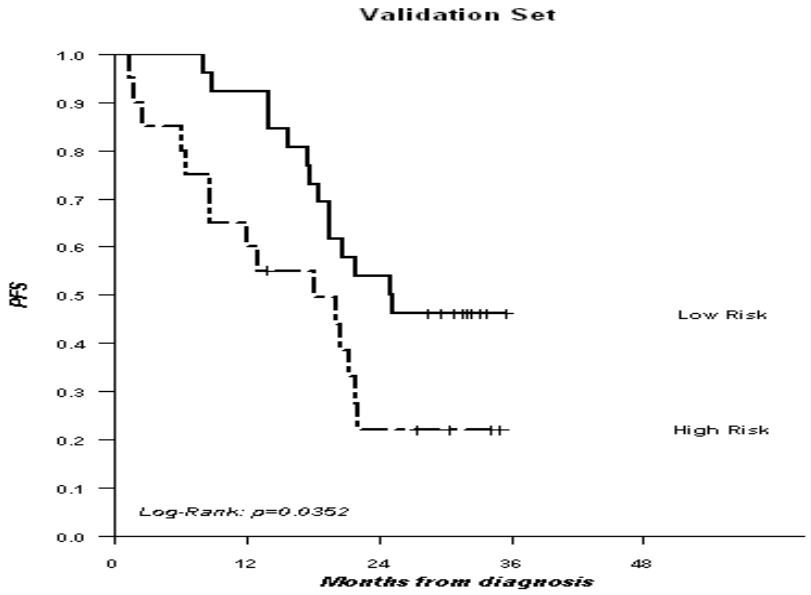

Figure 24. PFS of the high-risk and low-risk patients predicted with equalized plasma proteomic profiles.

It is validated that equalized plasma proteomic profiles predicted high-risk and low-risk patients with significantly different PFS.

- Analysis 3: Prediction of response status using plasma 5-protein-predictor: Plasma proteomic PFS-predictor was used to class patients according to platinum-response status. As shown below, this predictor significantly identified platinum-sensitivity status (Table 25).

Table 25. Prediction of reponse status using plasma 5-protein-predictor.

	Clinical phenotype	
	Resistant	**Non-resistant**
Proteomic-predicted High Risk	**8**	**12**
Proteomic-predicted Low Risk	**2**	**24**
p-value (Fisher's test)	0.01	
Good prediction [IC95]	69.6 % [54.2-82.3]	
sensitivity[IC95]	66.7 % [49-81.4]	
specificity [IC95]	80 % [44.4-97.5]	
Youden index	0.47	
PPV [IC95]	92.3 % [74.9-99.1]	
NPV [IC95]	40 % [19.1-63.9]	

Good prediction rate was almost 70%, specificity was 80% and positive predictive value was superior to 90%.

- Analysis 4: Comparison between plasma 5-protein-predictor and conventional clinical and pathological prognostic parameters: to compare the prognostic value of plasma 5-protein-predictor with other conventional clinical and pathological prognostic parameters, we built a multivariate Cox proportional hazard model.

Table 26. Comparison of the prediction using the plasma 5-protein-predictor and conventional parameters

N = 116		estimate	Hazard Ratio	HR IC95	p
Histology	no serous	-0.12	1	[0.457-1.723]	0.724
	serous		0.887		
FIGO	other	0.454	1	[0.738-3.363]	0.24
	IV		1.58		
Grade	G1-G2	0.588	1	[1.092-2.969]	**0.0211**
	G3		1.8		
Residual tumor	no	0.377	1	[0.929-2.289]	0.101
	yes		1.46		
SELDI risk group	Low risk	1.15	1	[1.956-5.093]	**<0.001**
	High risk		3.16		

As shown above, plasma 5-protein-predictor was the strongest independent prognostic parameter. Current identification of the relevant protein biomarkers is ongoing. If further validated, this profile could help stratifying patients for testing novel compounds or strategies in future clinical trials. In addition, depending on their biological relevance, the suggested biomarkers (yet to be actually identified) may become therapeutic targets.

Evaluation of candidate protein expressions for predicting patients' response

Various proteins were associated with tumorigenesis and progression of ovarian cancer. OVCAD had defined several tasks to measure the expression of several proteins in plasma, ascites and tumor tissues and to analyze the results in context of chemoresponse of ovarian cancer patients.

L1 expression in serum, ascites and primary tumors

Previously partner 5 led by Peter Altevogt and partner 6 led by Mina Fogel reported that soluble L1 can be detected in serum and ascites of ovarian carcinoma patients. L1 in body fluids is soluble and derived by ectodomain shedding of the transmembrane form. Using plasma and ascites samples from the OVCAD consortium, soluble L1 in these body fluids was determined. A total of 290 serum and ascites samples were analyzed in a sandwich ELISA specific for L1. Cell lysates prepared from tumor tissues by detergents lysis (1% Triton-X100) were also measured to determine total L1 content of the tumor sample (i.e. mostly membranous L1). Nearly all of these tumor tissue lysates (appr. 92%) were found to be positive for L1 (Table 27). Table 27 also summarizes the results from ELISA of ascites and plasma samples and groups them according to L1 status.

Table 27. Comparison of L1 in tumor lysates, plasma and ascites in OVCAD samples as determined by ELISA

	number of patients	L1 positive	L1 negative
tumor lysate	244	225	19
ascites	268	157	111
plasma	268	161	107

When the presence of L1 was correlated to survival data, several observations could be made. The presence of L1 in cell lysates was per se not a factor affecting patient survival (Figure 25A). In contrast, the presence of soluble L1 in ascites was a prognostic factor both for overall survival and progression free survival (Figure 25B, 25C).

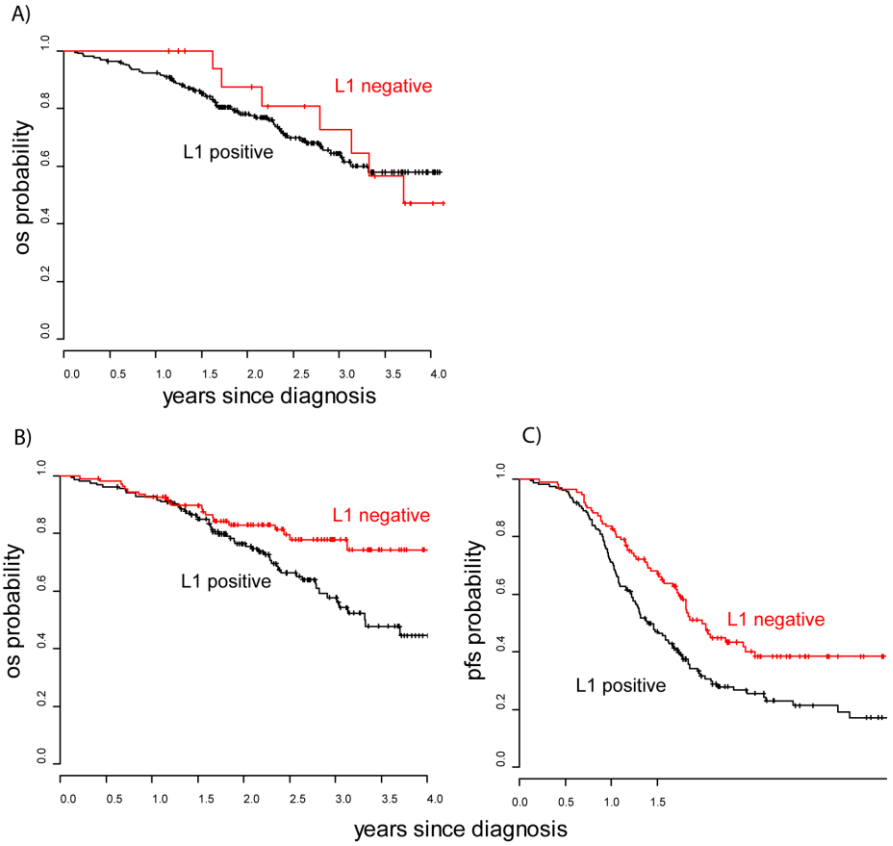

Figure 25. Kaplan-Meier survival analysis for overall or progression free survival in relation to L1 in tumor lysates (A) or ascites (B, C).

In multivariate analysis, taking age, FIGO stage and tumor grade into account, soluble L1 in ascites was a significant (p=0.0035) independent prognostic factor.

Partner 6 analyzed L1 expression by immunohistochemistry (IHC). L1 staining was observed in several patterns that differed between tumor samples. The following staining patterns were noticed and examples are given in Figure 26: L1 positive (40-50 % of cells positive), L1 focally positive (20-30% positive), advancing edge (10% cell positive mostly at the tumor-stroma interphase), L1 diffusely positive (80-90%).

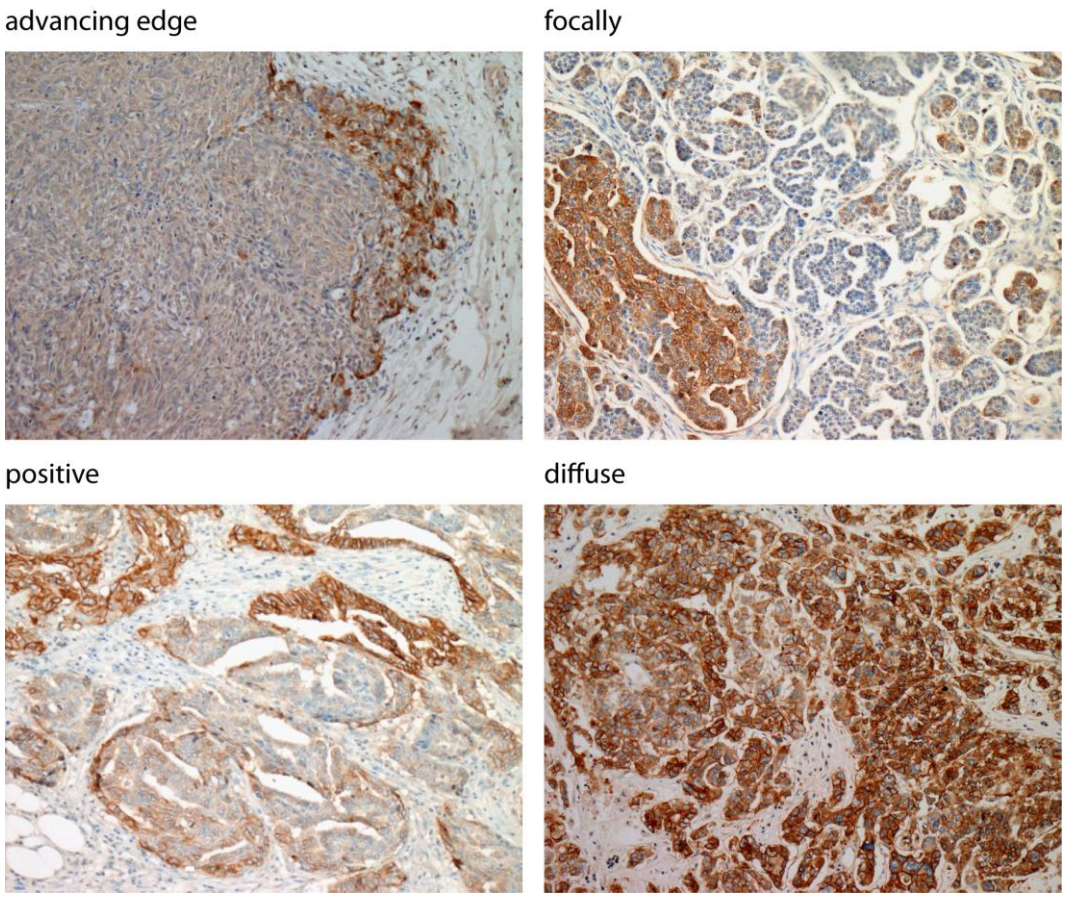

Figure 26. (A) Immunohistochemical staining of OVCAD tumor sections with mAb to L1 (mAb L1-14.10). Staining examples are given to illustrate the different L1 staining pattern.

Interestingly, the highest levels of soluble L1 in ascites were observed in the groups showing advancing edge or diffuse L1 staining (Figure 27A). When examined by Kaplan Meier analysis, the advancing edge and diffusely staining groups showed also worst overall and progression free survival (Figure 27B, 27C). These results suggested that L1 expression is most dangerous for ovarian carcinoma patients when it is cleaved by ectodomain shedding and soluble L1 is present. As soluble L1 was previously shown to trigger erk-activation, enhance cell motility and protect from apoptosis, these clinical data support an important role of soluble L1 in the progression of ovarian carcinoma.

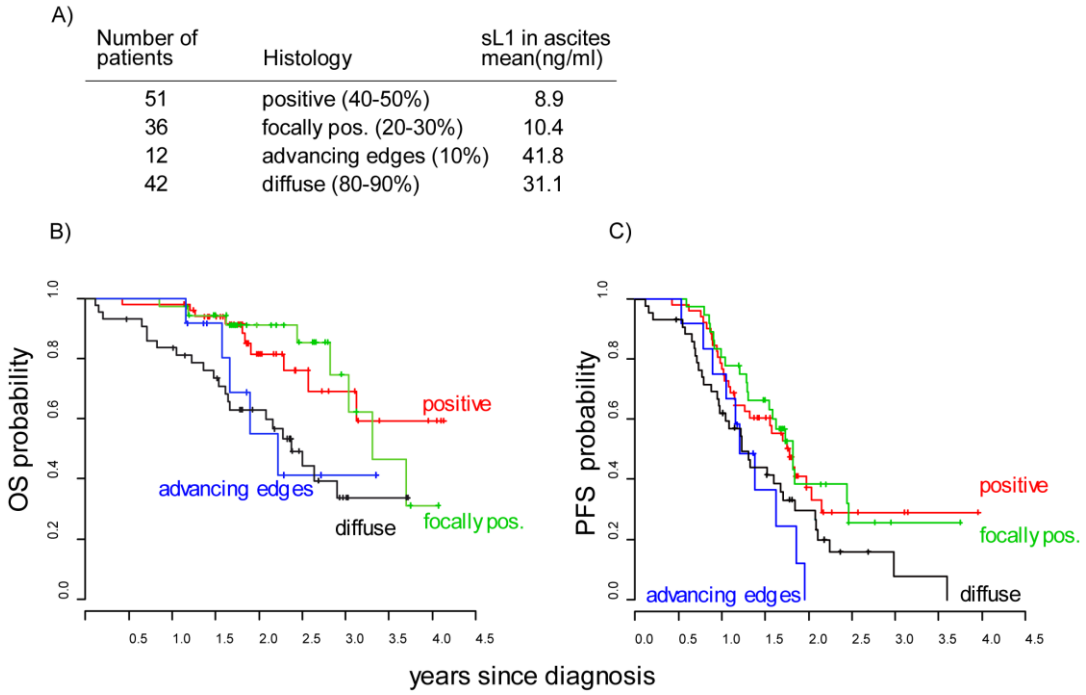

Figure 27. (A) Frequencies of L1 expression patterns in primary tumors (A) and Kaplan-Meier survival analysis for overall (OS) and progression free survival (PFS) in relation to L1 expression patterns in tumors (B, C).

HE4 expression and its influence on the surgical outcome in ovarian cancer patients

Originally, the tasks of partner 2 led by Jalid Sehouli were defined to evaluate VEGF, u-PA and PAI-1 expression and analyze their impact on predicting outcome. During the OVCAD project, P2 found an interesting marker HE4. HE4 gene is part of a family of protease inhibitors that function in protective immunity, and is expressed primarily in the reproductive tract and upper airways and can be detected in the plasma of patients' peripheral blood. This biomarker is over-expressed in ovarian carcinoma tissue, with minimal gene expression in normal tissue as also in several benign diseases. Due to these properties, HE4 was in the focus of some research groups trying to develop a new tumor marker or test for ovarian cancer screening and early diagnosis. HE4 gene is expressed particularly in serous and endometrioid ovarian cancer, but also in endometrial cancer or lung adenocarcinoma. The studies published until now showed that measurement of both HE4 and CA-125 together provides a better tool in identifying patients with ovarian cancer. Due to the innovation and the promising results of this marker, the original plan was changed and P2 decided to analyze the predictive value of HE4 in stead of other markers, which were well validated in the mean time.

The expression of HE4 in plasma and ascites from 276 patients with primary ovarian cancer were measured. Our results showed that the HE4 concentration in ascites was significant higher than that in plasma, having the mean values of and 8670 (range 104-149700) and 409 (range 29-900000), respectively. HE4 expression in plasma correlated significant with FIGO stage ($p<0.001$), being more expressed in advanced stage, with ascites volume ($p=0.002$), histological type ($p=0.002$), with residual mass after surgery and chemotherapy response ($p=0.012$). The patients having higher concentration of HE4 in plasma were more unlikely to benefit from cytoreductive

surgery and platinum based chemotherapy. HE4 concentrations in ascites didn't correlate with any clinical prognostic factor. Only in the univariate analysis HE4 expression in plasma was able to predict the surgical outcome and chemotherapy response, this significance was lost in the multivariate setting.

Plasma concentrations of the Vitamin E binding plasma protein Afamin in ovarian cancer patients

Comparative proteomics identified the vitamin E binding plasma protein afamin as potential novel tumor marker for ovarian cancer (OC). Partner 15 was led by Hans Dieplinger further validated afamin plasma concentrations in a small pilot and a large case/control study. Afamin was significantly decreased in preoperative OC patients compared to controls and increased to normal control values after successful tumor removal. The aim in OVCAD was to evaluate and to specify the diagnostic utility of afamin in OC patients and to elucidate possible mechanisms for decreased afamin levels in OC.

P15 measured afamin by specific sandwich-type ELISA in plasma samples and ascites from a total of 230 OC patients. From 107 OC patients blood withdrawn 6 months after primary treatment were also available. Patients were subdivided in responding and non-responding to chemotherapy. To investigate a possibly increased consumption of afamin by OC tissue that could explain the diminished plasma levels in OC patients, afamin uptake in HTP77 cells was studied in an established OC cell line by immunoblotting and immunocytochemistry.

As in previous studies, afamin plasma concentrations were significantly reduced in OC patients. They correlated significantly with afamin concentrations in the respective ascites fluids ($n=230$, $r_s=0.203$; $p=0.004$). An increase to values of healthy controls was, however, only observed in patients responding to chemotherapy ($p<0.001$), whereas afamin values in non-responders did not change significantly ($p=0.202$). OC tissue showed massive immunohistochemical reactions with antibodies against human afamin. Cell culture studies in HTP77 cells with exogenously added recombinant human afamin showed substantial uptake of afamin as demonstrated by immunoblotting and immunohistochemistry.

In summary, these data clearly indicate an additional role of afamin in predicting response to thearapy. They furthermore point towards an increased consumption of afamin as response-to-disease mechanism to explain the decreased afamin levels in OC.

<u>Evaluation of epitope profiling of ovarian cancer associated proteins</u>

The overall goals in regarding the epitope profiling of ovarian cancer were analysis of general properties of cancer antoantigen profiles, with particular focus on potential targets for immunodiagnostics and immunotherapy for ovarian cancer. Tasks include methods development (interaction network analysis) for deciphering general properties of autoantigen profiles in cancer, development of a novel experimental screening technology (immunome peptide chips), and finally target identification and experimental verification on the basis of public domain ovarian cancer 'omics' data. The task was carried out by partner 12, led by Bernd Meyer.

Data sets selection and differential gene expression

Following preparatory work for OVCAD, we have extracted public domain differential gene expression data showing significant differences when comparing tumor and healthy tissue. On the basis of this meta-analysis we identified about 1900 features, of which 192 showed increased prevalence of differential expression. This data repository provides a first core list for studying the interrelation of differential gene expression and autoantigen profiles.

Data set SEREX

The Ludwig Cancer Institute organizes a public domain database for autoantigens derived on the basis of SEREX. We have extracted the entire database and completed annotation of all features provided. In total autoantigen profiles for about 30 tumors are listed, giving 80 autoantigen candidates for ovarian cancer. This data set is, next to the differential gene expression data, the second repository for our analysis procedures.

Programming and interaction graphs

A first methods development step focuses on protein interaction network analysis. Hypothesis driving this project step is that cancer autoantigen networks are i) non-random, and ii) show similarities when compared between different cancer types. We have chosen the level of protein interactions for checking this hypothesis. Graph measures implemented are given in the following Table 28.

Table 28. Formal representation of graph measures

Name	Description		Ref.
size measures			
Closeness Centrality	$CC_i = \frac{1}{\sum_j d(i,j)}$	d(i,j) is the length of the shortest path between vertex i and j. The sum of CCi over all vertices gives the total closeness centrality of a given sub-graph.	[36]
Graph Diameter	$GD = \frac{\max(d(i,j))}{N}$	d(i,j) is the length of the shortest path between vertex i and j. GD is computed for all pairs (i,j), the graph diameter is reflected by the longest path identified.	[37]
Index of Aggregation	$IoA = \frac{A}{B}$	A is the total number of vertices in the sub-graph, and B is the total number of all given vertices of the graph.	[13]
distribution measures			
Assortative Mixing Coefficient	$r = \frac{4^* < k_1 * k_2 > - < k_1 + k_2 >}{2^* < k_1^2 + k_2^2 > - < k_1 + k_2 >^2}$	k1 and k2 are the counts of edges of two vertices connected by a given edge. This measure reflects the edge-edge distribution over all edges of a graph.	[38]
Entropy of the distribution of edges	$H = -\sum_k p(k) \ln p(k)$	k is the count of edges of one vertex, and p(k) is the ratio of vertices which have k edges.	[39]
relevance measures			

Betweenness	$B = \frac{\sum_{i \in V} \sum_{j,k} \frac{\sigma(j,i,k)}{\sigma(j,k)}}{N}$	σ(j,i,k) is the total number of shortest connections between vertex j and k, where each shortest connection has to pass vertex i, and σ(j,k) is the total number of shortest connections between j and k. We computed σ(j,i,k) and σ(j,k) for the entire OPHID graph, but then only used vertices also present in the sub-graph generated on the basis of a given gene expression data set.	[36]
Betweenness of all selected vertices	As for Betweenness, but all selected vertices are considered.		[36]
Stress Centrality	$StC = \sum_{i \in V} \sum_{j,k} \sigma(j,i,k)$	σ(j,i,k) is the total number of shortest connections between vertex j and k, where each shortest connection has to pass vertex i.	[36]
density measures			
Connectivity	$C = \frac{A}{B}$	A is the total number of edges realized in a given graph, and B is the maximum number of edges possible.	[37]
Clustering Coefficient	$CLUST_i = \frac{A}{B}$	A is the total number of edges between the direct neighbors of vertex i, and B is the maximum number of possible edges between the direct neighbors of vertex i. The sum of CLUSTi over all vertices gives the total Clustering Coefficient of a given sub-graph.	[40]
Number of edges divided by the number of vertices	$NeNv = \frac{A}{B}$	A is the total number of edges in a given graph, and B is the number of selected vertices in a given graph.	-
Community	$Comm = \frac{A}{B}$	A is the total number of edges, where both connected vertices are in the given sub-graph, and B is the total number of edges, where one connected vertex is in the sub-graph and the other vertex is outside.	[41]
Entropy	$H(G) = \sum_{v \in V, i(v)>=2} (i(v)-1) * \log(\frac{\lvert E \rvert - \lvert V \rvert + 1}{i(v)-1})$ |E| gives the total number of edges, |V| gives the total number of vertices; $i(v)$ gives the number of edges of vertex v.		[42]
Graph Centrality	$GC_i = \frac{1}{\max(d(i,j))}$	max(d(i,j)) is the length of the shortest path between vertex i and j for a given vertex i.	[36]
Number of Walks of length (n)	$NW = \sum NW_i$	NWi is one walk with length of n edges in the sub-graph.	[37]
Sum of the Wiener Number	$W_i = \frac{1}{2} * \sum_{i,j} d(i,j)$	d(i,j) is the length of the shortest path between vertex i and j. We computed a sum of the Wiener Number for each vertex.	[37]
modularity measures			

The total number of triangles of a sub-graph and its dilation	Given a sub-graph g of a graph G, the complement of g, denoted as g is the sub-graph implied by the set of vertices $N(\bar{g}) = N(G) \setminus N(g)$ The dilation of g is the sub-graph δ(g) implied by the vertices in g plus the vertices directly connected to a vertex in g. The coat of direct neighbors of the sub-graph is defined as: $DN(g) = \delta(g) \setminus N(g)$ The set of all valid triangles for g is defined as: $VT(g) = \{ x, y, z \mid (x,y,z \in N(\delta(g)) \wedge (x,y),(y,z),(z,x) \in E(\delta(g))) \cap (x \in N(g) \wedge z \in DN(g)) \}$ where N is the number of vertices, and E is the number of edges of the graph. The result for a sub-graph g is the total number of elements in VT(g).		[36]
Localized Modularity	$LM = \frac{\lvert E_{inside} \rvert}{\lvert E_{within\ the\ (direct)\ neighbors} \rvert} * \frac{\lvert E_{inside} \rvert * \lvert E_{to\ the\ outside} \rvert}{\lvert E_{within\ the\ (direct)\ neighbors} \rvert^2}$ $\lvert E \rvert$ gives the total number of edges.		[43]
modified Vertex Distance Number	$mVD = \sum_{i,j \in V, i \neq j}^{V} \frac{1}{d(i,j)^2}$	d(i,j) is the length of the shortest path between vertex i and j. For this measure, i and j are all selected vertices V.	-
cycles			
Eigenvalues	$EV = \sum_{j} \lvert ER_j \rvert^2$	ERj is the real part of the j-th Eigenvalue for the adjacency matrix of the given sub-graph.	[44]
Subgraph Centrality	$SC = \frac{1}{N} \sum_{i=1}^{N} \sum_{k=1}^{\infty} \frac{(A^k)ii}{k!}$	A is the adjacency matrix. We computed SC for k [1,99].	[36]
Cyclic Coefficient	$\theta(i) = \frac{2}{k_i * (k_i - 1)} * \sum_{j,k} \frac{1}{S_i(j,k)}$ $\theta = 1/N * \theta(i)$	Si is the smallest possible cycle of the vertex i and two of its neighbor vertices k. The total Cyclic Coefficient is then given for all vertices N as θ.	[36]

* Name, formal representation and short description of graph measures computed for the categories size, distribution, relevance, density, modularity and cycles.

Establishing immunome chip technology

Second methods development focuses on a novel, high throughput screening technology for identification of autoantigen profiles. Standard techniques for such a task include display methods as SEREX. Our prediction routines on antigenic determinants allows for the rational design of peptide chips, which in the meantime allow integration of up to 30.000 sequences on a single slide. All handling routines for this technology follow the setup used for differential gene expression analysis, providing easy to use and established infrastructure for performing this task. We have started on establishing this technology for screening ovarian cancer sera with a peptide chip prototype, a typical readout is given in the following Figure 28:

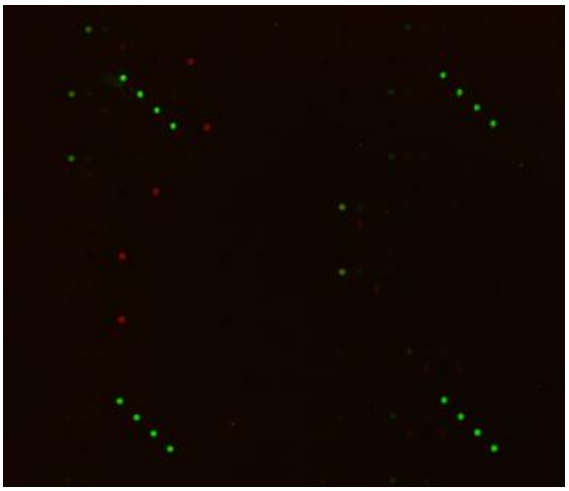

Figure 28. The figure shows a section of the immunome chip utilizing an ovarian cancer sera pool. The green spots represent controls, red spots show reactivity of antibodies present in the sera pool.

Data analysis, joint autoantigen networks

We have constructed protein interaction networks utilizing interaction data from the OPHID database, constructing undirected graphs for the given SEREX feature lists. The resulting graphs were then subjected to analysis including properties as size, density, betweeness, cycles, Eigenvalues, etc. In total, 22 different graph measures were implemented and tested on the given data sets. For deciphering our hypothesis random interaction networks were generated, and the deviation of given SEREX graphs from random graphs was checked. The following Figure 29 shows a typical evaluation result:

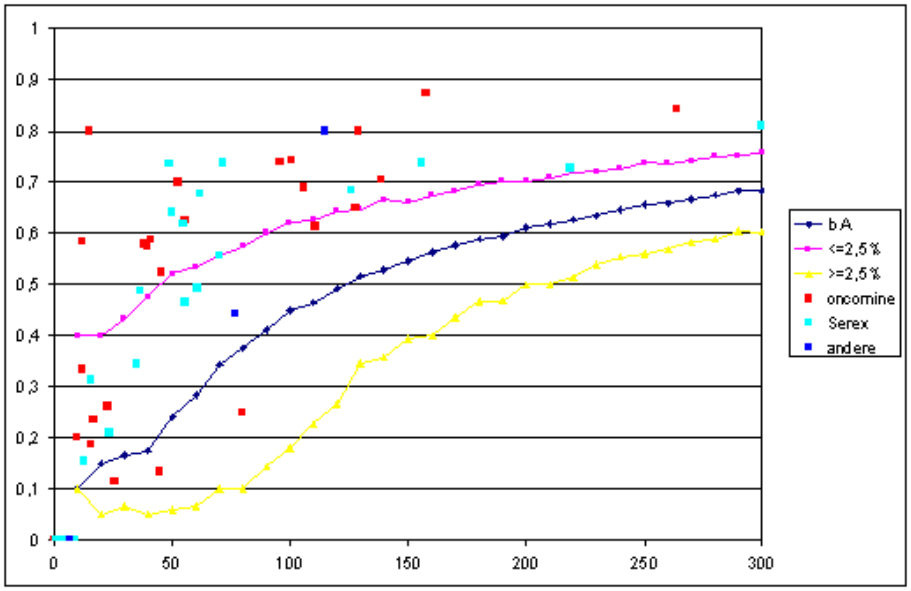

Figure 29 The figure provides mean values and 95% confidence intervals for the Index of Aggregation (IoA) of graphs derived on the basis of randomly selected feature lists, and additionally provides the IoA for SEREX (light blue).

Following the presently given interpretation of the interaction graph properties indicates that autoantigen profiles are non-random.

Paper draft, ovarian cancer immunome

Based on non-OVCAD project work, as well as following results provided within OVCAD, a concerted analysis for the link between differential gene expression and autoantigenic propensity was conducted. This work integrates diverse bioinformatics, covering gene expression analysis, co-regulation analysis on the level of joint transcription factors, further complemented by protein interaction network, sub-cellular location, and SEREX data analysis.

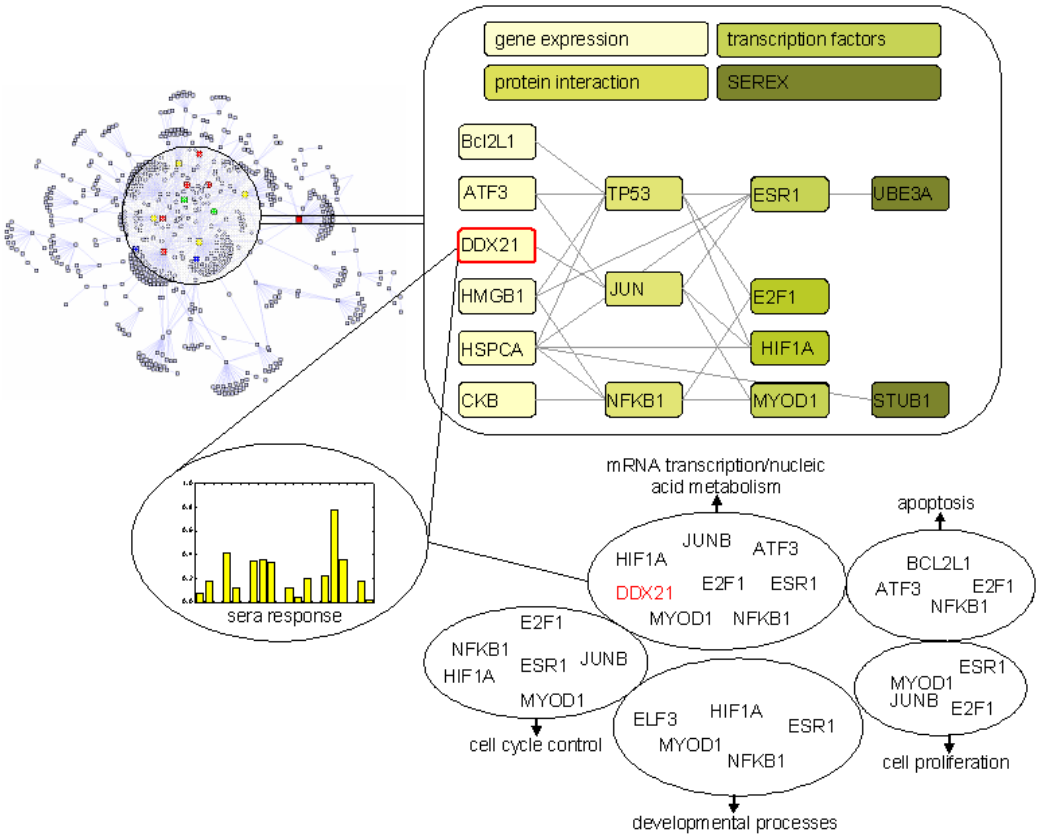

Figure 30. an impression on the interwoven network between transcription and autoantigenicity

This type of analysis will be continued on the basis of data provided by the immunome chip technology, but will in particular also include data from genomics and proteomics as provided by partner groups within OVCAD.

Further more, P12 refined an experimental epitope screening platform including proper statistical results evaluation. A total of 1000 epitopes have been screened with about 40 sera from ovarian cancer patients. Ashort list of epitopes has been derived which resembles the deliverable 17 (Ovarian Cancer Autoantigens).

Immunome chip screening

ELISA presents the state-of-the-art technique for screening (auto-)antibodies in human sera. We previously used this approach to examine the autoantigenic potential of proteins or peptides thereof, respectively. In order to analyze and identify new autoantigens of ovarian cancer for subsequently deriving autoantigenic profiles, we

used high-density peptide arrays/chips. In doing so we were able to screen for autoantibody targets simultaneously in a high-throughput manner.

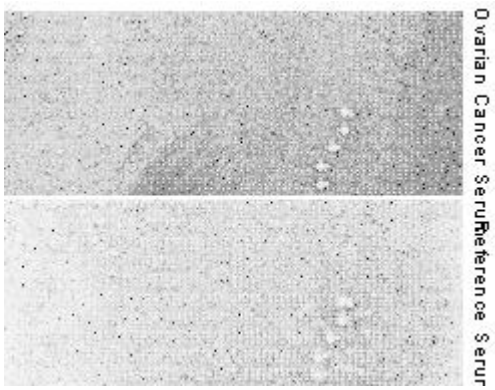

Figure 31: Visualization (of a section) of our Immunome screening chips utilizing sera from ovarian cancer patients (top) and reference sera from healthy individuals (bottom). Dark spots indicate antibody reactivity.

Using the resulting autoantibody signature for clustering reference and tumor sera indeed provides cancer-associated autoantigenicity profiles:

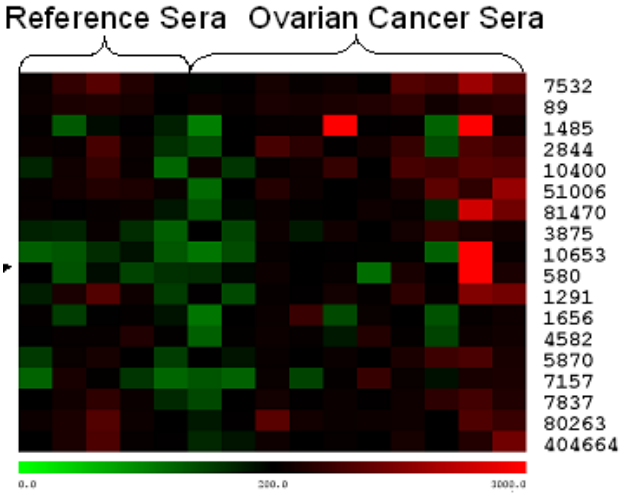

Figure 32: Heat-map-representation of the Immunome screening chip results along with identified peptides/proteins showing superior reactivity in tumor sera when compared to reference sera. Red squares indicate strong reactivity while green/black indicates no/weak reactivity.

Among the 18 candidate epitopes identified in the first set, some autoantigenic "usual suspects" were found, as e.g. BRCA1 associated RING domain 1 (BARD1), Cancer Testis Antigen NY-ESO I (CTAG1B), Keratin 18 (KRT18), Mucin 1 (MUC1) and the tumor protein 53 (TP53). These results illustrate the validity of the screening approach. Besides the aforementioned autoantigens a series of novel autoantigens has been found which will enter the next validation step.

Next to the 500 epitopes leading to the candidate epitope set given in Figure 31, a second peptide array was derived holding again 500 sequences. However, this second set was not selected solely based on differential gene expression in the tumor situation, but resembled 'early stage' antigen candidates (where NY-ESO is a prominent representative).

This second chip set was again tested with sera from healthy individuals and from ovarian cancer patients. Typical results of this screening round are given in Figure 33.

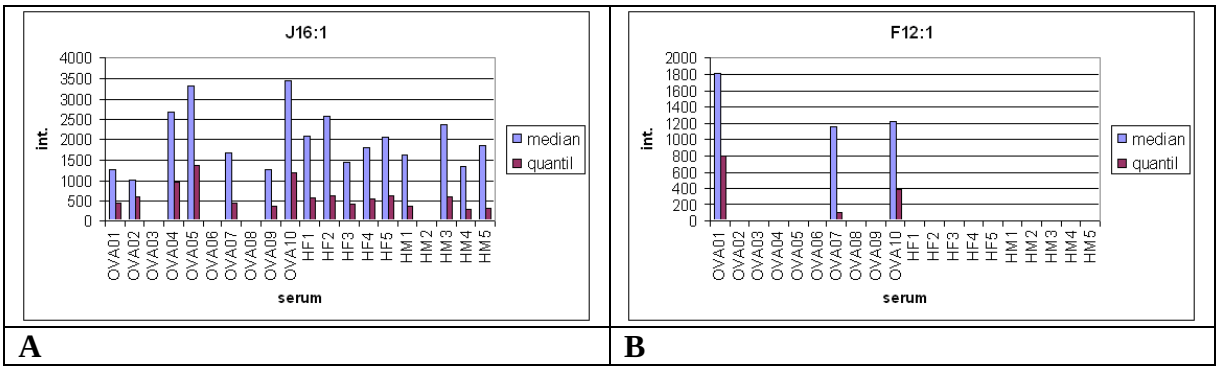

Figure 33: Candidate epitopes from the second chip set tested for their reactivity with plasma from ovarian cancer patients (OVCAD) and healthy female reference plasma (HF).

A considerable number of sequences showed no reactivity (as also given for the first epitope selection). A number of sequences showed overall high reactivity independent of the plasma type (Figure 32). However, a number of sequences showed reactivity with OVCAD sera but no background with healthy reference plasma.

Selection and validation of a subset of about 1000 epitopes

Based on the chip and ELISA pool data we selected 37 candidates for further analysis. Each candidate epitope was tested in an ELISA setup using 8 pools of ovarian cancer plasma composed of 10 individual plasma each. Based on these data a set of 10 epitopes was selected for testing the reactivity of individual sera.

A B

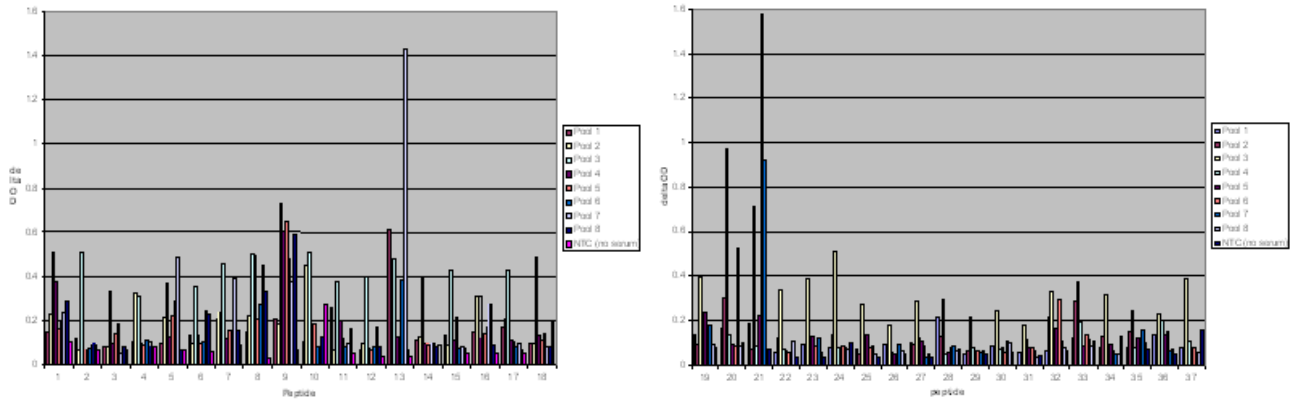

Figure 34. A: Set I of candidates: Provided is the epitope number, plotted against the ELISA OD obtained by screening sera pools. B: Set II of candidates: Provided is the epitope number, plotted against the ELISA OD obtained by screening sera pools.

Reactivity of candidate epitopes on the level of 81 single plasma is given as follows:

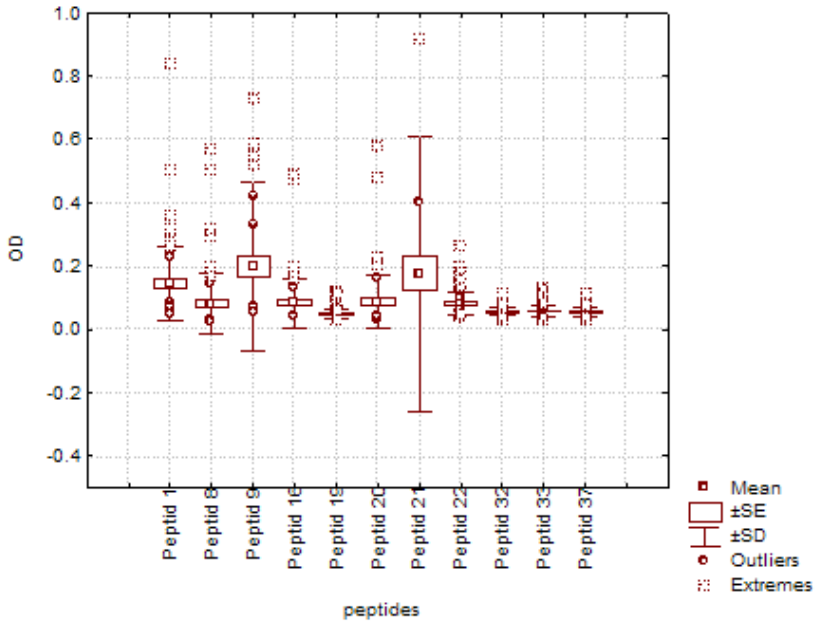

Figure 35: Mean value and distribution parameters characterizing the reactivity (given as OD) of the candidate epitopes and a negative reference (Peptid37).

Starting out from a list of differentially expressed genes reported in ovarian cancer, intersecting this list with SEREX reports on ovarian cancer autoantigens, and selecting candidate epitopes utilizing an in-silico selection procedure, we experimentally tested about 1000 candidate epitopes. From this broad screening we concluded on 37 candidate epitopes tested via sera pools, and finally tested 10 candidate epitopes on the level of 81 single plasma as provided by the OVCAD sample collection.
The clinical data characterizing the samples are given as:

- Total number of patient sera included in experiment: 81
- Total number of patient sera analyzed (complete data. serous only): 65
- Number of recurrences: 20
- Average days to recurrence: 460
- Number of deaths: 14
- Average number of days to death: 230
- Serous histology only
- Figo Stage II: 2
- Figo Stage III: 56
- Figo Stage IV: 7
- Complete surgical removal: 37
- Remaining tumor after surgery: 28

The majority of samples were from Stage III tumors. For statistical analysis we included serous tumors only (65), of which 20 showed recurrence. As given in Figure 36, seven out of the ten candidates showed reactivity at least with a number of plasma. In particular the peptides 9 and 21 gave in the mean significant reactivity. However, it is evident that single epitopes do not provide reactivity with a significant number of different sera. Certain sera provide high reactivity, whereas others show no reactivity at all. These findings are in line with literature reports on other autoantigens in ovarian cancer. e.g. anti-S100A7 antibody titers are reported as significantly elevated in ovarian cancer but still showing a high false-positive / false-negative number. Comparable findings are given e.g. for BARD1 showing SE=41% and SP=84%. The combination of BARD1, TM4SF1, ILF3, FXR1, TIZ, C1D, PKHD1 reaches SE=66%. SP=73%. Combining BARD1 with CA-125 yields SE=71% and SP=89%.

We also tested the association of autoantibody titers and recurrence; however, no correlation could be identified. A literature search also provided only one example where such a correlation was reported (Chance of serum antithyroglobulin antibody levels is useful for the prediction of recurrence in thyroid carcinoma. Kim et al., J. Clin. Endocrinol. Metab. 93. 4683-4689. 2008)

Our conclusion when reflecting literature data and our results are:

- The signature of autoantigens/autoantibodies is patient specific, as until now also given for transcriptomics and proteomics profiles
- Only the combination of autoantigens in a profile approach may provide clinically useful SE and SP values.

This conclusion is supported by Figure 37. Single plasma show reactivity with none/one/many of the provided candidate epitopes, whereas a combination provides good overall reactivity.

Samples	Peptid 1	Peptid 8	Peptid 9	Peptid 16	Peptid 19	Peptid 20	Peptid 21	Peptid 22	Peptid 32	Peptid 33	Peptid 37
B100	0.846	0.064	0.589	0.069	0.067	0.074	0.083	0.071	0.074	0.089	0.098
L092	0.119	0.508	0.063	0.199	0.046	0.228	0.920	0.065	0.048	0.044	0.075
H048	0.160	0.320	1.020	0.128	0.048	0.114	0.052	0.072	0.055	0.054	0.053
L053	0.508	0.143	0.137	0.492	0.119	0.581	1.506	0.093	0.118	0.131	0.114
B102	0.112	0.043	0.318	0.050	0.120	0.057	0.051	0.077	0.040	0.045	0.040
B061	0.238	0.048	0.080	0.474	0.049	0.480	0.061	0.081	0.052	0.059	0.057
H038	0.063	0.037	0.167	0.050	0.044	0.053	2.846	0.068	0.057	0.071	0.055
B080	0.244	0.055	0.097	0.067	0.053	0.068	0.068	0.196	0.060	0.068	0.078
L078	0.068	0.044	0.055	0.048	0.040	0.039	0.057	0.068	0.079	0.053	0.049
L085	0.360	0.044	0.523	0.050	0.042	0.045	0.048	0.069	0.055	0.120	0.050
H044	0.076	0.035	0.057	0.038	0.033	0.036	0.036	0.056	0.036	0.035	0.033

Figure 36: Combined profile reactivity given in red and blue (OD values) for selected sera (given in yellow).

(5) Approaches of circulating tumor cells (CTCs)

One potential approach for the development of predictive markers for ovarian cancer therapy could be the isolation and characterization of disseminated tumor cells from peripheral blood of patients with ovarian cancer. The detection and characterization of OC CTCs obtained from the peripheral blood of ovarian cancer patients could help to identify the patients who did not benefit from chemotherapy and moreover, to discover biomarkers for the decision in new therapy approaches if the standard therapy fails. The detection of CTCs makes an early diagnosis of recurrent disease possible and improves the understanding of the mechanism of lethal ovarian cancer cell spread. Partner 16 led by Burkhard Brandt aimed at isolating and characterizing CTCs in OC.

Detection of CTCs using genomic and protein markers

Detection of CTCs using original protocols

Detection of CTCs in blood cell fractions

According to the standard protocol, 199 blood samples (fixed monocyte fraction after density gradient centrifugation) were analyzed via EpCAM based semi-automated immunomagnetic cell separation and cytokeratin immunocytochemical staining. At the time point of the primary surgery (time Q), 143 samples were taken and other 56 samples were taken 6 month after completion of chemotherapy (time H). In 3.5%

(5/143) blood samples of time point Q, CTCs were detected. Additionally, a cell cluster was detected in one sample. None of the 56 H samples had detectable CTCs (Table 29).

Table 29: Detection rate of CTCs with the original protocol

time point	protocol	analyzed samples	samples with OCDCs	samples without OCDCs
before surgery (Q)	original protocol	143	5 (3.5%)	138 (96.5%)
6 month after therapy (H)	original protocol	56	0 (0 %)	56 (100%)

Detection of ambiguous cells

In some samples ambiguous cells were also found (Figure 37, 38). Some of these cells are positive for cytokeratin and additionally weekly positive for CD45. Other cells of this group are negative for CD45 and only weekly positive or negative for cytokeratin. These cells could derive from the primary tumor and might play a role cancer progression. They could have lost their cytokeratin expression. So, there is a need for further immunocytochemical characterization of these cells.

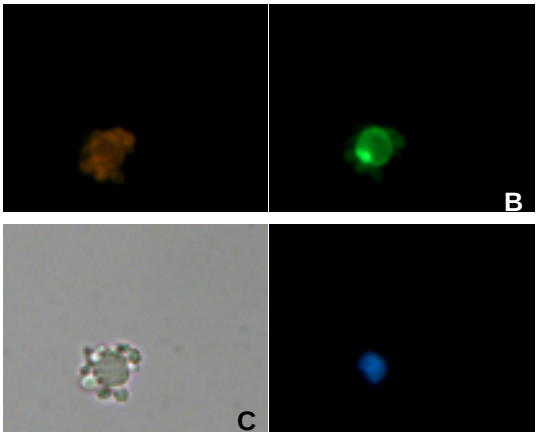

Figure 37: Ambiguous cell detected in blood of an ovarian cancer patient. A: cytokeratin staining (Cy3-channel); B: CD45 staining (Alexa488-channel); C: bright field; D: DNA staining by DAPI.

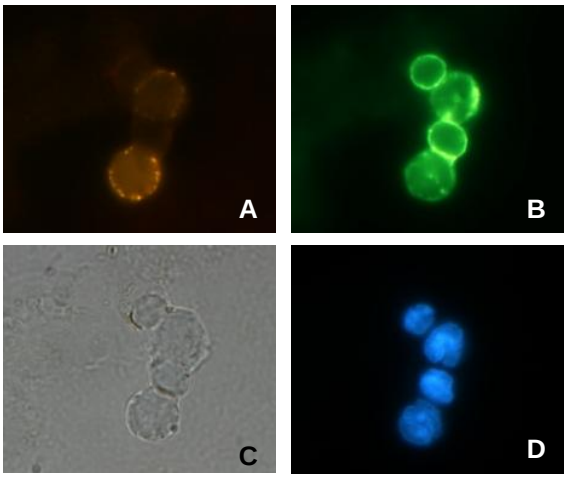

Figure 38: Ambiguous cells cell detected in blood of an ovarian cancer patient. A: cytokeratin staining (Cy3-channel); B: CD45 staining (Alexa488-channel); C: bright field; D: DNA staining by DAPI.

Immunocytochemical characterization of ascites cells

Because tumor cells of the ascites fluid could be precursor cells for disseminated tumor cells, these cells are very interesting to analyze. The immunocytochemical characterization of these cells might give us some hints about the quality of the enrichment and detection markers of CTCs. Additionally with the characterization of these cells, other potential tumor markers might be discovered. Therefore, cells isolated of the ascites fluid were stained for EpCAM and cytokeratin. Furthermore, staining of EMA (epithelial membrane antigen) was performed. The results demonstrated that the different markers are not expressed homogeneously for all ascites cells (Figure 39, 40). The results shows that primary ascites cells are more often positive for EpCAM than for cytokeratin and cultured ascites cells often lost the EpCAM expression and are often positive for cytokeratin (Figure 40). These results indicate a need for additional or new tumor markers for our detection method.

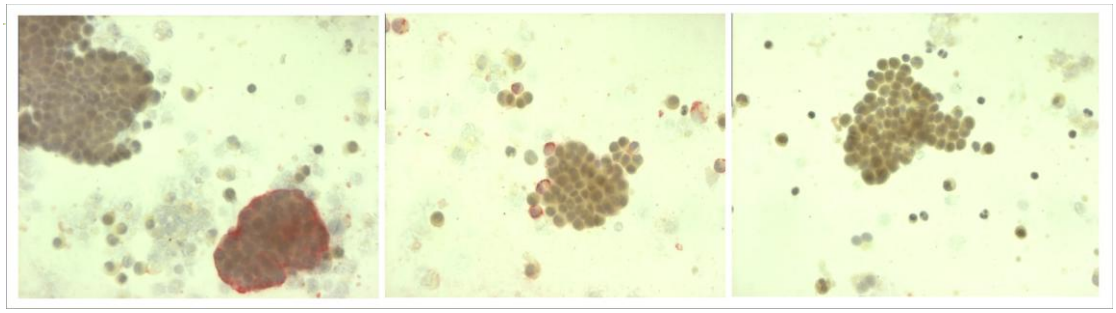

A) EpCAM B) cytokeratin C) EMA

Figure 39: Immunocytochemical staining of ascites cells of different tumor markers. A: EpCAM staining: one cell cluster is positive; one cell cluster is negative for EpCAM; B: cytokeratin staining: several cells of a cell cluster are positive the other cells are negative for cytokeratin; C: EMA staining: all cell clusters are negative for EMA, only a very rare number of cells are positive for EMA.

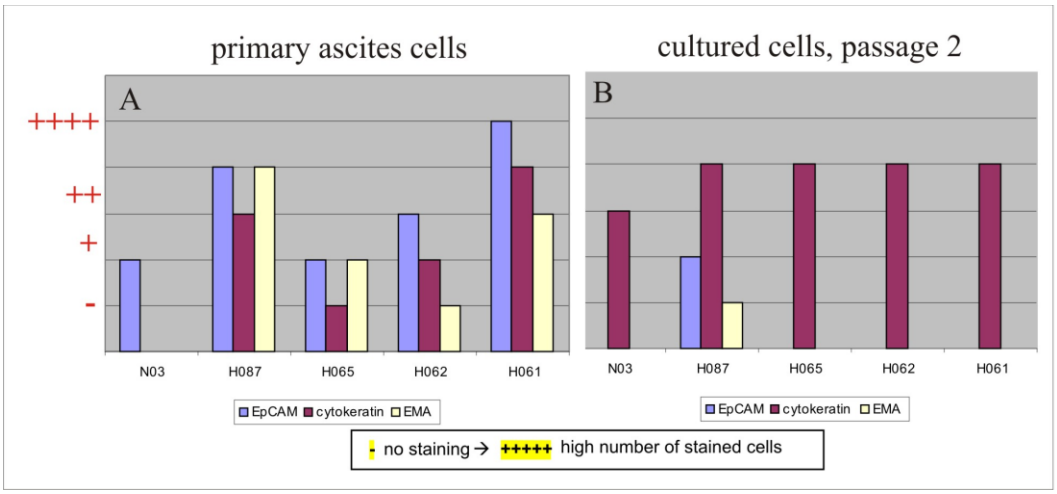

Figure 40: The Quantity of ascites cells of different tumor markers. A: primary ascites cells; B: cultured ascites cells, passage 2.

Detection of CTCs with a modified protocol - omitting immunological enrichment by EpCAM nanobeads

There are some indications that EpCAM expression might be lost during blood passage of the cells. This was supported by our experiments staining the ascites cells. Epithelial-mesenchymal transition (EMT) in the progression of ovarian cancer was

often reported in the literature. Due to the low detection rate of 3.5 % of CTCs from blood of time point Q of patients with ovarian cancer, the enrichment protocol was modified and the immunocytochemical investigation of CTCs were directly performed after the gradient separation (Figure 41). For the visualization of the OCDCs, we performed immunostaining directly after the density gradient centrifugation enrichment using the human epidermal growth factor receptor 2 (Her-2), the epithelia membrane antigen (EMA) and the epidermal growth factor receptor (EGFR) in addition to the anti-cytokeratin antibodies amd antibodies against EpCAM (antibody staining cocktail, ASC)

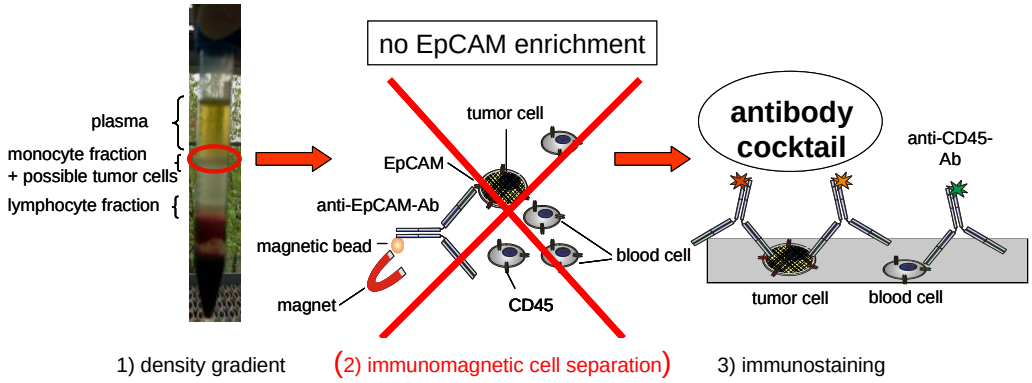

Figure 41: Modified protocol of CTC detection. 1) OC CTC enrichment from the peripheral blood via density gradient centrifugation. The possible tumor cells reside in the monocyte fraction of the density gradient. 2) No further enrichment via immunomagnetic cell separation. 3) For the identification of CTCs, the antibody cocktail against different tumor antigens and for the detection of leucocytes antibodies against CD45 (common leukocyte antigen) were used.

Peripheral blood samples of 87 ovarian cancer patients were analyzed using the modified protocol. CTCs were detected in 27.6% (24/87) of blood samples from the time point Q. These results indicated that the expression level of the epithelial antigens is down regulated in CTCs. The real number of the CTCs might be higher as those, which could be detected by immunocytochemistry. In samples collected at time point H, CTCs could be detected in 7.7% samples (2/26) (Table 30). Staining results are shown in Figure 42.

Table 30: Detection rate of CTCs with modified protocol

time point	protocol	analyzed samples	detectable CTCs	no CTCs
before surgery (Q)	modified protocol	87	24 (27.6%)	63 (72.4%)
6 month after therapy (H)	modified protocol	26	2 (7.7%)	24 (92.3%)

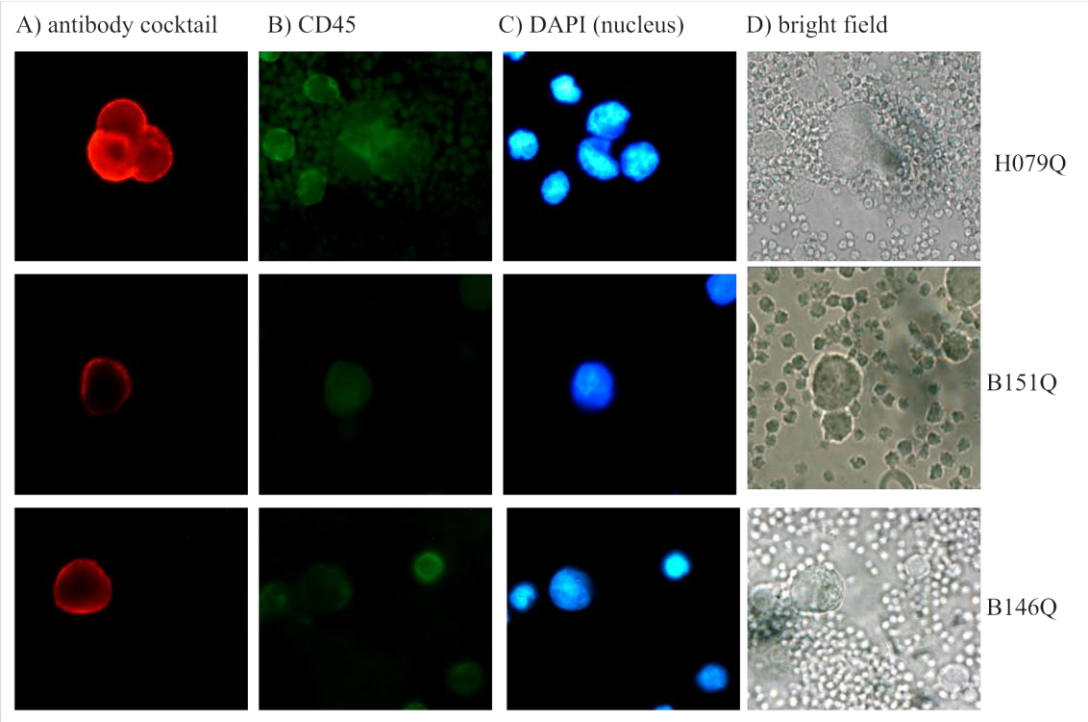

Figure 42: CTCs isolated of the blood samples of ovarian carcinoma patients (samples H079Q, B151Q, B146Q). A: ASC staining of the OCDCs, B: CD45 staining of the leukocytes, C: DNA staining (DAPI), D: bright field.

Characterization of the CTCs by fluorescence in situ hybridization analysis

To confirm the malignancy of immuncytochemical detected CTCs, fluorescence in situ hybridization (FISH) analyses were performed. Partner 8 had identified a region on chromosomal 3q26 by CGH, which was deferent in responder and non-responder patients. The non-responders showed a significant gain in 63% of the analyzed samples.

10 samples that showed the presence of CTCs by immunocytochemistry were further analyzed by FISH. In all samples cells with a DNA gain in the region 3q26 were found (Figure 43), confirming that the cells detected by immunocytochemistry are really tumor cells. Noteworthy, we identified additionally cells with a DNA gain for the chromosomal region 3q26, which were not positive stained by immuncytochemistry (Figure 34C, 34D). These results supported the assumption that the real number of CTCs is higher than those detectable by immunocytochemistry.

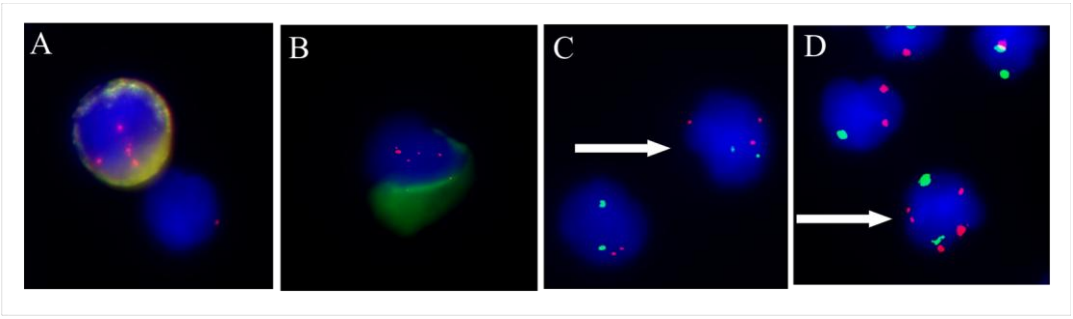

Figure 43: FISH analysis of CTCs for a region in 3q26. A und B: Immuncytochemical positive CTCs with a DNA gain. Red signal: target probe 3q26, green: immuncytochemical staining (CHEEE antibody cocktail). C und D: immuncytochemical negative cells with a DNA gain for the

region 3q26 (white arrow). Red signal: target probe 3q26, green signal: reference probe centromere 7.

Comparison of primary and metastatic ovarian cancer cells

In the blood of patient H071, a high number of CTCs (187 cells/ml blood) was detected that enabled the characterization of these cells with additional markers immuncytochemically. These CTCs were positive for cytokeratin, but negative for EpCAM, EGFR and Her-2. Interestingly, they expressed the mesenchymal marker vimentin, which supported the assumption that the primary epithelial tumor cells had differentiated during the passage and adapt a mesenchymal phenotype (Figure 44, 45).

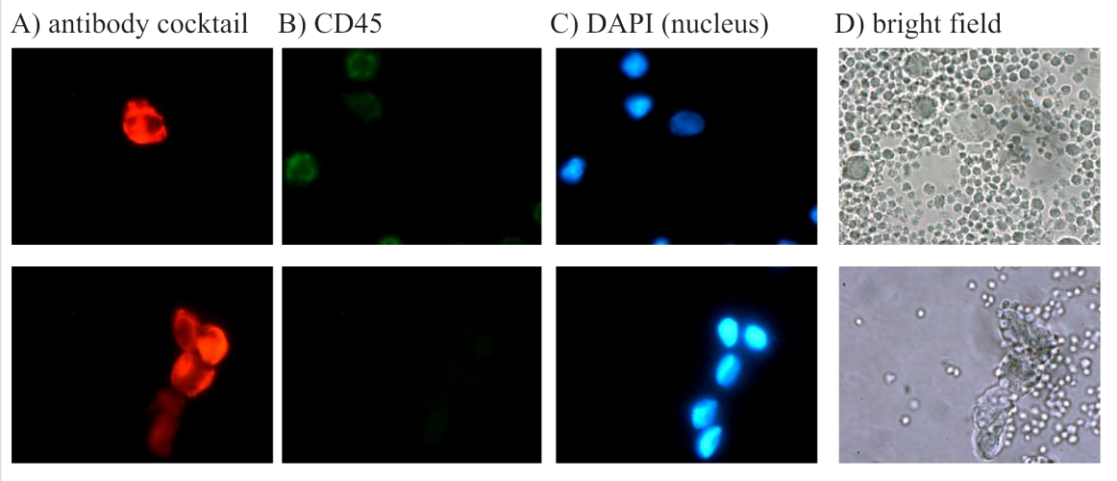

Figure 44: CTCs isolated of the blood sample H071Q. A: ASC staining of the CTCs, B: CD45 staining of the leukocytes, C: DNA staining (DAPI), D: bright field.

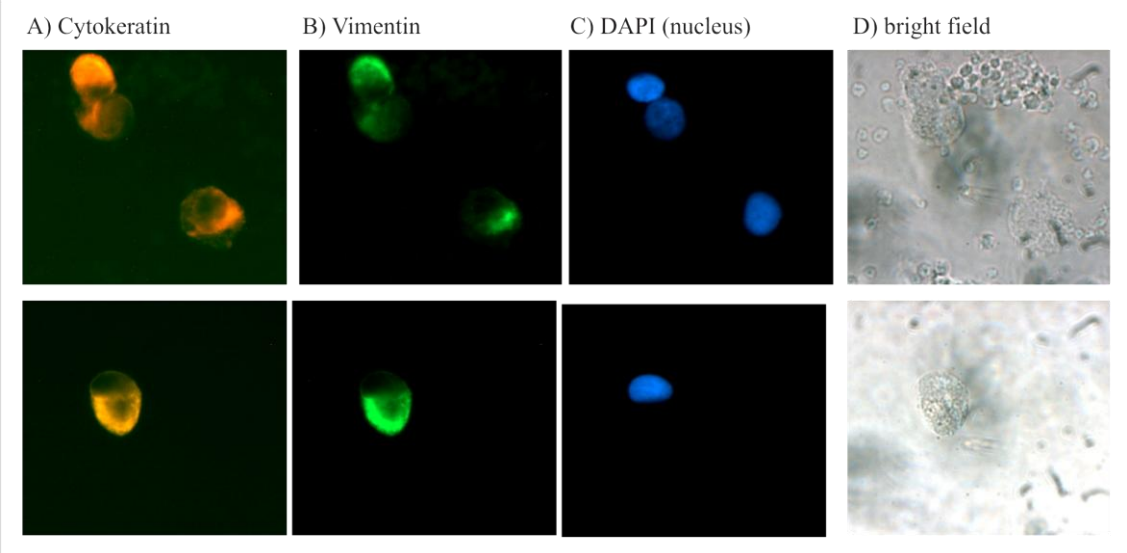

Figure 45: Immuncytochemical characterization of the CTCs positive blood sample H071Q. A: Cytokeratin staining of the OCDCs, B: vimentin staining of the OCDCs, C: DNA staining (DAPI), D: bright field.

At the time point of diagnosis, the patient H071 had already spleen and liver metastases. The cytokeratin and EpCAM expression of the metastases could be detected as the case in primary tumours on paraffin sections (Figure 46). The results correlated with the finding, that the CTCs did not express EpCAM. This observation

leads to the hypothesis that the CTCs could be the precursor cells of metastases, because of there similar expression profile.

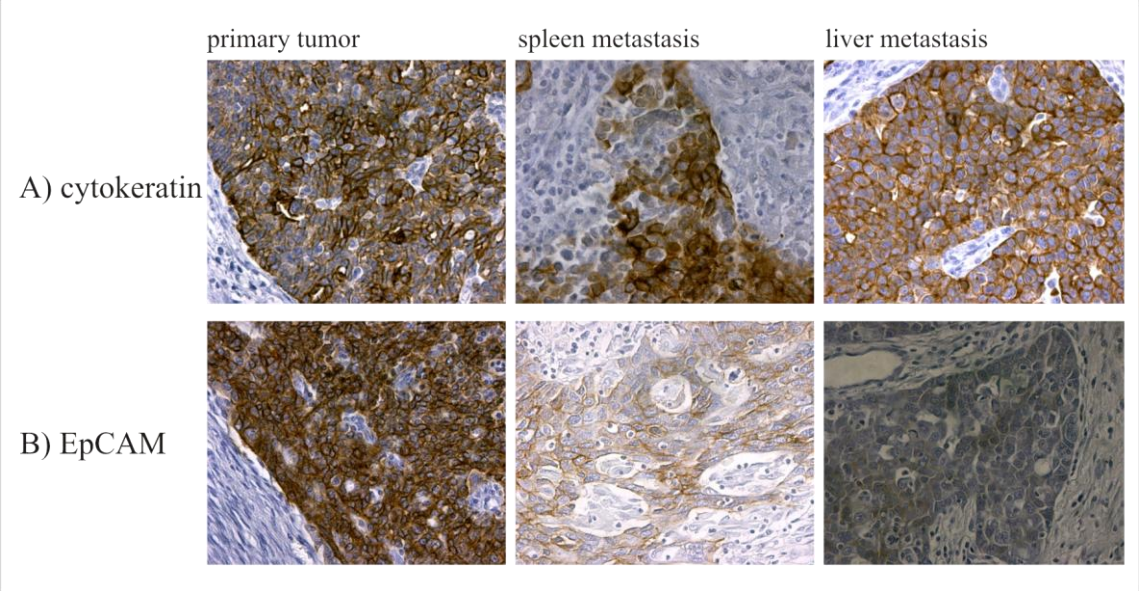

Figure 46: Immunhistological cytokeratin and EpCAM staining on paraffin tissue of the primary tumor, the spleen and liver metastasis from the patient H071.

FISH analysis for chromosome region 3q26 was performed for the further characterizations of the cells. The primary tumous as well as both metastases have a high level gain of the chromosome region 3q26 (Figure 47).

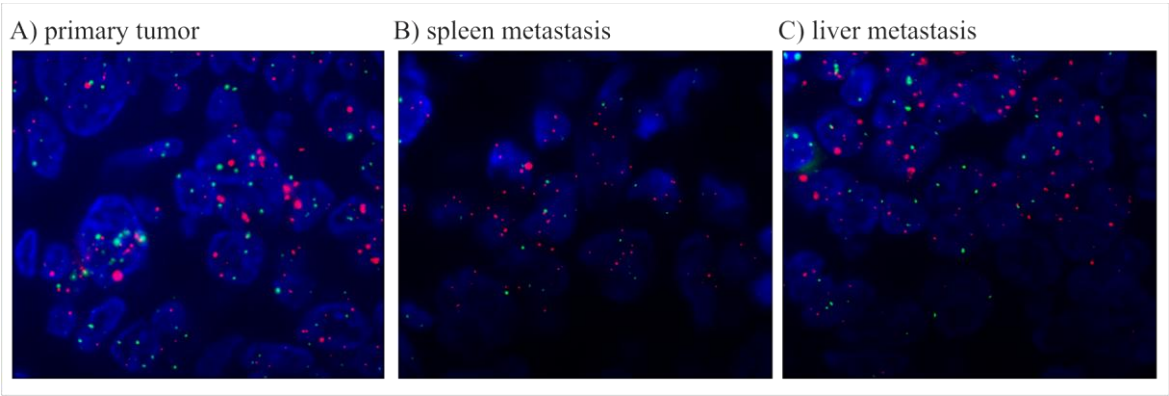

Figure 47: FISH analysis showing cells with gain on chromosome 3q26 on paraffin tissue of the primary tumor, spleen and liver metastasis from the patient H071. A: Primary tumor; B: spleen metastasis; C: liver metastasis. Red signal: target probe 3q26, green signal: reference probe centromere 7.

The major part (approx. 75%) of the CTCs detected by immuncytochemistry did not show DNA gain for the region 3q26 (Figure 48A), while a small part of the cells do (Figure 48B). Again, cells negative for immunocytochemistry showed a DNA gain for the chromosomal region 3q26 (Figure 48C, 48D). To conclude, in the blood circulation there are some disseminated tumour cells, which are do not express the normal epithelial tumour markers, like cytokeratin, Her-2, EpCAM, EMA or EGFR. The CTCs appear to be a very heterogeneous cell population

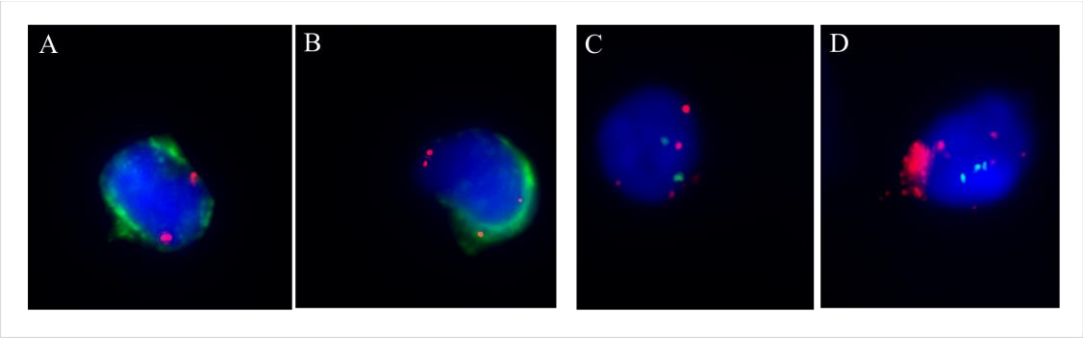

Figure 48: FISH analysis for the chromosome region 3q26 of the blood sample H071Q. A und B: positive CTCs (CHEEE antibody cocktail staining) without and with DNA gain for the region 3q26, respectively. Red signal: target probe 3q26, green: immuncytochemical staining by ASC. C und D: cells negative for the immunocytochemistry staining but with a DNA gain for 3q26. Red signal: target probe 3q26, green signal: reference probe centromere 7.

Taking together, the CTC detection rate was improved from 3.5% to 27.5% when omitting the anti-EpCAM-based nanobead enrichment and applying simultaneously additional antibodies as markers for immunocytochemical staining. DNA gain on the chromosome region 3q26 could be detected in all CTC positive samples defined by immunocytochemistry, suggesting primary tumour as the origin of these CTCs. In addition, cells which were negative for the antibody cocktail staining showed DNA gain, confirming that CTCs lost the expression of epithelial markers in the circulation, especially that of EpCAM. Analysis of blood samples and tumour tissues of patient H071 showed that CTCs might be precursors of metastases or derive from metastasis. In summary, CTCs in ovarian cancer are heterogeneous regarding their protein expression profile and their genetic aberrations.

Detection of CTCs by gene expression markers

In a previous national project carried out by partner 1, led by Robert Zellinger, gene expression markers, which are expressed in ovarian tumous but not expressed in peripheral blood mononuclear cells (PBMCs), were selected. One of the objectives of P1 in OVCAD was to validate these markers in context of predicting response of ovarian cancer patients to standard treatment.

In the course of OVCAD, microarray data was obtained from ovarian cancer tissues (35 patients) and from peripheral blood mononuclear cells (20 healthy female donors, 35 patients). 25 markers with low/absent gene expression in healthy PBMCs and high expression in ovarian cancer tissues were selected. 15 markers were selected from results generated in the previous national project. The expression of these 40 differentially expressed genes was validated in PBMCs obtained from 20 patients with benign ovarian diseases with RT-qPCR. 11 gene markers that had no expression in the benign PBMC were remained for further analysis.

Then the gene expression of these 11 markers was compared in the blood of 174 ovarian cancer patients and 39 healthy females. EpCAM (Epithelial cell adhesion molecule) was analysed as additional gene marker to compare results obtained from RT-qPCR and from immunocytochemistry. The blood samples were taken before the primary surgery. From 69/174 patients, blood samples taken six months after chemotherapy (time point H) were available. Gene expression was normalized to the median expression of three reference genes (B2M, ACTB, and TBP). Due to baseline

gene expression in the healthy PBMC samples, a threshold TX was defined differentiate healthy and diseased individuals and to identify CTC-positive patients. A patient was defined as CTC-positive if at least one of the 11 gene markers was over-expressed. As a results, 50/174 samples from pre-operative blood were CTC positive and 15/69 samples at H time were positive (Table 31).

Table 31. CTCs in pre-operative samples and samples 6 months after therapy

	Number of Patients (%)	
number of over-expressed gene markers	pre-operative	6 months after chemo
≥1	50 (28.7)	15 (21.7)
1	39 (78.0)	13 (86.7)
2	6 (12.0)	2 (13.3)
3	2 (4.0)	0
4	1 (2.0)	0
5	1 (2.0)	0
6	1(2.0)	0

No correlation was found between the occurrence of CTC in blood samples taken before initial surgery and patients' age, response to chemotherapy, recurrence, and residual disease (Table 32); whereas six months after chemotherapy CTC were present significantly more often in older patients and in patients with subsequent recurring disease (Table 33). The presence of CTC before surgery had no influence on patients' progression free and overall survival. Patients still presenting CTC six months after chemotherapy had a significantly shorter overall and progression free survival. Due to the fact that the numbers of patients in the classified groups is very small, the data have to be evaluated in a larger patient cohort.

Table 32: Correlation of CTC presence before surgery with clinical parameters

	Number of patients (%)		p-value
	CTC positive	CTC negative	
Total	50 (29)	124 (71)	
Mean age (yrs)	60.4 (±12.7)	57.5 (±12.0)	n.s.
FIGO stage II/III (N=140) IV (N=30)	 36 (26) 11 (37)	 104 (74) 19 (63)	n.s
Therapy response yes (N=123) no (N=32)	 32 (26) 10 (31)	 91 (74) 22 (69)	n.s
Subsequent recurrence yes (N=81) no (N=78)	 21 (26) 22 (28)	 60 (74) 56 (72)	n.s
Residual disease yes (N=78) no (N=86)	 26 (33) 19 (22)	 52 (67) 67 (78)	n.s

Table 33: Correlation of CTC presence 6 months after chemotherapy with clinical parameters

	Number of patients (%)		p-value
	CTC positive	CTC negative	
Total	15 (22)	54 (78)	
Mean age (yrs)	66.6 (±12.1)	55.4 (±10.9)	0.004
FIGO stage II/III (N=58) IV (N=9)	 11 (19) 4 (44)	 47 (81) 5 (66)	n.s
Therapy response yes (N=57) no (N=10)	 10 (18) 5 (50)	 47 (82) 5 (50)	0.038
Subsequent recurrence yes (N=36) no (N=31)	 12 (33) 3 (10)	 24 (67) 28 (90)	0.021
Residual disease yes (N=39) no (N=29)	 10 (26) 5 (17)	 29 (74) 10 (84)	n.s

Information of CTCs detected with immunocytochemistry was obtained from partner 16. Results obtained with RT-qPCR and immunocytochemistry perfectly agreed in 37/56 (66%) blood samples (81% both negative, 19% both positive). 15/56 (27%) samples were identified by ICC as CTC-positive, but not with RT-qPCR. 4/56 (7%) samples were only identified by RT-qPCR. Interestingly, patients with CTC identified by RT-qPCR only had a significantly worse prognosis than patients with both RT-qPCR- and ICC-negative results.

Cyclophilin C (*PPIC*) was predominantly over-expressed in the blood of CTC+ ovarian cancer patients. These patients had a significantly shorter overall and progression free survival compared to those CTC+ patients without over-expression. In contrast, p-Cadherin (*CDH3*) gene expression had a reverse impact on patient outcome. PPIC and *CDH3* gene expression might characterize CTC with different metastatic potential.

The multivariate survival analysis using a proportional hazards Cox regression model including age, FIGO stage, residual tumor, grade, and PPIC and CDH3 gene over-expression revealed that high FIGO stages, the presence of residual tumor mass, high grad and PPIC overexpression in the blood were significant factors for poorer progression free survival. CDH3 gene expression was associated with improved PFS (Table 34).

Table 34: Cox's proportional hazard regression models for progression free and overall survival

Progression free survival	univariate			multivariate		
	HR	**CI 95%**	**p**	**HR**	**CI 95%**	**p**
Age	1.018	1.002-1.035	0.032			
FIGO	1.953	1.339-2.850	0.001	1.517	0.986-2.334	0.058
Residual tumor	1.574	1.264-1.960	<0.001	1.481	1.176-1.865	0.001
Grade	1.718	1.172-2.519	0.006	1.505	1.009-2.244	0.045
PPIC	1.737	1.097-2.749	0.018	1.640	1.011-2.660	0.045
CDH3	0.283	0.07-1.147	0.077	0.214	0.051-0.894	0.035
Overall survival	**HR**	**CI 95%**	**p**	**HR**	**CI 95%**	**p**
Age	1.045	1.016-1.074	0.002	1.031	1.003-1.061	0.031
FIGO	1.508	0.834-2.726	0.174			
Residual tumor	1.628	1.152-2.300	0.006	1.467	1.030-2.090	0.034
Grade	2.169	1.078-4.361	0.030	1.862	0.920-3.768	0.086
PPIC	2.113	1.097-4.070	0.025			
CDH3	0.046	0-20.659	0.323	no events in one group		

(6) Characterization of multidrug resistance mechanisms

A group in partner 1 led by Theresia Thalhammer aims at investigating the role of multidrug resistance (MDR) mechanisms, particularly the role of membrane drug transporters important for MDR of ovarian cancer.

Multidrug resistance in cell line models

Studies were first done in two ovarian carcinoma cell lines, the drug sensitive, hormone receptor negative A2780 cell line and its adriamycin resistant counterpart, A2780ADR. For kinetic studies, we established an HPLC system to monitor the uptake and intracellular concentration of the taxane derivative paclitaxel, which is applied in ovarian cancer chemotherapy either as a single agent or in combination with platin derivatives.

Expression of drug efflux pumps

Membrane efflux transporter of the ABC family, namely ABCB1 (P-glycoprotein, transporters of ABC group C (MRP1-5) and ABCG2, the "Breast Cancer Resistance-Related Protein" are frequently over-expressed in ovarian cancer cell lines. These ATP-dependent pumps effectively extrude cytotoxic drugs through the cell membrane, and thereby, prevent drug accumulation in the cell interior. Their over-expression results in MDR as cytotoxic concentrations of anticancer drugs are prevented by their increased activity. We investigated, the expression of MDR1 (P-glycoprotein), MRP1, MRP5 and ABCG2 in the ovarian cancer cell lines A2780 and A2780-ADR. Quantitative TaqMan PCR revealed that MDR1 mRNA is over-expressed by 90-100fold in A2780-ADR cells as compared to the parent cell line, while no differences were observed for MRP1 and ABCG2 mRNA expression rates. This was confirmed at the protein level and indicates that P-glycoprotein, but not ABCG2 must confer resistance to anthracylines in these cells.

Sensitivity of cells to paclitaxel

The taxane paclitaxel is a substrate for the efflux transporter P-glycoprotein as well as for the breast cancer resistance protein ABCG2. Therefore, we tested whether parent A2780 and the MDR cell line A2780-ADR (selected by treatment with adriamycin) are sensitive to this compound. Using a modified formazane assay, we show that A2780-ADR cells are approx. 200 times more sensitive to paclitaxel than the parent A2780 cell lines. This was confirmed by cell counting experiments.

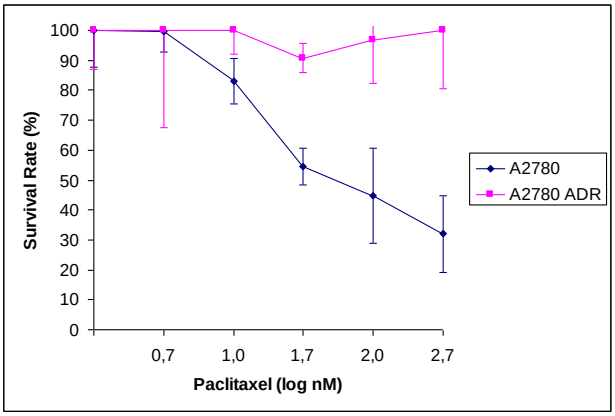

Figure 49: Toxicity of paclitaxel in A2780 and A2780-ADR cells. As expected, parental A2780 but not A2780-ADR cell lines are sensitive to paclitaxel (IC_{50}= 0,05 µM vs >10 µM). This was determined by a modified MTT assay (CCK-8 assay).

Uptake and intracellular concentration of paclitaxel

To answer the questions if, the difference in the sensitivity of A2780 and A2780-ADR cells to paclitaxel is caused by different intracellular concentrations of the drug and if transport modulators can alter intracellular drug concentration by influencing uptake and efflux, we established an HPLC drug assay to monitor paxlitaxel concentration in cancer cell lines.

Figure 50 shows accumulation of paclitaxel in the resistant cell line after applying doses between 0-50 µM. These experiments are in progress and uptake and intracellular concentration reached after different time points and different paclitaxel doses (1-12 hrs) are determined in both cell lines. Also the application of cell cycle modulators and tubulin modifying agents on the intracellular drug concentration is tested.

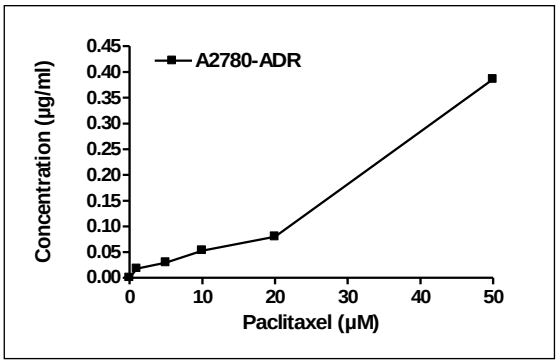

Figure 50. Intracellular concentration of paclitaxel in A2780-ADR cells. Cells were treated with different doses of paclitaxel for 48 hrs before analyzing drug concentrations in the cytosol.

Expression of drug uptake transporters (OATPs)

Public data strongly indicated that not only the efflux but also the uptake into the cells may be altered in MDR cell. To this group belong the uptake transporters of the organic anion transporter polypeptide (OATP) family, which consists of eleven members, which are important for the clinical success of ovarian cancer therapy, as they mediate the cellular uptake of a broad range of endogenous compounds as well as numerous drugs. It was demonstrated that paclitaxel is taken up to the cell interior by at least one OATP, namely OATP1B3, but probably by not yet known OATP family members as well. As preliminary experiments in our lab showed that several OATPs are expressed in normal and malignant breast tissue with strong inter-individual differences, they propose that these transporters are also important in ovarian cancer for the uptake of anticancer drugs, like paclitaxel.

We thus established PCR conditions relevant for screening drug sensitive and drug-resistant human ovarian cancer cell lines for the mRNA expression of human OATP-uptake transporters. An unexpected finding was that drug sensitive and drug resistant cells express a different pattern of OATP mRNA as seen in Table 35 and more transporters are present in the resistant cell line. It is of particular interest that A2780-MDR cells express the known uptake transporters for paclitaxel, namely OATP1B3. Presently, mRNA expression of the taclitaxel uptake transporter OATP8 (OATP1B3) is assessed by quantitative TaqMan PCR at different time points and under different conditions (e.g. pretreatment with paclitaxel or pregnane X receptor inducers). Also transporters OATP2B1 and 3A1, responsible for the uptake of hormones, e.g. estrone-sulfate as well as substrates for the nuclear receptor PXR, which regulates the expression of drug efflux transporters are over-expressed in the resistant cells. Therefore, increased expression of uptake proteins might favour the expression of MDR efflux pumps by increasing the cellular concentration of their inducers. Currently, this hypothesis is tested in the two cell lines.

Table 35: mRNA Expression of OATP uptake transporters
in drug sensitive- and drug resistant A2780 ovarian cancer cell lines

Uptake transport proteins			Ovarian carcinoma cell lines	
OATP	OATP: new nomenclature	bp	A2780	A2780ADR
OATP-A	OATP1A2	655bp	positive	negative
OATP-B	OATP2B1	718bp	negative	positive
OATP-C	OATP1B1	1150bp	negative	negative
OATP-D	OATP3A1	163bp	negative	negative
OATP-E	OATP4A1	291bp	negative	negative
OATP-F	OATP1C1	249bp	negative	positive
OATP-H	OATP4C1	223bp	negative	positive
OATP-I (GST)	OATP6A1	191bp	negative	negative
OATP-J	OATP5A1	272bp	negative	negative
OATP-8	OATP1B3	341bp	negative	positive
PGT	OATP2A1	350bp	positive	Positive

It is of particular interest that OATP1B3 responsible for the uptake of paxlitaxel is particularly found in MDR A2780ADR cells. Therefore, it seems that these cells tried to increase uptake mechanism to compensate for the increased drug efflux, although this does not seem to lead to higher intracellular drug concentrations. However, its expression as well as the expression of other drug transporters in drug refractory cells is still not clear.

Resistance to Paclitaxel

Membrane uptake transporters of the SLCO/OATP (solute carrier organic anion transporter/organic anion transport polypeptide) family were previously identified to mediate the uptake of the cytostatic drug paclitaxel (PAX) into *Xenopus l.* oocytes. To study the impact of drug uptake transporters of the OATP family in ovarian cancer cells, we investigated drug uptake in the four ovarian cancer cell lines A2780, multidrug resistant (MDR), P-glycoprotein overexpressing A2780ADR, OVCAR-3, and SKOV-3 cells. mRNA expression of various OATPs as well as of ABC-transporters was assessed by TaqMan PCR. A number of OATPs could be identified in all cell lines. However OATP1B3, which had been previously identified as a PAX-uptake transporter into *Xenopus l.* oocytes, was only found in SKOV-3 cells, only. Additionally, we determined mRNA expression of SLC22A7 (hOAT2), an organic anion transporter with highest affinity to PAX as substrate. However, expression of this transporter seems to be mainly confined to liver, while the ovarian cancer cell lines were clearly negative for this transporter. Uptake studies using HPLC showed that incubation of cell lines with PAX for 30 min leads to a 24-fold lower intracellular accumulation of the drug in A2780ADR cells (0.044µg/mg protein/h) as compared to A2780 cells (1.06µg/ mg protein/h). Similar values were obtained for the two other cell lines, OVCAR and the OATP-overexpressing SKOV-3 cells. These results suggest that P-gp is the main determinant for PAX sensitivity, while expression of uptake transporters, e.g. OATP1B3, seems to be of minor importance for the cellular accumulation of PAX. In line with these observations, the P-gp inhibitor verapamil caused a dose-dependent increase in PAX toxicity only in A2780ADR cells.

Exposure of ovarian cancer cell lines to PAX effectively reduced the growth of A2780, SKOV-3 and OVCAR cells with IC_{50} of 5-10 nM, while A2780ADR cells were highly resistant to doses up to 1 µM PAX. Remarkably, after 10 days, A2780ADR cells became resistant to even higher concentrations of PAX (>1 µM PAX). After this time period, A2780ADR cells escaped the growth inhibitory effect of this high dose. This may be explained by a further selection of P-gp-overexpressing cells in the A2780ADR population and this process is currently studied by FACS analysis.

Further studies on drug efflux transporters were done in cooperation with Dr. Martina Czechova from the laboratory led by Prof. F. Staud, Department of Pharmacology and Toxicology, Charles University in Prague, Faculty of Pharmacy, Hradec Kralove, Czech Republic. In addition to the expression of ABCB1 (P-gp), we could also show that other drug efflux pumps are expressed in A2780 and A2780ADR cell lines. ABCC1-6, ABCC11 coding for the MDR-related proteins (MRPs1-6 and MRP11, respectively) were assessed by quantitative PCR in ovarian cancer cell lines A2780 and A2780ADR. However, only ABCC2, coding for MRP2 was higher expressed in the resistant than in the sensitive cell line. MRP3, involved in efflux of anionic conjugates of anticancer drugs, as well as MRP6 (ABCC6), which is not involved in

MDR but mutations are responsible for a metabolic genetic disease *(Pseudoxanthoma elasticum)* were not detectable in both cell lines. No differences in the expression of ABCC1, ABCC4, ABCC5, ABCC11 and ABCG2 were found between the drug sensitive and resistant cell lines.

Impact of the nuclear receptor PXR

We also investigated a possible regulation of drug membrane transporter expression through the chemosensitizing pregnane-X-receptor (PXR). PXR belongs to the group of nuclear receptors and is present in tissue with high rates of drug metabolism, e.g. liver, intestine, but was also found in a number of tumor cells. PXR is activated by rifampicin resulting in an increased expression of PXR target genes such as metabolizing enzymes, drug uptake and efflux transporters. However, using qPCR, we did not detect significant PXR expression in these cell lines applying primers, which detect three common PXR isoforms. In the Western blot analysis, no PXR protein was detectable at the proposed molecular mass. Therefore, we concluded that PXR is not present in the ovarian carcinoma cell lines or, alternatively, these cell lines contain another rare mutant, which might not be sensitive to rifampicin induction. These concepts are currently investigated. In accordance with the lack of wt PXR, we did not observe PXR-mediated alterations in the expression of transporters, e.g. P-glycoprotein. However, as rifampicin increased PAX toxicity only in A2780ADR cells, competitive inhibition of P-gp-mediated PAX excretion by the P-gp substrate rifampicin is likely.

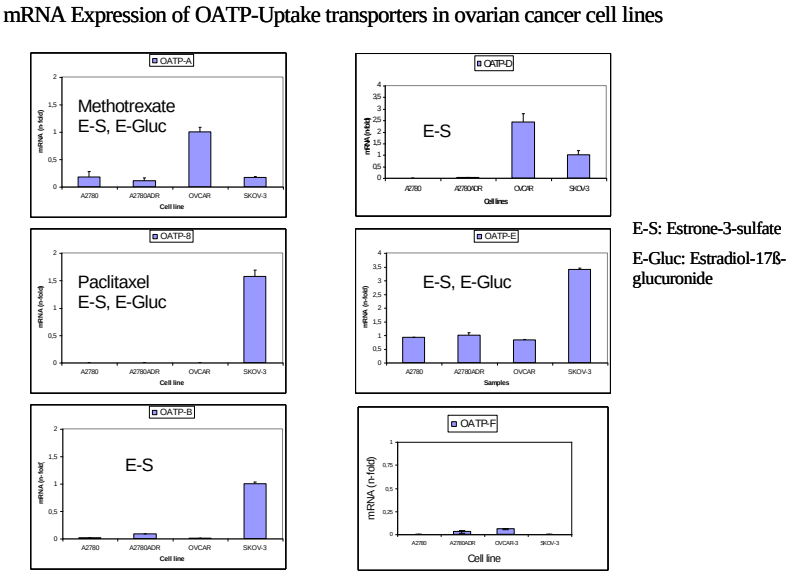

Figure 51. OATP-uptake transporters in ovarian cancer cell lines and specimens from patients

On the other hand, mRNA expression of OATPs, which mediate the uptake of estrone-3-sulfate, namely OATP1A2, OATP2B1, OATP3A1, and OATP4A1 is widely found in all ovarian cancer cell lines and in tissue specimens from ovarian cancer patients (Figure 52).

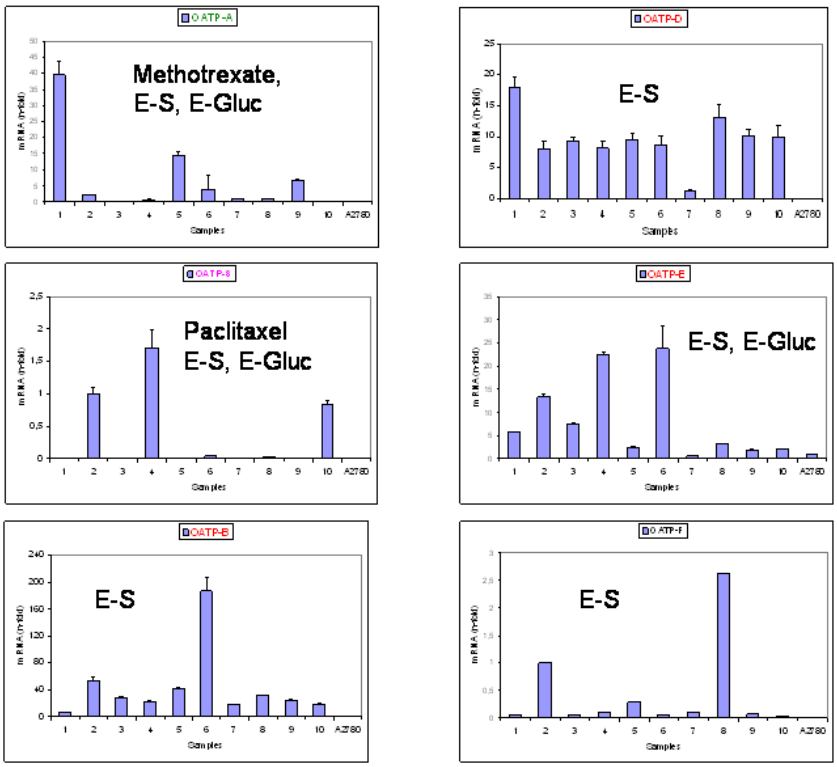

Figure 52: OATP-Uptake transporter OATP-A (methotrexate) is present in many ovarian cancer specimens, while OATP-8 (paclitaxel) is only detectable in some samples, while estrone-sulfate uptake transporters (OATP-B,D,E) are widely expressed at high rates

Taken together, our data suggest that drug efflux pumps including P-gp control the sensitivity of ovarian cancer cells to cytotoxic drugs (PAX), while OATP uptake transporters seem to be important for estrogen homeostasis in hormone sensitive ovarian cancer.

As our findings on high expression levels of OATP uptake transporters (OATP-B, -D, E) in ovarian cancer cells indicate that E_1S might taken up into ovarian cancer cell lines in order to provide a storage for the hormone (Figure 53). Through the activity of steroid-sulfatases (STS, arylsulfatase A and B), estrone (E_1) will be liberated from the non-active E_1S. E_1 can be converted into 17ß-estradiol (E_2) through the active 17ß-hydroxysteroid-dehydrogenase1 (17ß-HSD_2) and vice versa E_2 is converted back to E_1 via the 17ß-hydroxysteroid-dehydrogenase 2 (17ß-HSD_1). Inactivation of E_1 will occur through sulfonation via estrogen-sulfotransferases (SULT1E1, SULT1A1, SULT2A1).

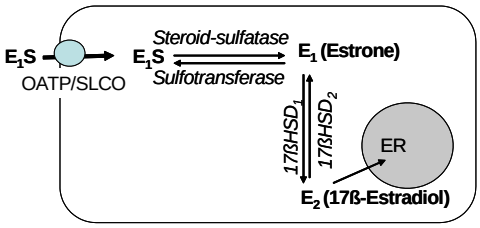

Figure 53: The estrogen storage system in ovarian cancer cells

Using TaqMan PCR, expression of steroid-sulfatase (STS) was detected in all cancer cell lines and in samples from patients with ovarian cancer. Therefore, ovarian cancer cells should be able to generate the active hormone from the sulfated compound.

Interestingly, STS mRNA levels in SKOV-3 cells were 5-fold higher than in other cell lines (Figure 54). However, SKOV-3 cell do not express functional estrogen receptors and, therefore, it is not clear, whether an estrogen storage system might be active in these cells.

STS was found in all specimens from patients with ovarian cancer (Figure 54). Remarkably, STS levels were higher in younger patients and might reflect the overall activity of the hormone in the premenopausal patients. Expression of other sulfatases, namely arylsufatase A and B as well as estrogen-inactivating SULT1E1 was determined in all ovarian cancer cell lines (Figure 55).

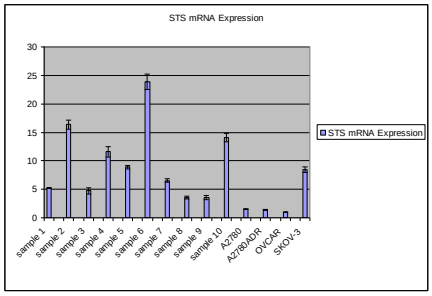

Figure 54. Expression of steroid- sulfatase (STS) in ovarian cancer cell lines and specimens from ovarian cancer patients.

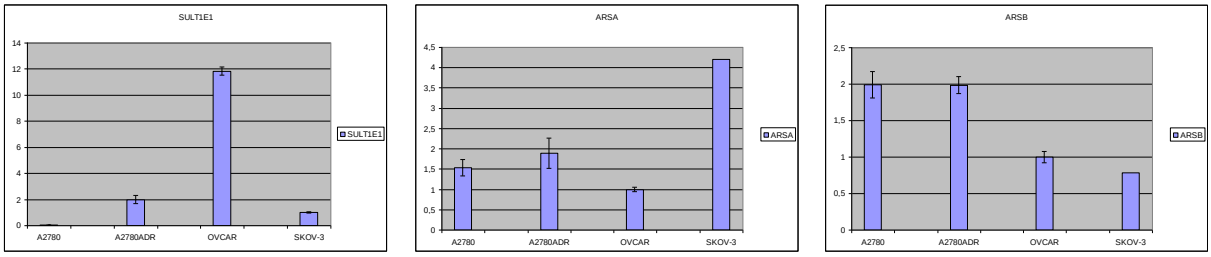

Figure 55. Expression of estrogen-sulfotransferase (SULT1E1) and arylsulfatase A and B in ovarian cancer cell lines.

Remarkably expression of sulfatase A, which is also active in estrogen-sulfate conversion is high in SKOV-3 cells, whereas OVCAR-3 cells do not express considerable amounts of sulfatases, but contain estrogen-sulfotransferase SULT1E1. Therefore, estrogen sulfonation may prevent estrogen effects in the estrogen receptor positive OVCAR-3 cells. Interestingly, SULT1E1 was also induced in MDR-cells. Together with P-gp and CYP3A4, SULT1E1 might form a sort of chemical protection in MDR cell lines.

Drug metabolizing enzymes in ovarian cancer cell lines

During the studies on the resistance of ovarian cancer cells against various chemotherapeutic agents, we discovered that drug metabolizing enzymes of phase I might be active in the ovarian cancer cell lines. Through cooperation with Prof. Jukka Hakkola (Department of Pharmacology and Toxicology, University of Oulu, Oulu, Finland) mRNA expression of CYP enzymes involved in the metabolism of various anticancer drugs is investigated.
CYP1A1: all cells are positive and the expression level is similar and to liver
CYP1A2: no expression
CYP1B1: expressed in all cell lines at comparable levels and similar to that of liver

CYP2A6/CYP2A7: no expression
CYP2B6/CYP2B7: expression level in all cell lines, but much lower than in liver
CYP2C8-19: no expression
CYP2D6: expression of variant CYPs
CYP2E1: expression in all cell lines, but expression levels are lower than in liver
CYP2F1: mRNA detected only in A2780 cells. This is remarkably, as this enzyme is not expressed in liver. Expression appears to be a little higher in ADR cells. Rifampicin has no effect
CYP3A4: expression in all cell lines, but expression is upregulated in ADR cells. Rifampicin has no effect
CYP3A5/CYP3A7: no expression

These studies are of particular interest as it was shown that CYP3A4 up-regulation accompanies induction of drug resistance transporters like P-gp in some MDR cancer lines. This is usually explained by induction via the nuclear receptor PXR. However there are also variant forms of PXR that are not activated by rifampicin, but by etoposide and doxorubicin. These variant forms of PXR might not have been detected in our qPCR assay, or alternatively, another nuclear receptor might regulate CYP3A4 induction in ovarian cancer. Therefore, we are looking for the mechanism for CYP3A4 up-regulation in resistant cell line using long (13 kb) promoter constructs for CYP3A4.

Expression of eleven OATPs in ovarian tumours and in the ovarian cancer cell ines

The transcriptional expression levels of all eleven SLCOs (SLCO1A2. 1B1. 1B3. 1C1. 2A1. 2B1. 3A1. 4A1. 4C1. 5A1. 6A1) were determined in tissue samples by quantitative RT-PCR. All eleven transporters of the SLCO family could be detected in ovarian cancer tissue, although their expression levels varied greatly in the individual specimens. All SLCOs, except SLCO1C1, were also detectable in at least one cell line.

SLCO2A1. SLCO2B1. SLCO3A1 and SLCO4A1 were expressed in every ovarian tissue specimen (Table 35). This is in line with their broad distribution throughout the human body. These SLCOs were also detected in both ovarian carcinoma cell lines, except SLCO2B1, which was found only in SK-OV-3 cells. Remarkably, SLCO5A1, a transporter for which the tissue distribution and substrate specificity is not clearly established, is present at considerable levels in normal and malignant ovarian tissue specimens and in OVCAR-3 cells.

Surprisingly, the “liver specific” SLCO1B1 and SLCO1B3 (23), and “kidney specific” SLCO4C1 were expressed in ovarian carcinoma samples and cell lines. SLCO4C1 was present in normal ovary, but generally, its expression levels were low in all but one sample. Interestingly, coexpression of the paclitaxel transporters SLCO1B3 and 1B1 was found in specimens from three younger patients only. A possible relation between the expression of these two transporters and the age of patients may be assessed in future studies.

All SLCOs except SLCO1C1 were also present in the ovarian cancer cell lines, either in both, or in SKOV-3 (SLCO1A2. 1B3. 2B1. and 6A1) or OVCAR-3 cells (SLCO5A1) alone. This makes these cell lines a valuable tool to be used in the investigation of SLCO-mediated transport. Differences in expression levels of the

paclitaxel transporting protein SLCO1B3 and the presence of SLCO1B1 in the two cell lines could influence the cellular accumulation of paclitaxel.

Table 36. mRNA expression level compared to reference gene (HPRT1)

Gene symbol	N	1	2	3	4	5	6	7	8	9	10
SLCO1A2	ND	1.31±0.11	0.08±0.00	ND	0.02±0.01	0.48±0.02	0.13±0.10	0.04±0.00	0.04±0.00	0.20±0.00	ND
SLCO1B1	ND	ND	2.33±0.33	ND	1.19±0.06	ND	ND	ND	ND	ND	0.40±0.00
SLCO1B3	ND	ND	1.27±0.08	ND	2.18±0.30	ND	0.06±0.01	ND	0.04±0.00	ND	0.10±0.00
SLCO1C1	ND	ND	0.04±0.00	ND	ND	ND	ND	ND	0.10±0.00	ND	ND
SLCO2A1	4.35±0.15	0.96±0.30	3.03±0.29	1.02±0.14	1.03±0.04	1.33±0.25	3.05±0.39	0.37±0.01	2.02±0.14	0.31±0.01	0.42±0.05
SLCO2B1	103±2.02	1.13±0.09	9.36±1.14	4.90±0.39	3.91±0.27	7.23±0.36	32.4±6.86	3.32±0.24	5.50±0.57	4.19±0.35	3.33±0.29
SLCO3A1	1.88±0.04	2.76±0.12	1.23±0.14	1.45±0.18	1.25±0.08	1.48±0.07	1.34±0.13	0.19±0.01	2.03±0.16	1.56±0.13	1.54±0.13
SLCO4A1	0.38±0.01	0.22±0.01	0.50±0.03	0.31±0.01	1.22±0.05	0.07±0.00	1.00±0.28	0.02±0.00	0.12±0.01	0.06±0.01	0.06±0.00
SLCO4C1	0.02±0.00	0.05±0.02	0.05±0.01	0.03±0.01	0.04±0.00	0.02±0.01	0.67±0.09	0.03±0.00	0.15±0.00	0.04±0.00	ND
SLCO5A1	0.41±0.06	1.34±0.41	0.62±0.09	0.12±0.12	0.25±0.04	0.63±0.12	0.12±0.06	0.09±0.00	0.29±0.03	0.13±0.00	0.06±0.01
SLCO6A1	ND	0.31±0.10	0.03±0.02	ND	0.03±0.01	0.07±0.02	ND	ND	ND	0.12±0.00	0.05±0.01

Uptake of paclitaxel into ovarian cancer cell lines

Membrane uptake transporters of the SLCO/OATP (solute carrier organic anion transporter/organic anion transport polypeptide) family may mediate the uptake of paclitaxel in ovarian cancer cell lines. Regarding the expression of various SLCOs in SK-OV-3 and OVCAR-3 cells, we show higher expression levels of the paclitaxel transporter SLCO1B3 in SK-OV-3 cells but both cell lines express considerable levels of the other paclitaxel transporter SLCO1B1. Surprisingly, uptake of paclitaxel did not show saturation kinetics (up to 10 µM) in SK-OV-3 cells, while in OVCAR-3 cells the initial uptake of paclitaxel showed saturation kinetics, with K_m and V_{max} values of 17.25 ± 4.12 µM and 517.5 ± 86.21 pmol/mg of protein/min. respectively. Exposure of ovarian cancer cell lines to PAX effectively reduced the growth of SKOV-3 and OVCAR-3 with IC_{50} of 5-10 nM (Figure 56).

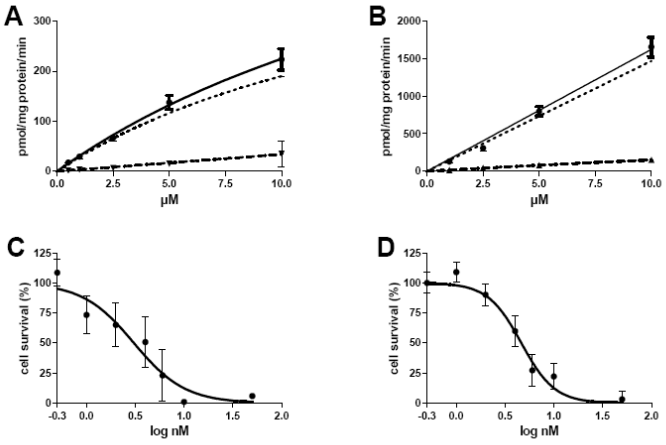

Figure 56: Uptake (A. B) and cytotoxicity (C. D) of paclitaxel in the ovarian cancer cell lines OVCAR-3 and SKOV-3, respectively.

To date, no other SLCOs have been identified for paclitaxel transport and the paclitaxel transporting SLC22A7 was undetectable in both cell lines. Differences in the uptake cannot be explained by differences in the SLCO expression. However, efflux via specific ABC-efflux pumps, which are expressed differently in the two cell

lines, may influence initial uptake rates. Indeed, in SLCO1B3 expressing SK-OV-3 cells, an approximately 6-fold higher expression of ABCC3 coding for the paclitaxel resistance conferring protein, MRP3, might counteract SLCO1B1 and 1B3 mediated uptake, thereby limiting the intracellular paclitaxel accumulation. This might prevent saturable uptake of paclitaxel in the range of soluble concentrations in the incubation medium (up to 10µM. Table 37).

Table 37: Expression of OATP/SCLO-transporters (left) and MDR-efflux (right) pumps in ovarian cancer cell lines OVCAR and SKOV-3

Gene symbol	OVCAR-3	SK-OV-3
SLCO1A2	**0.03 ± 0.00**	ND
SLCO1B1	0.29 ± 0.02	**1.0 ± 0.1**
SLCO1B3	ND	**2.0 ± 0.1**
SLCO1C1	ND	ND
SLCO2A1	0.15 ± 0.01	**0.15 ± 0.02**
SLCO2B1	ND	**0.17 ± 0.02**
SLCO3A1	**0.37 ± 0.03**	0.15 ± 0.01
SLCO4A1	0.03 ± 0.00	**0.16 ± 0.01**
SLCO4C1	**0.08 ± 0.01**	ND
SLCO5A1	**0.37 ± 0.02**	ND
SLCO6A1	**0.01 ± 0.00**	ND

ABC-Transporter	OVCAR-3	SK-OV-3
ABCB1	ND	**1.3 ± 0.1**
ABCC1	139.8 ± 9.8	**545.2 ± 54.5**
ABCC2	0.7 ± 0.0	**21.9 ± 2.2**
ABCC3	84.6 ± 4.5	**516.1 ± 51.6**
ABCC4	44.7 ± 5.8	**362.2 ± 36.2**
ABCC5	24.6 ± 0.1	**65.8 ± 6.6**
ABCC6	**4.0 ± 0.4**	ND
ABCC10	4.5 ± 0.4	**4.9 ± 0.3**
ABCC11	0.5 ± 0.3	**16.6 ± 1.7**
ABCG2	ND	ND

Although OATP1B3 is known to mediate the uptake of paclitaxel in hepatocytes, no further studies are available to characterise any other OATP family members to be able to transport this anticancer agent. As similar to our findings in ovarian cancer, also other groups showed that OATPs are differently expressed in breast, lung, and liver cancer as compared to the non-malignant tissue; we tried to identify further OATP members with specific transport activity for paclitaxel. These informations together with data about inter-individual differences in OATP expression could contribute to explain altered response rates in cancer patients treated with OATP substrates.

Paclitaxel transport studies in Xenopus laevis oocytes

Paclitaxel uptake was investigated in *X. laevis* oocytes injected with cRNA coding for each of the OATP family members A 5.3 fold ($p<0.0001$) and 3.9 fold ($p<0.0001$) higher accumulation was seen in OATP1B1 and OATP1B3 expressing oocytes, respectively, as compared to the water control (Figure 57). Transport of paclitaxel in all other OATPs did not reach statistical significance. For further kinetic characterisation of OATP1B1 and 1B3 mediated paclitaxel transport we studied the time-dependent influx over a period of 120min. (Figure 58). For both transporter proteins the time point of 60 min showed to be within the linear phase and was therefore selected for concentration-dependent studies. For saturation kinetic analysis unlabeled paclitaxel was added to reach a final concentration range from 20 to 1180 nM. We observed saturable transport for OATP1B1 with a V_{max} rate of 12.29 ± 0.41 fmol/oocyte/min and a K_m value of 582.1 ± 42.4 nM. OATP1B3 showed a V_{max} of 29.96 ± 1.97 fmol/oocyte/min and a K_m of 1582 ± 166.3 nM. Additionally, we confirmed ectopic oocyte protein expression and membrane localization of human OATP1B1 and 1B3 by Western blot analysis.

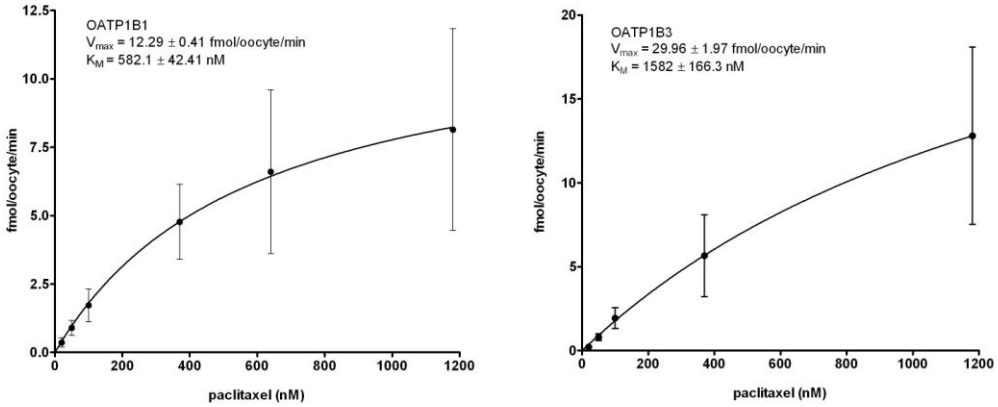

Figure 57: Kinetics of paclitaxel uptake of OATP1B1 and 1B3 expressing *X. laevis* oocytes.

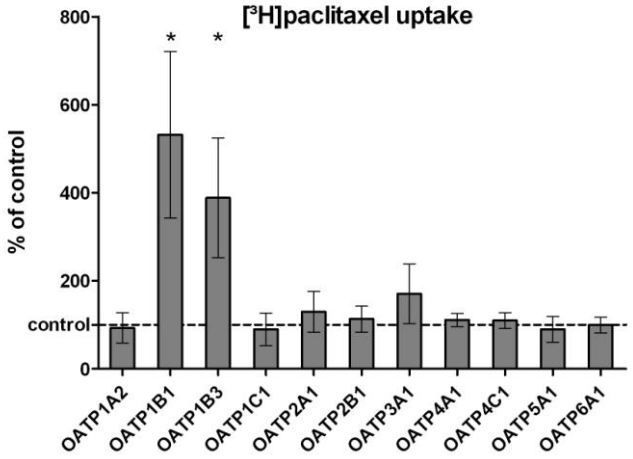

Figure 58: Paclitaxel uptake in different OATPs, expressed in *X. leavis* oocytes

We further investigated transport of 20 nM [³H]E3S and [³H]DHEAS in OATP5A1 and 6A1 since their substrate specificity is virtually unknown. Although E3S belongs to the best characterised substrates among the OATP family, data about transport activity of OATP5A1 and 6A1 is lacking. Moreover, OATP6A1 is predominantly expressed in testis and it has been already reported that the putative rat orthologues Oatp6b1 and Oatp6c1 transport DHEAS. However, in the *X. laevis* oocytes expressing the respective OATP, neither OATP5A1 nor OATP6A1 showed significant transport activity for both compounds (data not shown).

(7) Approaches on the incorporation of targeted therapies

There is an urgent need for alternative therapies as there are no further treatment modalities available for chemoresistant tumours. Antibody therapeutics with pro-apoptotic potential in combination with passive immunotherapy may help to overcome this problem. Partner 5 led by Peter Altevogt and partner 6 led by Mina Fogel found that expression of L1 augmented cell motility, tumour growth of carcinomas xenografted in NOD/Scid mice, and up-regulated erk-dependent genes when ectopically expressed in HEK293 cells. P5 identified an amino acid motif responsible for the upregulation of erk-dependent genes. The objectives in regard of targeted therapies were to characterize the L1-regualted genes in ovarian cancer and to evaluate the L1-based therapy in NOD/Scid mice.

Characterization of L1-regulated genes in ovarian carcinoma

We previously observed that L1 overexpression lead to enhanced cell migration on fibronectin and laminin and also augmented matrigel invasion. We now analyzed whether the overexpression of L1 also affected tumor cell growth in NOD/Scid mice. We examined the ovarian carcinoma cell line 130 that is negative for L1 but expresses L1 after retroviral trunsduction. We observed that L1-GFP (green fluorescent protein) expressing cells had increased tumor volume compared to GFP-empty vector expressing m130 cells (Figure 59A). A similar analysis was carried out in HEK293 cells stably transduced with L1. Also in this experimental system the L1 expression lead to enhanced cell motility and invasion (not shown) and significantly augmented tumor formation in mice (Figure 59B, 59D).

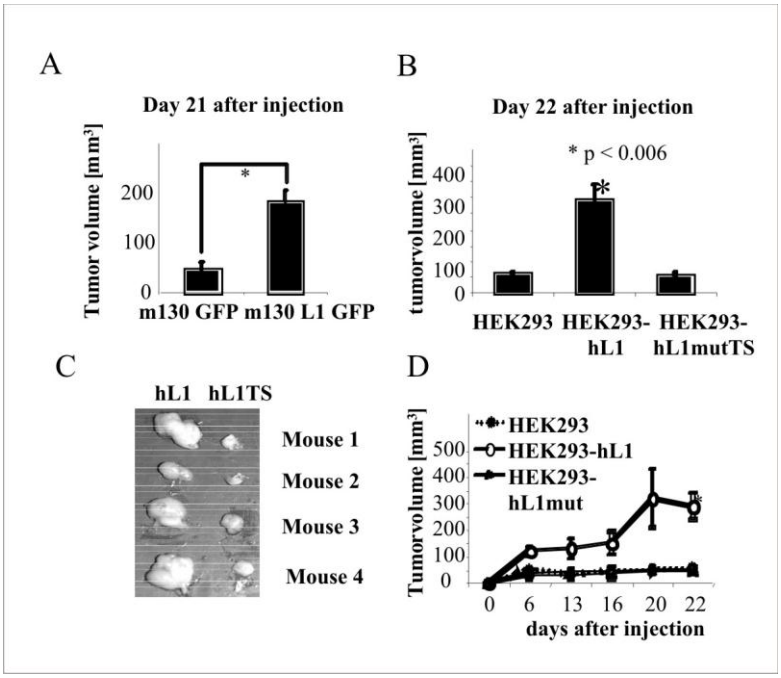

Figure 59: Effect of L1 over-expresssion on tumor growth. A) Tumor growth in NOD/Scid mice was compared between m130 mock–transfected and L1-retrovirus transduced cells, B) L1 expression augmented tumor formation of HEK293 cells stably transduced with L1. An L1 mutant form devoid of the ERK phosphorylation site in the cytoplasmic portion did not have this effect, C) Tumor size of HEK293-hL1 versus HEK293-hL1mutTS. Tumor cells were inoculated on the left or right back site of the same animal, D) Time course of tumor growth.

Investigation of the effect of L1 on gene expression

Using mRNA from HEK293 or HEK293-hL1 (Figure 60, 61A) cells we probed an oncochip containing 1920 tumor related cDNAs. We identified numerous mRNAs that were differentially expressed (Figure 61B). Many of the genes regulated were reconfirmed by qRT-PCR and Western blot analysis. We assumed that the altered gene expression pattern might contribute to the enhanced tumor growth seen in NOD/Scid mice.

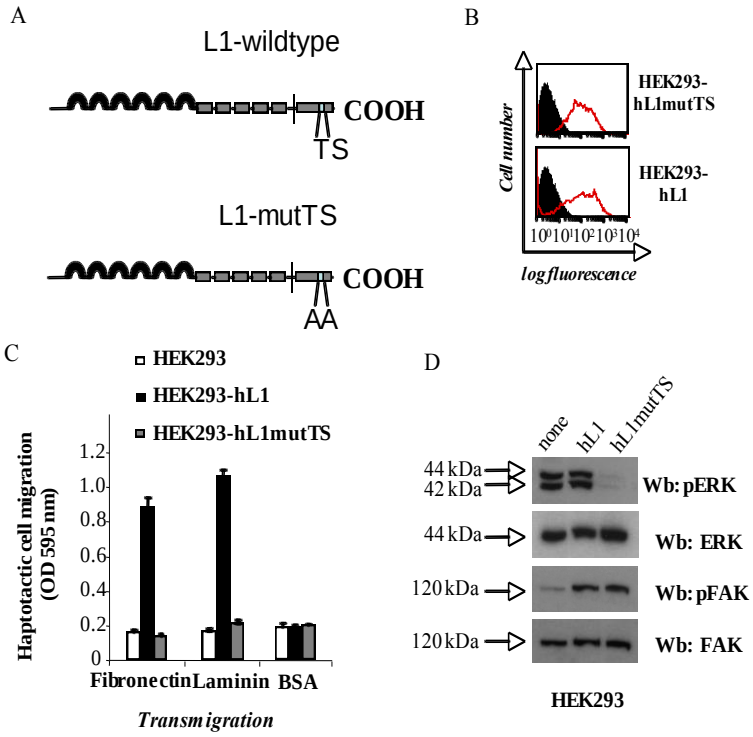

Figure 60: Characterization of HEK293-hL1mutTS cells. A) Schematic representation of the structure of hL1-wildtype and hL1-mutTS. Note that the ERK phosphorylation site in L1 was removed in the mutant. B) Stable expression of hL1 and hL1mutTS in HEK293 cells as revealed by FACS analysis. C) Analysis of haptotactic cell migration of transfected HEK293 cells on fibronectin or laminin as substrate. Bovine serum albumin (BSA) was used as negative control. D) Analysis of ERK and FAK phosphorylation in untransfected HEK293 and transfected cell lines. Cells were grown in 10% FCS and lysates were examined by Western blot analysis with the indicated antibodies. Note that hL1mutTS suppresses ERK phosphorylation.

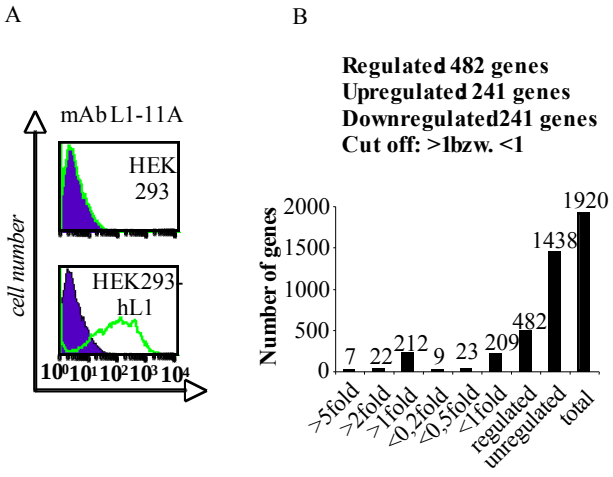

Figure 61: Analysis of L1-regulated genes. A) FACS analysis of HEK293 and HEK293-hL1 cells used for gene expression profiling, B) Summary of changes in gene expression between the two cell lines (fold increase or decrease represents the mean of three independent hybridisations).

Investigation of the responsible part of L1 molecule responsible for tumor growth and gene regulation

We initially studied a form of L1 in which the cytoplasmic portion was deleted. This construct when stably expressed in HEK293 cells did not reveal enhanced motility, invasion and tumor growth in mice. Since L1 interacts with ERK, we mutated the ERK-phosphorylation site in the cytoplasmic tail of L1 (hL1mutTS). A schematic representation of the mutant and wildtype L1 forms is depicted in Figure 60. The mutant L1 form was stably expressed in HEK293 cells and the biological effects were characterized. We observed that the hL1mutTS mutant had lost the ability to promote tumor formation in NOD/Scid mice (Figure 61). Further analysis showed that the HEK293-hL1mutTS mutant could not promote L1-enhanced motility on fibronectin and laminin (Figure 60C). Interestingly, the analysis of the activation status of ERK and FAK in transfected HEK293 cells revealed that hL1mutTS could suppress ERK activation in the transfected cells (Figure 60D). A previous publication by Silletti et al (2004) had shown that L1-mediated ERK activation is instrumental for L1-promoted gene regulation.

Effect of hL1mutTS in L1-mediated gene regulation

We found that hL1mutTS could efficiently suppress L1-mediated gene regulation in HEK293 cells (Figure 62). Similar results were obtained when hL1 or hL1mutTS were expressed in SW707 colon carcinoma cells (data not shown). We concluded that L1 can alter the gene expression profile in two carcinoma cell lines. L1-dependent gene regulation appears to be linked to tumor growth, motility and invasiveness of carcinoma cells.

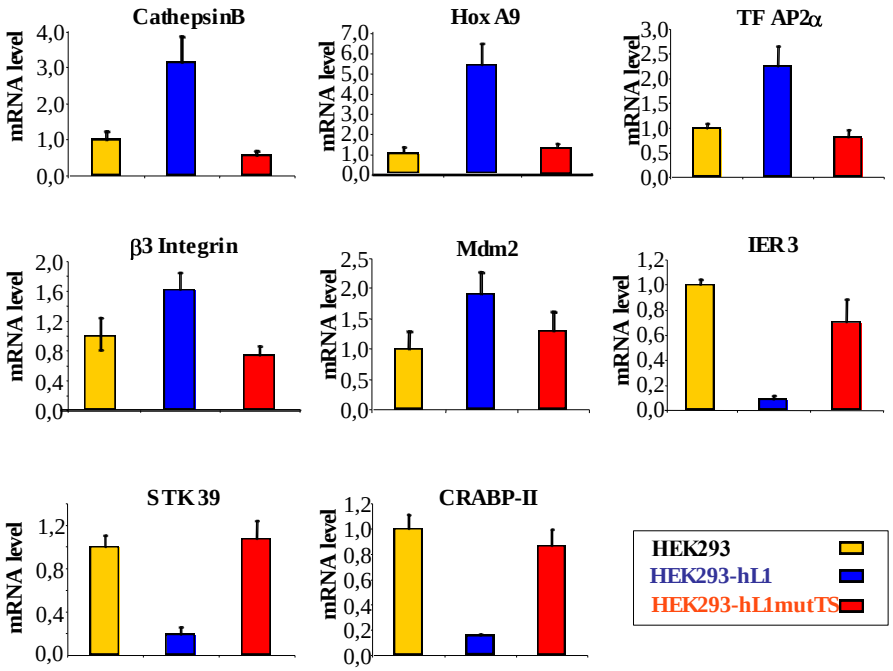

Figure 62: Suppression of L1-mediated gene regulation by hL1mutTS. The mRNA was isolated from the indicated HEK293 cells or L1-transfectants, reverse transcriped to cDNA and analyzed for the indicated genes by quantitative RT-PCR. Note that L1-mediated gene regulation is reversed to normal HEK293 expression levels in hL1mutTS expressing cells. This mutation rendered the molecule inactive.

Antibodies to L1 alter L1-dependent signalling in ovarian carcinoma cells

We have shown that antibodies to L1 can suppress the tumour growth of SKOV3ip cells in a xenograft mouse model (Arlt *et al.*, 2006, Knogler *et al.*, 2007). We speculated that the mutant and the treatment with mAbs may have mechanistic similarity. Therefore, we examined the effects of mAb on L1-mediated signaling in more detail. We observed that the incubation of OVMz cells with mAb to L1 caused a time-dependent loss of Src and Erk-activation (Figure 63A). Similar results were noted in the ovarian carcinoma cell line SKOV3ip (Figure 63B).

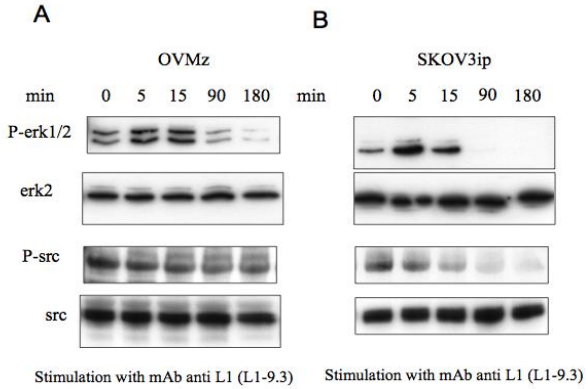

Figure 63: (A) Cells were incubated with mAb L1-9.3 (10mg/ml) for the indicated length of time. They were lysed in the presence of phosphatase inhibitors and analyzed by Western blotting with the indicated antibodies to phospho-Erk (p-Erk) and Phospho-Src (P-Src). Equal loading of the lanes was controlled using antibodies to the respective none-phosphorylated proteins.

To analyze whether the effects of the L1-mAb were transient or long lasting, we incubated SKOV3ip cells for 24 h. In addition to the novel mAb L1-9.3, we included the L1-mAbs L1-11A, L1-14.10 and L1-38.12. The mAbs L1-11A, L1-14.10 and L1-9.3 efficiently blocked Erk-phosphorylation *in vitro* (Figure 64A). There was no inhibition with isotype matched control antibody or the mAb L1-38.12 that binds only the neural isoform but not the tumour isoform of L1. Fluorescent analysis with the phospho-specific Erk antibody confirmed a clear reduction of activated Erk in L1-mAb treated cells (Figure 64B).

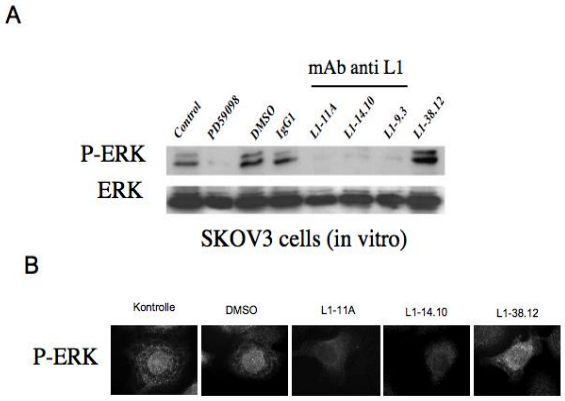

Figure 64: (A) Sustained suppression of Erk-phosphorylation achieved by L1-mAbs in SKOV3ip cells. The cells were incubated for 24 h at 37°C with the indicated purified antibodies to L1 (10 mg/ml) or isotype control IgG. The mAb L1-38.12 recognizes only the neural form of human L1 but not the tumour form. Cells were also treated with DMSO (vehicle), or the Erk-specific inhibitor PD98059. Cell lysates were examined for phosphorylation of Erk. (B) Fluorescent staining of treated cells with a phospho-Erk specific antibody.

Effects of L1-mAb on gene expression

We next examined whether L1-mAb affected the gene expression profile of SKOV3ip cells. Therefore, cells were treated for 96 h with L1-mAb and analyzed by qRT-PCR analysis. Indeed, cells treated with L1-11A versus control antibody showed significant changes in the expression of L1-regulated genes. Whereas the L1-mAb treatment reduced the expression of HOXA9, and β3-integrin, the expression of CRABPII, IER3 and STK39 were enhanced. Thus, the L1-mAb treatment reverted the effects of L1-mediated overexpressing cells (Figure 65B).

We argued that the depletion of L1 by siRNA might induce similar effects than the treatment with L1-mAb. To answer the question, we transiently depleted L1 by siRNA and examined Erk-activation and the expression of our predefined gene set. The L1 knock-down completely abrogated L1 expression (decrease by 90%). At the same time, the levels of phopshorylated Src and Erk were reduced (not shown). Strikingly, the siRNA mediated L1 knock-down caused similar changes in the expression levels of genes as the treatment with L1-mAb (Figure 65A).

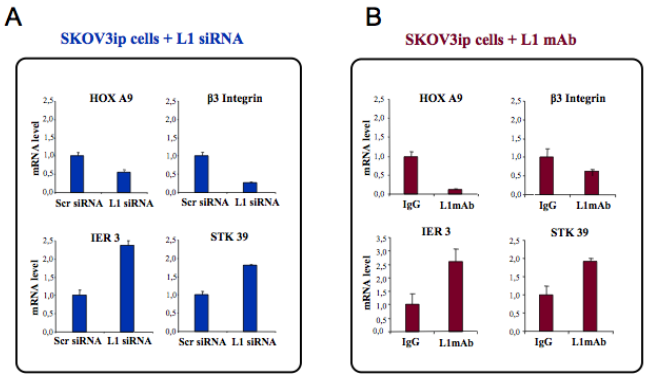

Figure 65: (A) Depletion of L1 by L1-specific siRNA. SKOV3ip cells were transfected with L1-specific siRNA or scrambled control oligos and analyzed 72 h later. Cell lysates were examined for L1 depletion (decrease by 90%). The siRNA transfected SKOV3ip cells were analyzed by qRT-PCR for the expression of the indicated genes. (B) SKOV3ip cells were incubated in the presence of mAb L1-11A or isotype-matched control antibody for 96 h. The mRNA was transcribed to cDNA and analyzed by qRT-PCR for the expression of the indicated genes.

Effects of L1-mAbs on tumour growth and gene expression in vivo

Having established that L1-mAbs could interfere with Erk-phosphorylation, we analyzed the capacity of novel L1-mAbs in functional assays. All mAbs to L1 blocked the invasion of SKOV3ip cells in matrigel *in vitro*. We also observed a partial inhibition of the growth of SKOV3ip cells in nude mice reconfirming our previous data (Arlt *et al*., 2006).

In an independent experiment we tested whether L1-mAb had influenced the gene expression of SKVO3ip cell *in vivo* in a similar fashion as *in vitro.* mRNA from the residual tumour of mAb L1-9.3 treated mice or control mice were isolated and subjected to qRT-PCR analysis. L1-mAb treatment led to significant reduction of the tumour mass (minus 60%) (Figure 66A) and to the down-regulation of L1-dependent genes as demonstrated for HOXA9, β3-integrin and IER3 (Figure 66B).

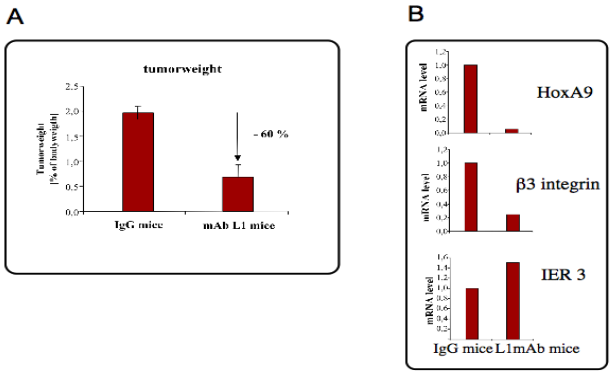

Figure 66: (A) SKO3ip tumour bearing animals were treated with mAb L1-9.3 leading to a substantial reduction of tumour volume. (B) mRNAs from residual tumours or control tumours were isolated, transcribed to cDNA and analyzed by qPCR for the expression of the indicated genes.

Based on our results, we propose that loss of the TS-motif in the L1 cytoplasmic part reduces sustained activation of Erk and prevents the expression of Erk-dependent genes. The same effects are observed after treatment with L1-mAbs. Although the mechanistic details have still to be elucidated, this offers the possibility to target L1 in human carcinomas. The inactivation of L1 by mAbs or over-expression of the hL1mutTS might be novel routes for blocking the growth and dissemination of tumours.

The role of the RGD integrin binding site in human L1-CAM

L1 can was shown to support cell migration and invasion and can promote gene regulation in HEK293 and other carcinoma cells. It is not known whether L1-signaling requires ligand binding. The RGD motif in the sixth Ig domain of L1 is a binding site for integrins. The role of RGD in L1-signaling using site directed mutagenesis combined with antibody blocking studies was studied.

It is conceivable that L1 expressing tumor cells interact with integrins on neighbouring tumor cells or stroma cells in the surrounding tissue. Contact to neighboring tumor cells could for example favour bidirectional signaling via L1 and integrins as the same cell types often express both binding partners. In order to address these questions we have analyzed closer the role of L1-RGDs for L1 signaling using site-directed mutagenesis and antibody blocking experiments. We observed that L1-RGE expressing HEK293 cells showed reduced cell-cell binding, cell motility, and invasiveness (Figure 67) and tumor growth in NOD/SCID mice (Figure 68).

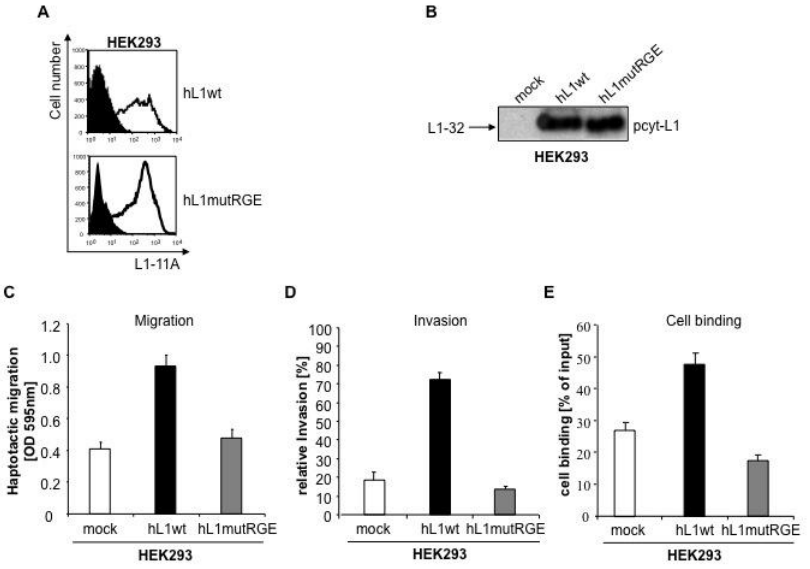

Figure 67: (A) Characterization of transfected HEK293 by FACS analysis. The indicated cells were stained with mAb L1-11A to the L1 ectodomain followed by PE-conjugated rabbit anti mouse IgG and analyzed by FACS. Staining with the secondary antibody only is shown for control (dark curve). (B) Analysis of haptotactic cell migration. Fibronectin was used as substrate and coated onto the backside of Transwell chambers. After 16 h the transmigrated cells at the backside of the filter were stained with cristalviolet solution. The eluted dye was measured at 595 nm in an ELISA reader. (C) Analysis of matrigel invasion. Cells were seeded into a 4-well plate and allowed to invade into matrigel using a double filter assay. After 22 h the invaded cells adhering to the top of the second membrane were counted after staining with DAPI. (D) Analysis of cell-cell binding. The indicated cells were allowed to adhere to monolayers of CHO cells at 37°C and the percentage of cell binding was determined by counting the non-bound fraction.

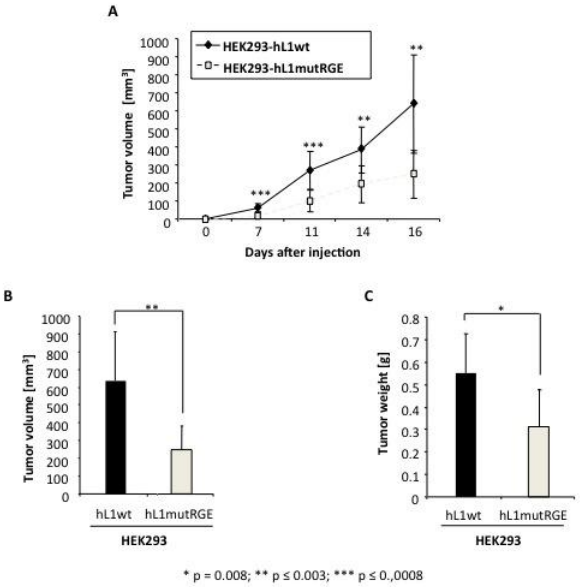

Figure 68: Analysis of tumor growth in NOD/SCID mice (A) Stably transfected HEK293 cells were injected into the left or right flanks of 6-week-old NOD/SCID mice, respectively. Tumor growth was monitored for 16 days, at which point the experiment was terminated. Results shown represent mean tumor volume ± SD for n = 8 animals. The tumor weight was determined after sacrificing the tumor bearing animals. (B and C) The statistical analysis was carried out on the basis of tumor volume or tumor weight.

We found that the RGE-mutation impaired L1-dependent gene regulation and antibodies to avb5 integrin had similar effects (Figue 66). Mutant L1 was unable to translocate to the nucleus. Our findings highlight the importance of the RGD site in L1 for human tumors and suggests that nuclear signaling of L1 is dependent on integrins.

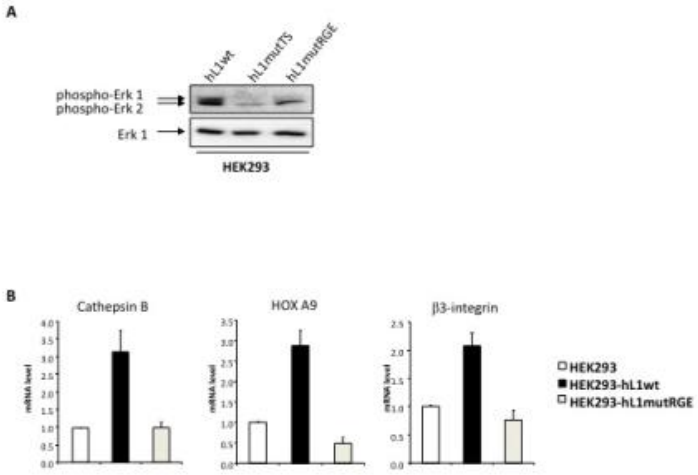

Figure 66. Analysis of erk activation and L1-dependent gene regulation. (A) Phosphorylation of Erk was analyzed in lysates from cells grown in 10% FCS. Not that HEK293-mutTS cells were used as an internal control as these cells are impaired in ERK-activation. (B) The expression levels of selected genes were analyzed in the indicated cells by qRT-PCR. The mRNAs were isolated. transcribed to cDNA and used as template. The investigated target genes were selected on the basis of our previous work.

To further explore the role of soluble L1, we have constructed cell lines expressing either L1-fulllength at the cell surface (L1-FL), the L1-ectodomain that is secreted into the medium (L1-ecto) or the cytoplasmic remnant that is leaved behind after cleavage (L1cyt). The L1-constructs were retrovirally transduced into the L1-negative ovarian carcinoma cell line m130. Figure 70A-D shows the characterization of the established cell lines. All constructs expressed the functional L1 fragments well. Treatment with PMA, to induce L1 cleavage, augmented slightly the amount of soluble L1 in the medium of L1-FL expressing cells. The amount of cleaved L1 was much smaller than the secreted L1-ectodomain in L1-ecto expressing m130 cells (Figure 70C).

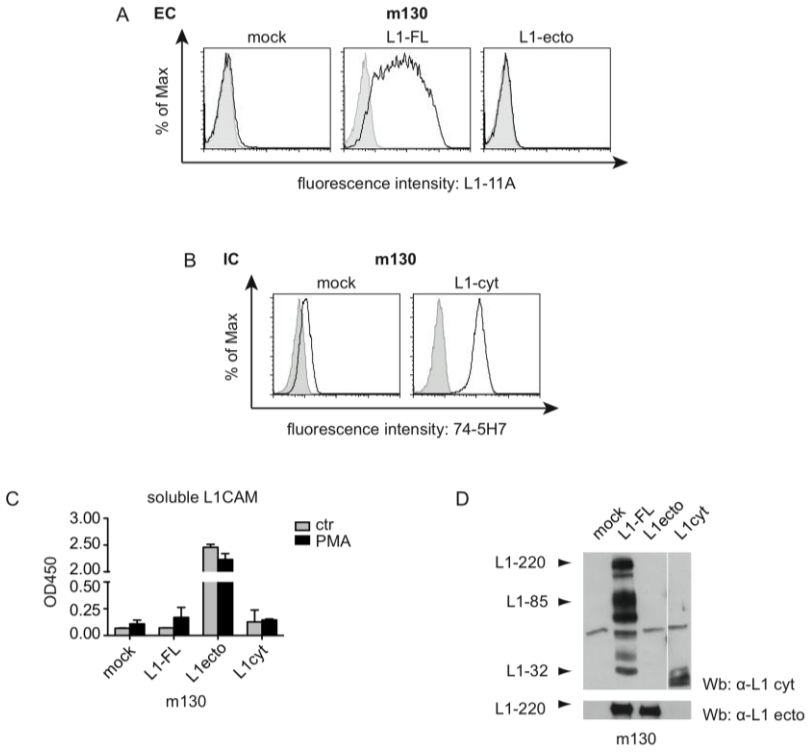

Figure 70. (A) Cytofluorographic analysis of m130 cells expression mock (empty vector), L1-FL or L1-ecto using mAb L1-11A to the ectodomain of L1. (B) Cytofluorographic analysis of m130 cells expression mock (empty vector) or L1-cyt using mAb 74-7H7 to the cytoplasmic part of L1 after cell permeabilization. (C) Shedding of L1-FL but not L1-ecto is augmented after PMA treatment. Note the large amounts of soluble L1 in m130 L1-ecto cells. (D) Detection of L1 by Western blot using natibodies to the L1 Ectodoamin (mAb L1-11A) or cytoplasmic part (pcytL1). Note the various L1 cleavage fragments L1-220 (fulllenght), L1-85 and L1-32.

Evaluation of L1-based therapy in NOD/Scid mice

Objective is to investigate whether L1 might be a novel target for antibody-based therapy using in vitro studies and a xenograft mouse model for human ovarian carcinoma.

We observed that antibodies to L1 could efficiently block cell proliferation in vitro (Figure 71) and could inhibit the matrigel invasion of two ovarian carcinoma cell lines OVMz and SKOV3 (Figure 71B). As SKOV3 cells form tumors with a dissemination pattern similar to human ovarian carcinoma cells *in situ*, we applied antibody treatment to CD1 nu/nu mice carrying the human xenograft. As shown in Figure 71C, the antibody treatment with mAb L1-11A significantly reduced the tumor load and the volume of ascites during the treatment period.

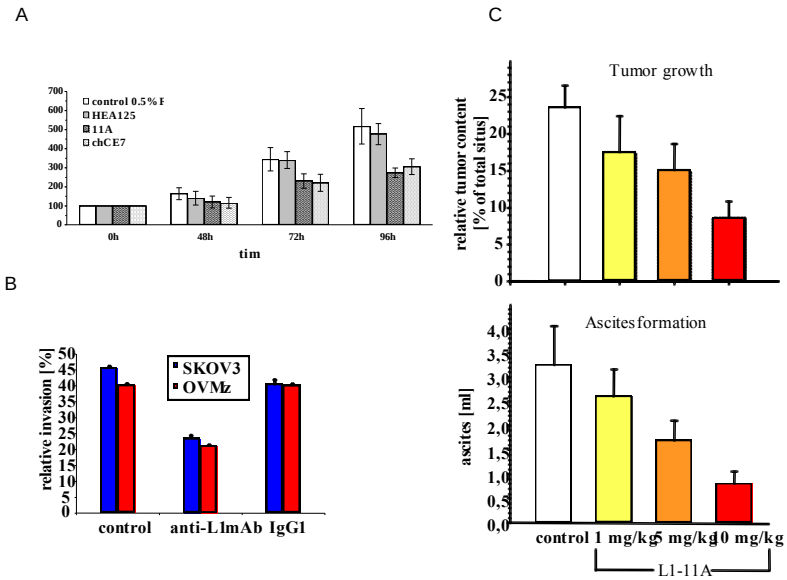

Figure 71: L1-antibody based therapy of ovarian carcinoma. A) SKOV3 cells were incubated in the presence or absence of mAb to L1 (L1-11A or ChCE7) or the EpCAM-specific mAb HEA125. Cell proliferation was determined at the indicated time points by the MTT assay. B) Matrigel invasion assay. The ovarian carcinoma cell lines SKOV3 or OVMz were allowed to invade into matrigel in the presence of mAb to L1 or isotype control mAb. Note that both cell lines were partially blocked in matrigel invasion. C) SKOV3 ($7x10^6$cell) were marked with a LacZ reporter gene and injected into CD1 nu/nu mice. After 2 days L1 mAb L1-11A or an isotype matched control mAb was injected twice a week i.p at the indicated amount. After 35 days the animals were sacrificed and tumor volume and ascites were measured. Note that mAb to L1 significantly reduced both tumor volume and ascites.

We have demonstrated that antibodies to L1 can have therapeutic potential and can reduce cell proliferation *in vitro* and *in vivo* growth of SKOV3ip human ovarian carcinoma cells in a xenograft mouse model (Primiano *et al*., 2003; Arlt *et al*., 2006, Knogler *et al*., 2007). Thus, a better understanding of L1 signaling in carcinoma cells and the mode of action of L1 antibodies is needed.

We have developed and characterized novel L1 mAbs and have begun to evaluate the therapeutic potential. Figure 72A shows some of the novel antibodies to L1 (mAb L1-14.10, mAb L1-9.3) that can block the matrigel invasion of SKOV3ip cells to a similar extend as the established mAb L1-11A. Mab L1-9.3 was superior in the inhibition of tumour growth of SKOV3ip cells in nude mice (Figure 72B).

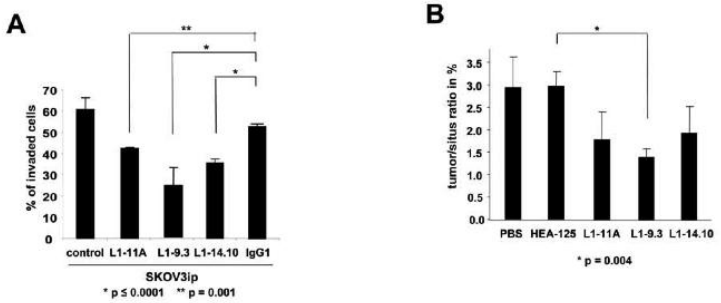

Figure 72: (A) SKOV3ip cells in the presence of the indicated antibodies (10 mg/ml) were examined in a matrigel invasion assay. (B) Tumour growth in nude mice. LacZ-tagged SKOV3ip cells were injected i.p. into nude mice and after tumour implantation animals were treated with the indicated L1-mAbs or control mAb to EpCAM (HEA-125). After 30 days the tumour volume was determined and is given as the ratio between X-Gal stained tumour mass and the total sinus. 6 animals were analyzed per group.

Therapy monitoring using luciferase labeled cells

In previous studies, we used retroviral ß-galactosidase labelling and X-Gal staining of tumour cells to quantify the tumour volume and the therapeutic effect of applied antibodies. We have now introduced luciferase labelling to allow real-time monitoring of tumour growth. Figure 73 gives an example of growth monitoring of luciferase-labeled SKOV3ip cells grown subcutanously.

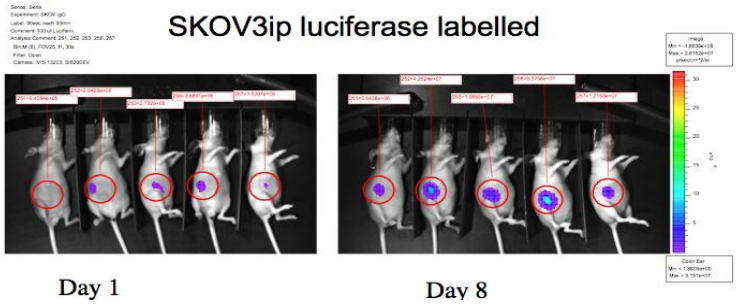

Figure 73: (A) SKOV3ip cells were stably transduced with luciferase. Tumour cells were injected s.c. into nude mice and tumour take was monitored on day 1. Imaging on day 8 shows progressive tumour growth of SKO3ip tumour.

Generation of isotype switch variants of L1 mAb 9.3

To demonstrate that L1 mAb of the IgG-2a isotype gave better therapeutic effects compared to IgG1 mAb was not due to a difference in the antibody variable portions but was indeed mediated by the Fc part of the mAb, we carry out isotype switching of mAb L1-9.3 (IgG1). We used cell sorting of rare isotype switch variants that occur spontaneously due to recombination of the antibody locus. Hybridoma cells were confirmed to be isotype specific antibodes to mouse IgG-2a. Sorted cells were grown up and expanded for a second round of cell sorter selection using antibodies to mouse IgG-2b. Hybridoma cells producing all three isotyes variants of mAb 9.3 were obtained. All isotype variants had retained a similar binding affinity for human L1 .

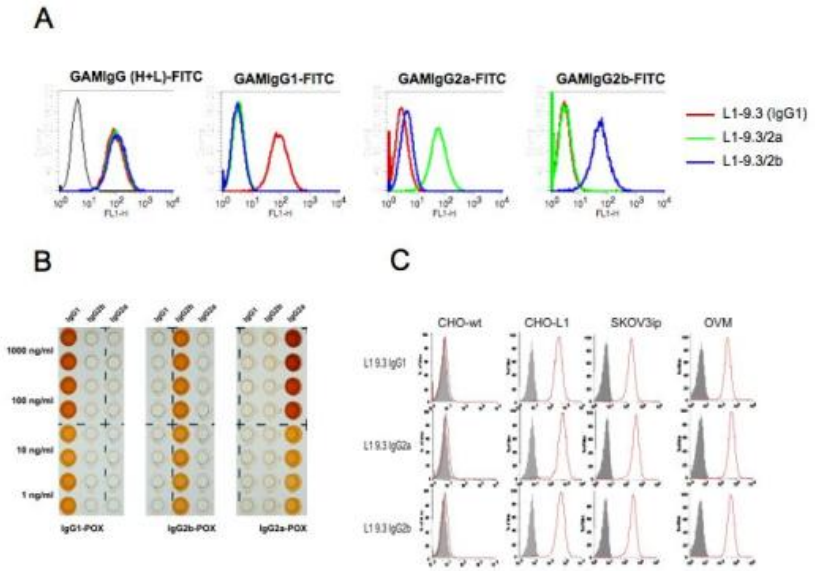

Figure 74: (A) mAb 9.3 hybridoma cells were isotype switched by cell sorter technology. Two variants of the initial IgG1 antibody (2a and 2b) were isolated. Cytofluorographic analysis of SKOV3ip cells with the three isotypes revealed staining with antibodies specific for the respective isotype. (B) Determination of isotype by ELISA. Purifed isotype mAbs were purfied and coated in decreasing amounts to ELISA plates. (C) The indicated cells were stained with the L1-9.3 isotype variants and analyzed by cytofluorographic analysis.

Humanized and chimerized antibodies to human L1

Because of its superior biophysical characteristics (high Kd and low off rate), we used mAb 9.3 as a developmental candidate. We constructed chimerized and fully humanized IgG1 antibodies in collaboration with Dr. G. Moldenhauer and a pharmaceutical company (Medigene Inc., Munich) (Figure 75).

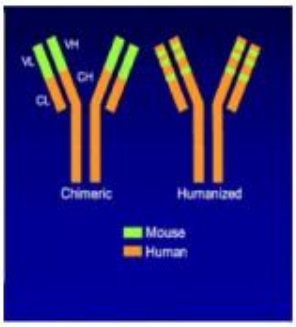

Figure 75: Schematic summary of Abs to human L1. Chimerized Ab Chi L1 9.3 is produced in mouse hybridoma cells. Fc part: human IgG1, Fv part: mouse (L1-9.3). Hu3 and Hu4 are two different formats of the human IgG1Humanized Abs produced by CHO or human B-cell line. Fc part is human IgG1, while Fv part is human except of CDR region (Mouse L1-9.3).

We next examined whether the chimerization or humanization had altered the binding ability of the 9.3 mAb. The binding to cells was not altered and the binding constants as determined by Biacor analysis on purified L1-Fc was not changed (Figure 76).

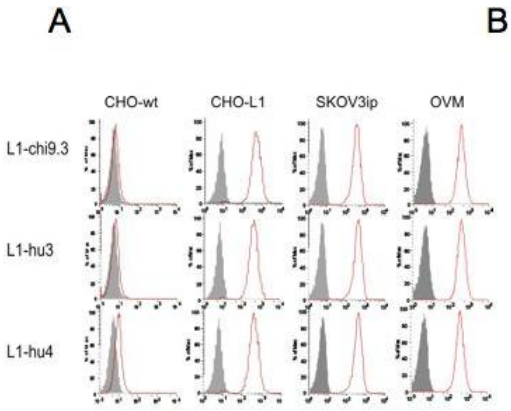

Antibody	ka (1/Ms)	kd (1/s)	KD (M)
L1-9.3 hu3	1,10E+06	6,50E-05	5,90E-11
chi L1-9.3	3,30E+05	2,20E-05	6,70E-11
L1-9.3	2,60E+05	2,20E-05	8,50E-11

Figure 76: Binding of chimerized and fully humanized Abs to human L1.

Effects of humanized L1-mAbs on tumor growth

Having established that humanized L1-mAbs were not altered in binding characteristics we tested the antibodies in the SKOV3ip therapy model using luciferase labelled cells and imaging. Figure 77 shows a representative example and demonstrates that both the humanized and chimerized antibodies were effective in reducing the tumor volume.

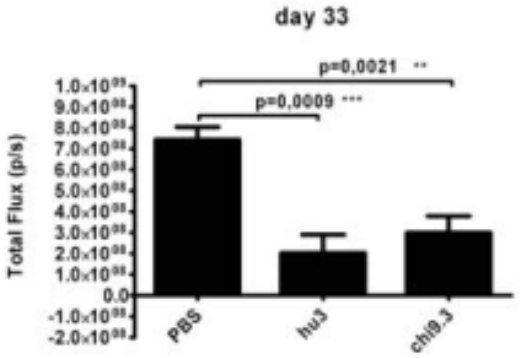

Figure 77: (A) SKOV3ip cells were stably transduced with luciferase. Tumor cells were injected i.p. into CD1 nude mice and mAb therapy (10 mg/kg bodyweight. 3 times weekly) was started 2 days later. Imaging on day 33 showed reduced tumor growth of SKO3ip tumors.

Humanized L1-mAbs exert ADCC (antibody-dependent cellular cytotoxicity)

Most antibodies used for human tumor therapy are human IgG1 and ADCC is an important component of the therapy effect. We have shown that mAb L1 therapy recruited inflammatory cells to the tumor site. The finding that L1 mAbs therapy effects were clearly dependent on the isotype also suggested an important contribution of Fc-receptor bearing host cells. To investigated whether L1 mAb were able to support ADCC we used human PBLs as effector cells in a calcein release assay. As target cells we used SKOv3ip cells or SKBR3 human breast carcinoma cells. Both target cell lines express Her-2 as well as L1CAM. Significant ADCC was only seen when the L1 mAb were produced in human Namalwa cells and not in CHO cells. It is quite known that the addition of excessive fucose in the glycans of mAbs can inhibit ADCC which seems to be the case in CHO cells. Our results suggest that humanized L1 mAb can excert ADCC just in the same way as the Herceptin Ab used for control (Figure 78).

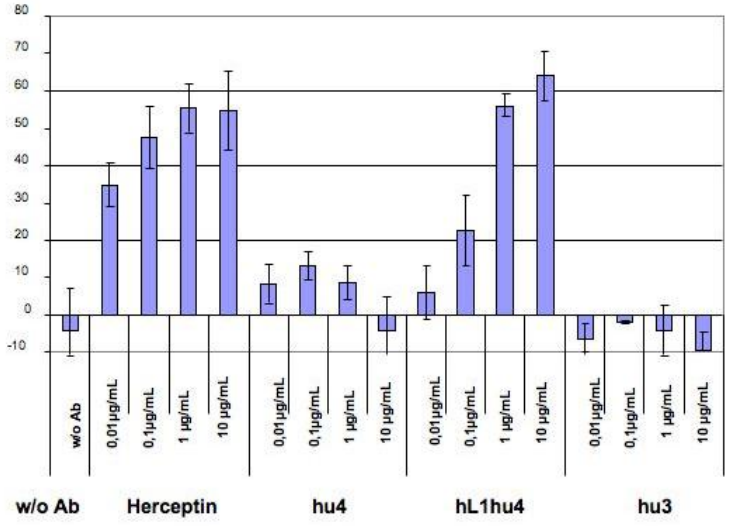

Figure 78: ADCC dependent lysis of SKBR3 cells by Herceptin and L1 mAb. Note that Hu3 and hu4 are produced in CHO cells (insufficient glycosylation) whereas hL1hu4 was produced in human Namalwa cells.

(8) Development of an effective method for the enrichment and isolation of circulating tumor cells from blood

Partner 10 led by Viktoria Weber has developed a new technology for the enrichment and isolation of circulating tumor cells from a large blood volume. The process comprises pre-enrichment of CTCs by leukapheresis and elutriation and subsequent isolation of the CTCs from the pre-enriched cell fraction with either fluorescence activated cell sorting (FACS) or immunomagnetic bead adsorption. Elutriation and FACS are both semi-automated systems in need of little material handling minimizing the inherent variability of the process. The applicability of the three step process: leukapheresis - elutriation - FACS/adsorption was investigated in a proof of concept study using leukapheresates from healthy donors which were spiked with cells from the tumor cell line CaOV-3 at a ratio of 26 CTCs per 106 peripheral blood mononuclear cells. The combination of elutriation and FACS was equivalent to or outperformed state-of-the-art techniques with respect to the enrichment, recovery, and purity of isolated tumor cells at the given spike ratio. When combined with leukapheresis, the described process has at least a 500fold greater capacity expected to increase CTC yield and incidence. Tumor cells and leukocytes isolated by the three-step process were also found to be viable and easily identified and distinguished using cytometric and nucleic acid based techniques. Isolation of CTCs from the last elutriation fraction by immunomagnetic bead adsorption using microparticles functionalized with anti-EpCAM antibodies was associated with lower recovery and purity of the isolated circulating tumor cells. In addition, it was demonstrated that suspensions of magnetic (micro)particles are superior for the isolation of circulating tumor cells as compared to conventional adsorbent columns, which are associated with high unspecific cell retention due to trapping of cells between the adsorbent particles. All deliverables and milestones of the project were met; however, regarding the isolation of CTCs, the focus was shifted from adsorbent columns to either suspensions of adsorbent microparticles or fluorescence-activated cell sorting.

Next, the three-step process developed in this project should be further evaluated using patient samples instead of cell lines and subjected to direct comparative studies with leading CTC enrichment technologies. An increase in CTC yield and incidence is anticipated to improve the diagnostic utility of CTCs facilitating the early detection of metastasis and monitoring of therapeutic benefit. The high yield of CTCs obtained with this procedure would allow for robust molecular analysis of isolated CTCs, increasing the potential to identify and investigate new therapeutic targets, and to develop an in vitro metastatic disease model.

Development of specific adsorbents for circulating tumor cells

For the development of specific adsorbents for circulating tumor cells, polymer beads are functionalized with antibodies against surface molecules of the tumor cells. Basically, there are two approaches, namely (a) the use of adsorbent columns containing particles in a size range of several hundred micrometers, or the use of magnetic microparticles functionalized with specific antibodies. Both approaches were followed in parallel. In this reporting period, experiments were performed in order to compare the efficacy of the two approaches.

Large adsorbent particles (particle size about 100 to 150 µm)

Given the low abundance of circulating tumor cells among other blood cells, it is prerequisite that polymers used for functionalization with antibodies exhibit low unspecific binding of cells. In previous screening tests summarized in earlier reports, it was demonstrated that Tentagels as well as Sepharose beads are suited for this purpose and show low unspecific cell binding. The structure of Tentagels is shown in Figure 79.

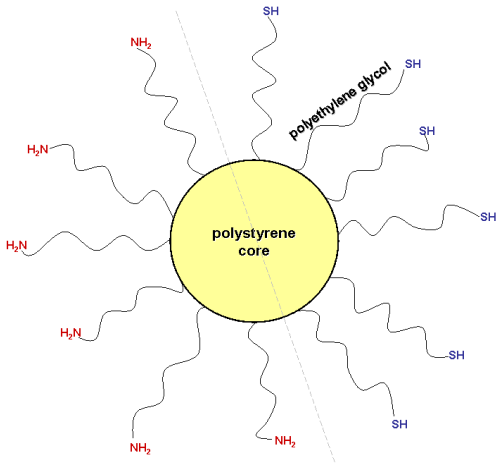

Figure 79: Basic structure of Tentagels, containing either terminal amine or thiol groups for further activation and functionalization.

Tentagel beads (Tentagel-NH_2) were obtained from Rapp Polymers, Germany. The amine group content was determined by reaction of the beads with excess phenylisothiocyanate (PITC) and determination of free PITC after the reaction by HPLC. On average, Tentagels were found to contain 0.26 mmol of terminal amine groups per g dry adsorbent. Beads were activated with glutaraldehyde (1.5 g of dry beads reacted with 5 mL of 0.5% glutaraldehyde in 0.1 M sodium phosphate buffer, pH 7.6). Under these conditions, about 50% of the terminal amine groups were reacted to aldehyde groups. The activated beads were functionalized with anti-EpCAM antibodies using 100 µg of monoclonal anti-EpCAM antibody per 0.5 mL of activated Tentagels. For comparison, Protein A Sepharose 6 MB (bead size 250 to 350 µm) was coupled with anti-EpCAM antibodies using the same ratio of antibody to beads. The functionalized beads were used to bind CaOV-3 cells using 10^6 cells per 100 µL beads for 30 min. Unbound cells and beads were separated using Bio Micro Spin chromatography columns (BioRad). The number of bound cells was calculated from the number of cells in the supernatant before and after adsorption. Blank experiments were conducted using Tentagels or Sepharose beads without immobilized antibody to compensate for unspecific trapping of cells between the adsorbent particles.

Functionalized magnetic microparticles (particle size 3 µm)

Two different products were used, namely CELLection Epithelial Enrich beads or tosyl activated Dynabeads fuctionalized with anti-EpCAM antibodies (both from Dynal Invitrogen). CELLection beads contain anti-EpCAM antibody immobilized on the beads via a DNA linker. For tumor cell capture, $4x10^7$ beads were incubated with

10^6 CaOV cells for 30 min. Subsequently, beads with captured tumor cells were separated using a magnet and the amount of captured cells was calculated from the difference of cells in the supernatant before and after addition of magnetic microparticles. The results are summarized in Table 38 and Table 39.

Table 38: Comparison of glutaraldehyde activated TentaGels and Protein A Sepharose beads examined for their tumor cell capture capability

Adsorbent	µg mAb bound/ml ads.	pmol mAb bound/ml ads.	TC bound/ml ads.	% bound tumor cells of initial cell number
TentaGels S-NH_2 0.5% glutaraldehyde activated	below detection	below detection	8,95 x 10^5	8
Protein A Sepharose 6MB	56,6	377	1,14 x 10^6	10

* The cell capture experiments were carried out by applying 1x10^6 cells to 100µl of wet adsorbent.

Table 39: Capture efficiency of magnetic beads regarding tumor cell immobilization

Magnetic Beads	µg mAb bound/ml ads.	pmol mAb bound/ml ads.	TC bound/ml ads.	% bound tumor cells of initial cell number	Number of beads/TC
CELLection epithelial enrich. magn. beads	not indicated	not indicated	4,6 x 10^8	91	43
Tosyl activated, anti-EpCAM coupled magn. beads	1332	8880	5,4 x 10^8	98	39

* For the cell binding experiments 1x10^6 cells were incubated with 4 x 10^7 magnetic particles.

The results demonstrate that considerably higher amounts of antibody can be immobilized on a given adsorbent volume if microparticles (3 µm as compared to 200-300 µm for conventional beads) are used, resulting in significantly increased efficiency for the capture of tumor cells. When Tentagels were activated with a higher concentration of glutaraldehyde (7% instead of 0.5%), this did not significantly increase the tumor cell binding (data not shown). Another big advantage of the use of magnetic particles is that they can be easily separated from the tumor cell suspension, which avoids trapping of cells between the beads and thus minimizes unspecific cell loss.

Development of a system for the enrichment of circulating tumor cells

A proof of concept study for the enrichment and isolation of CTCs from a large blood volume was conducted and completed in the last reporting period. The enrichment and isolation procedure consisted of the following steps: pre-enrichment of white blood cells from healthy donors by leukapheresis, further fractionation of the leukapheresis product (spiked with tumor cells) by counter-flow centrifugal elutriation, and isolation of the tumor cells by either fluorescence activated cell sorting or immunomagnetic bead adsorption. (Figure 80).

Technical systems

Leukapheresis is a density centrifugation system used to harvest peripheral blood stem cells and mononuclear cells for therapeutic purposes by circulating the total blood volume of a patient up to three times. This system has been used without complication for patients with advanced disease stage and age receiving autologous transplantation of CD34 positive cells or mobilized dendritic cells for immunotherapeutic purposes following high dose chemotherapy (Chou *et al.* Breast Cancer 2005; 12:178-88; Mazzolini *et al.* J Clin Oncol 2005; 23:999-1010). In addition, the presence of circulating tumor cells within leukapheresate products obtained from metastatic cancer patients has previously been confirmed (Ferrucci *et al.*, Int J Oncology 2007; 30: 955-962., Franklin *et al*. Transplantation 1999; 94: 340-47). Elutriation following leukapheresis has been used to separate leukocytes based primarily on their size to enrich and purify monocytes for dendritic cell tumor immunotherapy (Berger *et al.*, J Immunol Methods 2005; 298: 61-72). Circulating tumor cells contained in a leukocyte population are expected to be elutriated with monocytes due to their large size and similar density, simplifying their subsequent detection and isolation. Final enrichment and isolation of tumor cells was performed using fluorescence-activated cell sorting (FACS), which was compared against immunomagnetic bead adsorption. FACS was chosen as a high throughput system that permits simultaneous detection and sorting using multiple markers to eliminate leukocytes and isolate viable circulating tumor cells with high purity.

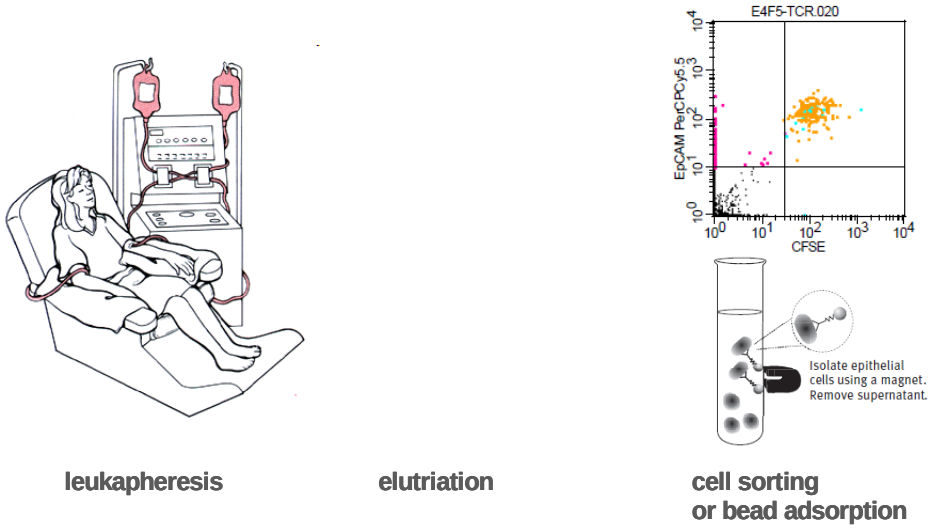

Figure 80. Enrichment system for circulating tumor cells. CTCs are collected and enriched from whole blood using three distinct semi-automated processes: (1) leukapheresis, (2) elutriation and (3) binding to magnetic beads functionalized with anti-EpCAM antibodies or fluorescence-activated cell sorting.

Leukapheresis

Leukapheresis was performed using the COBE Spectra system (Caridian BCT, Lakewood, CO), software version 6.1, programmed to collect peripheral blood stem cells within enriched peripheral blood mononuclear cells from healthy donors. The donation of leukapheresate products from healthy male donors, age 20-50, was

approved by the Medical University of Vienna Ethics Commission. 10 liters of blood were circulated to harvest greater than 10^9 monocytes and $5x10^9$ to $30x10^9$ leukocytes. A pre- and post-leukapheresis blood cell count was determined. After collection, the leukapheresate was stored overnight with shaking (22ºC, 50-60Hz). Leukapheresis successfully harvested 94% of total blood volume PBMCs equal to on average $14x10^9$ PBMCs concentrated in 90% platelet depleted plasma. Of the PBMCs, 80% were lymphocytes and 16% monocytes. The reduction of granulocytes resulted in approximately 2-fold enrichment of monocytes. The leukapheresate also contained $14x10^{10}$ platelets and $26.5x10^9$ red blood cells (99.9% reduction from blood). The leukocyte composition of the leukapheresate is summarized in Table 40.

Prior to elutriation, the leukapheresate was spiked with ovarian epithelial CaOV-3 tumor cells. CaOV-3 cells were observed to have a diameter of 15.9 to 34.7 µm consistent with what has been observed for other epithelial tumor cell lines from various cancers. The spiking procedure was performed as described in previous reports. A ratio of 2.6 (n=1) or 26 (n=6) tumor cells per $1x10^6$ PBMCs was used.

Elutriation

This step was used to separate the tumor cell spiked leukapheresates into 5 or 6 distinct fractions with smaller cells being elutriated first at lower counter fluid flow rates. The process was carried out as described in previous reports using the Elutra® elutriation system (Caridian BCT). Experimental work on the enrichment of circulating tumor cells was performed at the Department for Transfusion Medicine, Medical University of Vienna, under the supervision of Prof. M.B. Fischer.
Flow cytometry was performed as described in earlier reports to determine the tumor cell distribution within the leukapheresate and elutriation fractions 2-6. Tumor cells were classified as CFSE+/EpCAM+/CD45-, and each event was morphologically confirmed within the forward scatter-side scatter dot plot (Figure 81). The leukocyte composition of the last elutriation fraction is given in Table 41 and the distribution of PBMCs and tumor cells during elutriation is shown in Figure 82. Platelets, the smallest blood cell component, were completely removed in the first elutriation fraction, and red blood cells were completely eliminated prior to the last fraction. In total, 97% of monocytes were recovered from the leukapheresate during elutriation, 77% of which were collected with 81% purity in the last elutriation fraction. This corresponds to 1.6 ± 0.6 billion monocytes enriched approximately 5-fold as compared to the leukapheresate in this fraction. Due to their large size the majority, 85 ± 15%, of tumor cells recovered by the elutriation process were contained in the last elutriation fraction along with enriched monocytes corresponding to a spiked tumor cell recovery of 66 ± 8% therein. No tumor cell events were observed in leukapheresate samples obtained prior to tumor cell spiking indicating a specificity of 100% for the flow cytometry detection method.

Leukapheresate

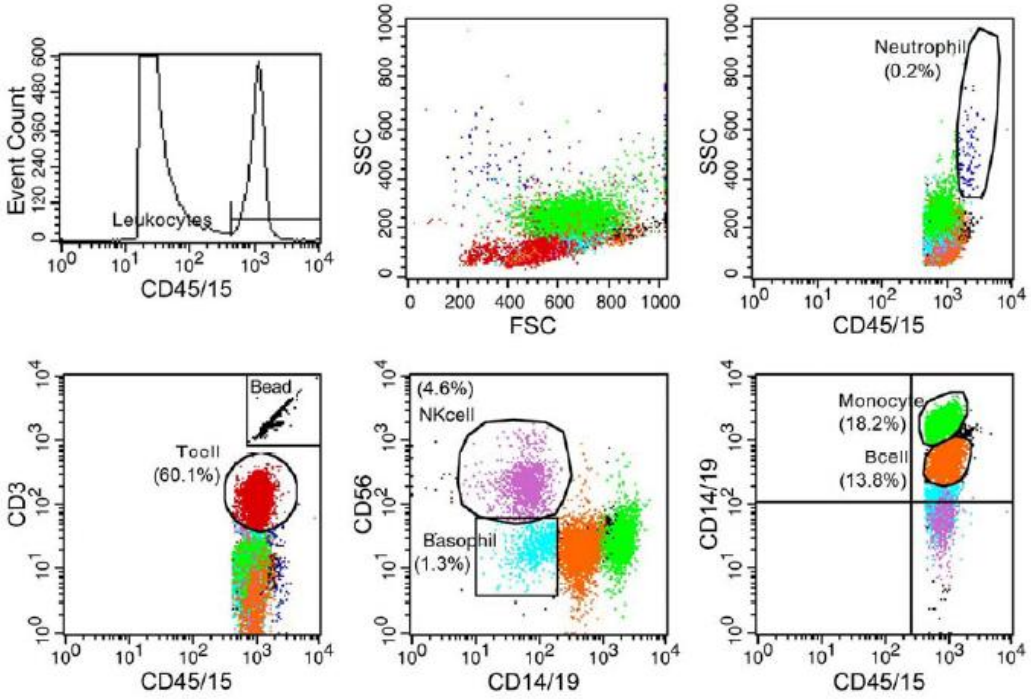

Elutriation Fraction 3

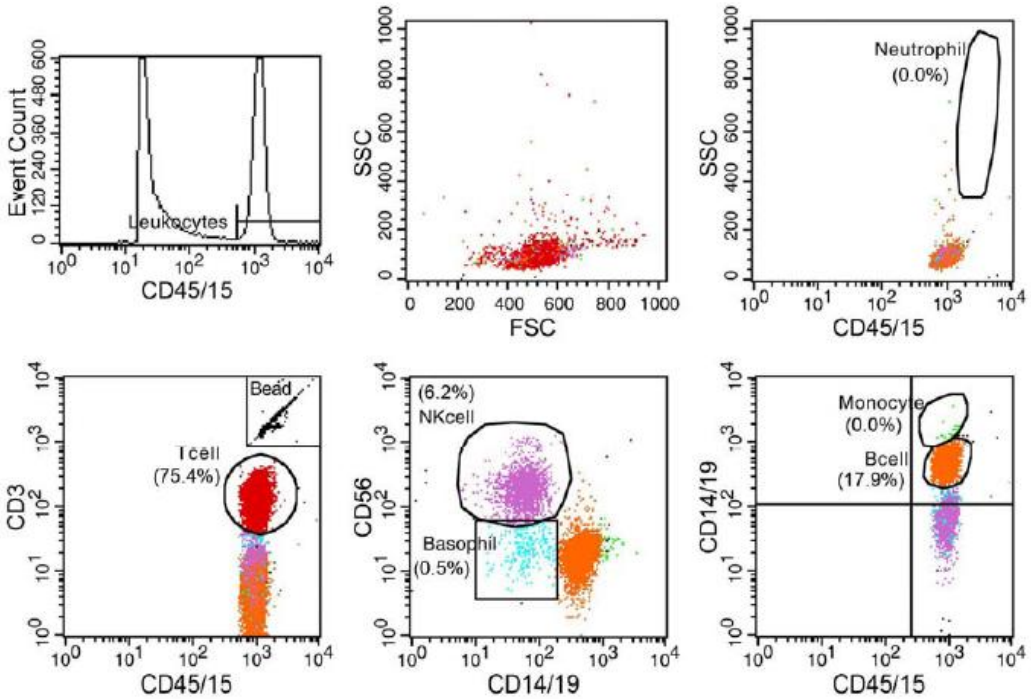

Figure WP6-3

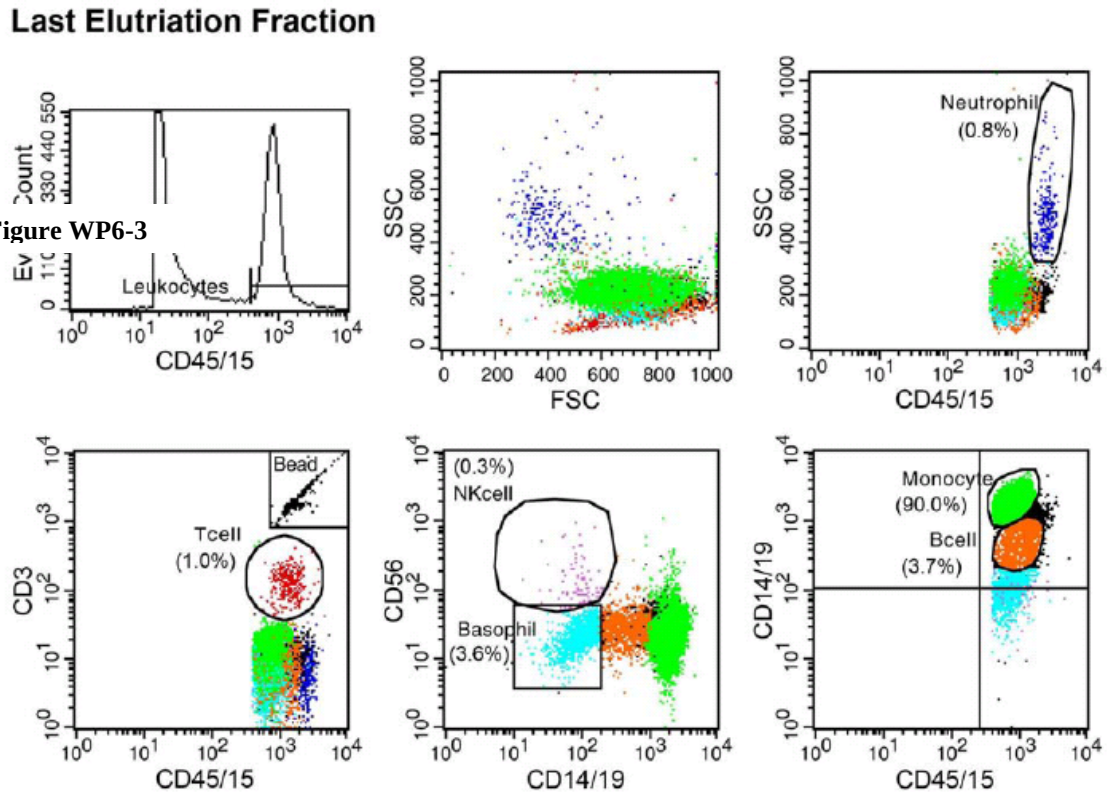

Figure 81: Leukocyte quantification by flow cytometry. Samples containing 105 leukocytes were obtained from the leukapheresate and elutriation fractions, placed in absolute count TruCount tubes, and labelled with an antibody cocktail containing anti-CD45, CD15, CD56, CD19, and Cd14. Flow cytometry was used to acquire 50,000 leukocyte events identified by CD45 expression. Cd45 positive events were then gated for analysis, and the leukocyte composition determined by specific antigen expression as follows: neutrophils (dark blue), by Cd15 of high granularity SSC, T-lymphocytes (red) by CD3, natural killer cells (violet) by CD56, B-lymphocytes (orange) by CD19, monocytes (green) by CD14 and basophils (light blue) by low granularity and negative expression of lymphocyte and monocyte specific antigens. Cells were quantified by multiplying their event number by the ratio of the total number of fluorescent beads contained in the TruCount tube to the number of beads acquired. The fluorescent beads are displayed in the upper right corner of the CD3 versus CD45/15 scatterplot, and for simplicity, they were gated and removed from the other plots. Representative histograms and scatterplots for the leukapheresate, fraction 3 and the last elutriation fraction from trial 10 are displayed.

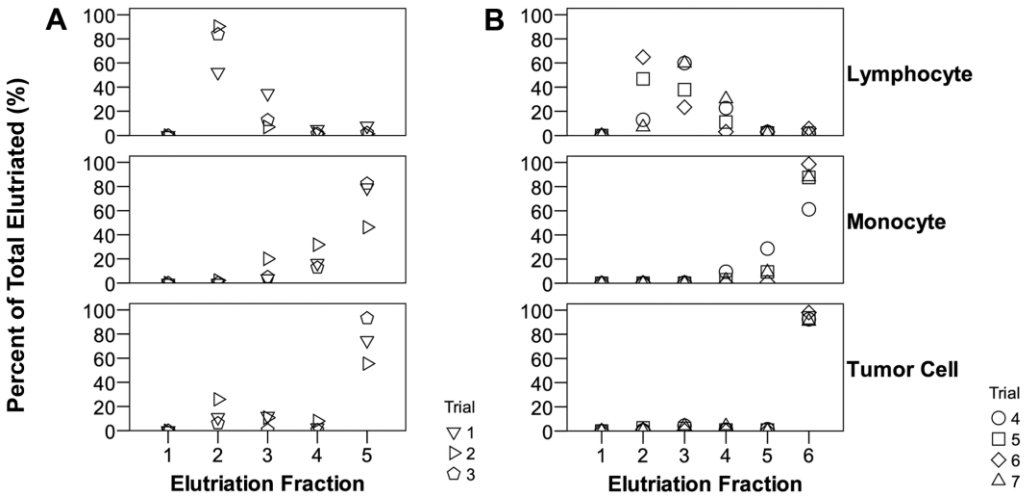

Figure 82: Distribution of lymphocytes, monocytes and tumor cells as a percentage of the total elutriated for each distinct population plotted against elutriation fraction number using the (A) default (trials 1-3) or (B) modified (trials 4-7) monocyte enrichment program.

Fluorescence activated cell sorting was used to isolate tumor cells from the last elutriation fraction (n=2). A total of 79,120,000 and 76,376,941 CD45 positive events were acquired yielding 1,272 and 3,301 CD45 negative and 4,889 and 7,948 CD45 positive sorted events after gating for intracellular CFSE and EpCAM expression. Thus, on average 20% of the spiked tumor cells were recovered in the CD45 negative group after FACS. Fluorescence microscopy indicated a tumor cell purity of 94.1% in the CD45 negative sorted samples and 25.5% in the CD45 positive sorted samples, and using this purity it can be estimated that 15% of the spiked tumor cells were recovered in the CD45 positive sorted group (Figure 83). The increased speed during sorting decreased the recovery of spiked tumor cells, and it may therefore be more efficient to use a lower speed and sort a decreased number of cells to provide a sensitivity of 75% and a tumor cell recovery of at least 50% after sorting. Immunomagnetic bead adsorption using EpCAM-immobilized beads resulted in lower recovery and a lower purity than FACS (numbers in parentheses, Table 42). For the experiments, aliquots of 10^7 PBMCs from fraction 2-6 were incubated with $4x10^7$ CELLection epithelial enrich beads (4.5µm diameter; Dynal-Invitrogen) in 600µl PBS 0.1% HSA for 30 min at 4ºC. Bead bound cells were separated from the suspension magnetically and subsequently eluted from the beads using DNAse-I and spun onto glass slides for immunofluorescent labelling and detection. Slides were blocked with goat serum prior to labelling with primary antibody (anti-EpCAM, anti-Her-2 [human epidermal growth factor receptor 2] and anti-EGFR [epidermal growth factor receptor), and secondary antibody (AF546 goat anti-mouse). Cells were fixed with 3% paraformaldehyde in PBS and permeabilized with 0.2% Triton X-100 in PBS. Intracellular labelling was performed with pan-cytokeratin-FITC antibody and Hoechst 33258 dye. Tumor cells were classified as cytokeratin+/Her-2, EGFR, EpCAM+/Hoechst+ events and morphologically confirmed by their large size, rounded appearance and high nuclear to cytoplasmic ratio.

Table 40. Leukocyte composition of the leukapheresate.

Trial	Leukocytes (10^9)	Neutrophils (10^7)	Basophils (10^7)	Lymphocytes (10^9)				Monocytes		
				NK cells	T cells	B cells	Total	Count (10^9)	Purity (%)	Enrichment
1	4,56	16,15	20,43	0,31	1,95	0,55	2,80	1,39	31%	3,4
2	19,75	3,45	69,33	0,69	12,65	2,34	15,68	3,34	17%	2,4
3	15,41	1,45	28,32	0,83	11,24	1,89	13,96	1,15	7%	1,4
4	14,35	3,90	59,82	1,02	7,54	2,62	11,18	2,53	18%	2,4
5	14,69	7,74	48,80	0,96	9,38	1,02	11,36	2,76	19%	2,3
6	11,10	27,06	33,65	0,47	6,75	1,21	8,43	2,06	18%	1,8
7	8,70	1,98	11,27	0,40	5,32	1,23	6,95	1,61	18%	2,1

Table 41. Leukocyte composition and monocyte isolation in the last elutriation fraction

Trial	Leukocytes (10^9)	Neutrophils (10^7)	Basophils (10^7)	Lymphocytes (10^9)				Monocytes			
				NK cells	T cells	B cells	Total	Count (10^9)	Purity (%)	Enrichment	% Elutriated
1	1,85	12,09	7,26	0,01	0,03	0,18	0,22	1,43	77%	2,5	79%
2	1,64	2,65	5,39	0,01	0,05	0,11	0,17	1,39	85%	5,0	46%
3	1,46	0,45	9,23	0,01	0,04	0,25	0,30	1,07	73%	9,8	82%
4	1,47	0,85	11,43	0,01	0,02	0,10	0,13	1,22	83%	4,7	61%
5	3,29	6,45	19,21	0,04	0,03	0,14	0,21	2,82	86%	4,6	87%
6	2,89	21,87	13,08	0,03	0,09	0,34	0,45	2,09	72%	3,9	98%
7	1,22	0,96	4,44	0,00	0,01	0,05	0,06	1,11	91%	4,9	88%

Table 42: Quantification of spiked tumor cell enrichment, recovery and purity within the last elutriation fraction by flow cytometry.

Trial	Tumor cells per 10^6 leukocytes		Tumor cell enrichment		Recovery (%)		Purity (%)
	Spiked	Recovered	Elutriation	Total (10^4)*	Total Elutriated	Spiked	
1	21	35	1,7	9,38	75	68	57
2	2,6	20	7,8	44,74	55	65 (13)	48 (1)
3	26	174	6,7	4,03	93	64 (5)	76 (32)
4	26	136	5,2	3,49	92	53 (15)	37 (8)
5	26	90	3,5	7,15	94	78 (9)	80 (2)
6	26	74	2,8	1,86	98	74	28
7	26	111	4,2	6,10	91	60	77

Table 43: Comparison of state-of-the-art enrichment techniques for circulating tumor cells.

Parameter	Density Gradient (80)	µ-Filtration (71)	Magnetic Bead (46, 76)	Microfluidics (43)	Elutriation & FACS
Enrichment Method	Oncoquick®	ISET (8 µm pores)	CellSearch™ (anti-EpCAM)	CTC-chip (anti-EpCAM)	Elutriation & FACS
Cytometric Detection	CK^+/hematoxylin$^+$	CK^+/7AAD$^+$	CK^+/$DAPI^+$/$CD45^-$	CK^+/$DAPI^+$/$CD45^-$	$CFSE^+$/$EpCAM^+$/$CD45^-$
Spike ratio (CTC/ml*)	7	3	3 - 150	50-50,000	26†
Capacity (ml*/test)	15	1 x 12 wells	7.5	1-2	TBV
Enrichment Factor	$4.5x10^2$	$5x10^3$‡	$4.0x10^4$	$7.1x10^4$‡	$6.6x10^4$
Recovery (%)	55	80	85	61	66
Purity (%)	0.04	0.2	1.4	50	58
Specificity (%)	99.882	99.980	99.998	100.000	100.000

*milliliters of blood

†Spike ratio = number of CTCs per 10^6 peripheral blood mononuclear cells (approximately 60 CTCs/mL blood).

‡1 mL of blood assumed to contain $7.1x10^6$ leukocytes (82)

Note: Expected values from flow cytometry detection are reported for Elutriation & FACS.

Note: Results were obtained from pre-clinical validation experiments where sensitivity is equivalent to recovery.

Abbreviations: anti-pan-cytokeratin antibody, CK; isolation by size of epithelial tumor cells, ISET; 7-aminoactinomycin D, 7AAD; 4,6-diamidino-2-phenylindole, DAPI; total blood volume, TBV (~ 5 L for the avg. adult)

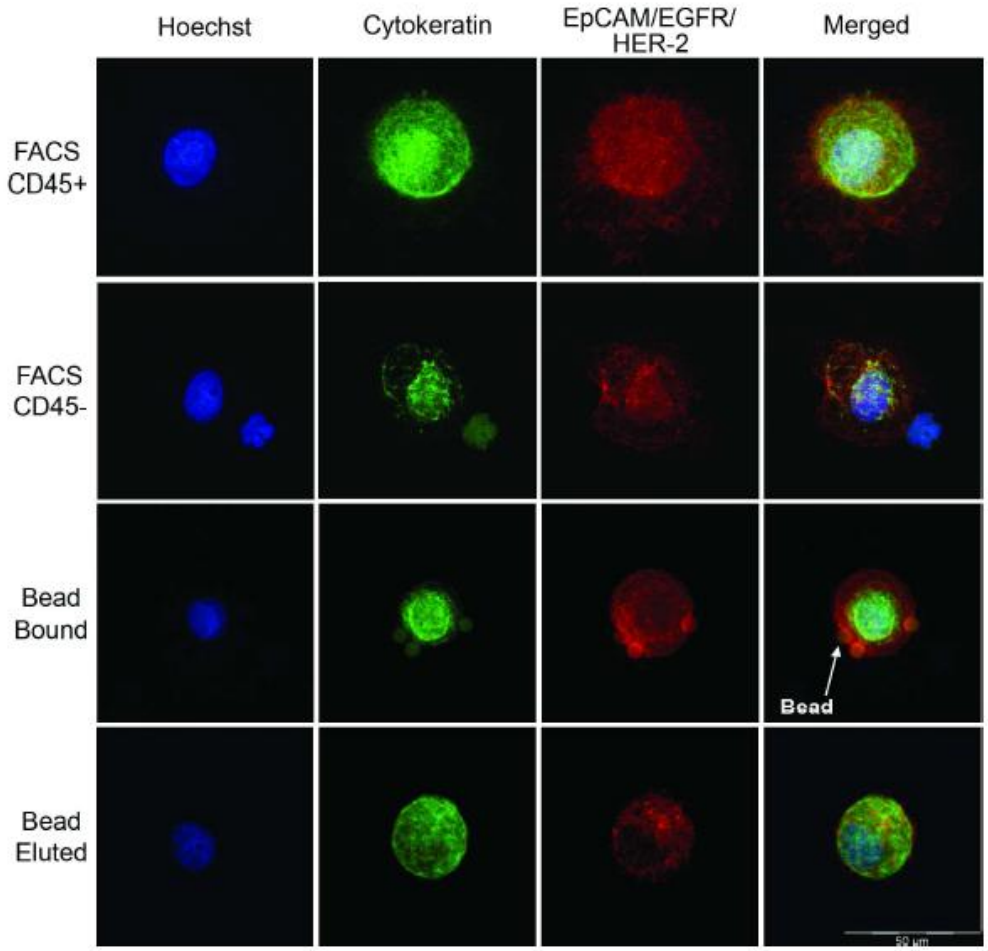

Figure 83: Fluorescent microscopy images representative of CaOV-3 tumor cells and leukocytes from the last elutriation fraction that were either isolated by FACS into CD45 negative or positive sorted groups, or captured and eluted by EpCAM coupled immunomagnetic beads. Cells were counted at 100 X magnification, and classified as tumor cells if they stained positive for Hoechst (nuclear), cytokeratin (cytoskeletal) and at least one of the epithelial cell antigens EpCAM, EGFR or HER-2 (membrane). Individual stains are represented in the first three columns, and are merged in the last column. Tumor cells were morphologically confirmed by their large size, rounded appearance and high nuclear to cytoplasmic ratio. Tumor cells were clearly distinguished from leukocytes using these criteria. The FACS CD45 positive images present a tumor cell to leukocyte aggregate with the leukocyte expressing cytokeratin at low levels compared to the tumor cell. Arrows depict bead captured cells prior to elution, and remaining bound DNA-linker after elution by DNAse I in the bead bound and bead eluted row of images, respectively. Images were acquired at 400 X magnification (scale 50 µm).

A proof of concept study was successfully performed for the isolation of circulating tumor cells from a large blood volume. Leukapheresis is the most common technique to collect cells from a large blood volume. It represents a minimally invasive procedure, requires an experienced clinic, and can only be used for patients in relatively good standing with no contradictions to the procedure. Following leukapheresis, CTCs were enriched and isolated using elutriation and FACS or immunomagnetic bead adsorption. The combination of elutriation and FACS outperformed current techniques with regard to the enrichment, recovery and purity of isolated tumor cells, and when combined with leukapheresis, the described process has at least a 500-fold greater capacity expected to increase tumor cell yield and incidence.

Tumor cells and leukocytes isolated by the 3-step process were found to be viable, and easily identified and distinguished using multiple cytometric and molecular techniques.

The main findings and conclusions

The combination of leukapheresis and elutriation led to a physical 10-fold enrichment of circulating tumor cells due to depletion of granulocytes during leukapheresis and lymphocytes during elutriation distributing about 240.000 tumor cells in 1.6 billion monocytes with a purity of 80%. The removal of lymphocytes thought to bind to EpCAM and granulocytes thought to contribute to false positive events during molecular analysis potentially improves the specificity of subsequent immunological enrichment techniques.

With the methodology developed within the OVCAD project, ccirculating tumor cells can be enriched with at least 200-fold whole blood capacity and equivalent recovery and purity compared to current technologies (Table 43). Using the criteria set forth by Cristofanilli *et al.*, who defines poor prognosis for metastatic cancer patients as the occurrence of 5 circulating tumor cells in 7.5ml of blood, the described system would have the potential to collect 2000 CTCs when 5L of blood is circulated with an expected tumor cell recovery of 60%. The increased number of isolated CTCs would be sufficient to improve the characterization of metastatic disease using molecular biology techniques and provide a metastatic *in vitro* disease model, and thus may enhance their diagnostic potential.

3. Summary

In the frame of OVCAD project, the ovarian cancer tumour bank has been established. It contains biological materials from blood, tumour tissues and ascites of about 300 ovarian cancer patients with advanced FIGO stage and treated with surgery and platinum-base chemotherapy. With these clinical materials, epigenomic, genomic, transcriptomic, and proteomic data from different biological materials have been generated. In addition, candidate markers at various molecular levels were validated. Models and signatures have been generated for the prediction of response of the patients to standard treatment, and to predict the outcome of the patients. Database have been established for the depository of all data generated from OVCAD, which will enable further collaboration of OVCA partners by data analysis and further networking in ovarian cancer research. Mechanisms involved in the drug resistance in ovarian cancer were investigated and an antibody-based therapy was evaluated. Circulating tumour cells were analyzed for their protein expression, genomic alterations and gene expression and were found to be a very heterogeneous cell population. In addition, a three-step technology combining leukapheresis, elutriation and fluorescence activated cell sorting technique was established for the enrichment and isolation of circulating tumor cells from a large blood volume.